

An atom-sorting machine

Dissertation

zur

Erlangung des Doktorgrades (Dr. rer. nat.)

der

Mathematisch-Naturwissenschaftlichen Fakultät

der

Rheinischen Friedrich-Wilhelms-Universität Bonn

vorgelegt von

Yevhen Miroshnychenko

aus

Kiew (Ukraine)

Bonn 2006

Angefertigt mit Genehmigung der Mathematisch-Naturwissenschaftlichen Fakultät

der Rheinischen Friedrich-Wilhelms-Universität Bonn

1. Referent: Prof. Dr. Dieter Meschede

2. Referent: Prof. Dr. Martin Weitz

Tag der Promotion: 16.08.2006

Diese Dissertation ist auf dem Hochschulschriftenserver der ULB Bonn
http://hss.ulb.uni-bonn.de/diss_online elektronisch publiziert

Памяти моих дедушек
Александра и Василия.

Abstract

In this thesis I present the realization of a technique for building strings of neutral atoms stored in a standing wave optical dipole trap with any desired interatomic separations atom by atom. As the first application of this technique I demonstrate the preparation of equidistant strings of atoms. Further, I demonstrate that this technique allows us to insert two atoms into a single potential well of a standing wave dipole trap and to deterministically induce light induced collisions between these atoms.

The first part of this thesis (Chapters 2 and 3) is devoted to the presentation of tools for trapping and detecting single atoms. A magneto-optical trap is our source of a desired small number of cold atoms. Strings of atoms are stored in a standing wave optical dipole trap. All spatial manipulations with the atoms are carried out with two dipole traps. An intensified CCD camera in combination with molasses cooling allows us to nondestructively observe and determine the positions of the atoms.

In the second part (Chapter 4) I describe the realization of the spatial manipulation of the atoms. I demonstrate the creation of strings of up to seven atoms by rearranging initially irregularly spaced atoms. The rearrangement is carried out by extracting atoms out of the initial string and by reinserting them back at predetermined positions using a second standing wave dipole trap operated as optical tweezers. Using this method, the distance between simultaneously trapped atoms can be actively controlled with a precision of $0.78(\pm 0.05) \mu\text{m}$ rms and a success rate of $98^{+2}_{-5} \%$. This precision corresponds to only 3-4 potential wells of the standing wave trap. Further, I experimentally demonstrate that our reinsertion technique is compatible with the insertion of an atom into the potential of the standing wave already occupied by another atom. We can induce inelastic interaction between these atoms by illuminating them with an optical molasses. The detected success rate of the insertion of one atom into the potential well occupied by the other atom is $16^{+4}_{-3} \%$, which is limited by the precision of insertion with our optical tweezers. Furthermore, I present analytical models of insertion and extraction processes which allows to identify the main mechanisms limiting the performance of our tweezers, e. g., precision and efficiency. Finally, I discuss the possibility to apply of our rearrangement technique to larger number of atoms.

Parts of this thesis have been published in the following papers:

1. Y. MIROSHNYCHENKO, W. ALT, I. DOTSENKO, L. FÖRSTER, M. KHUDAVERDYAN, D. MESCHÉDE, D. SCHRADER AND A. RAUSCHENBEUTEL, *An atom-sorting machine*, Nature, 442, 151 (2006)

2. Y. MIROSHNYCHENKO, W. ALT, I. DOTSENKO, L. FÖRSTER, M. KHUDAVERDYAN, D. MESCHEDE, D. SCHRADER, S. REICK AND A. RAUSCHENBEUTEL, *Inserting two atoms into a single optical micropotential*, quant-ph/0606113 (2006)
3. Y. MIROSHNYCHENKO, W. ALT, I. DOTSENKO, L. FÖRSTER, M. KHUDAVERDYAN, A. RAUSCHENBEUTEL AND D. MESCHEDE, *Precision preparation of strings of trapped neutral atoms*, physics/0607294 (2006)
4. Y. MIROSHNYCHENKO, D. SCHRADER, S. KUHR, W. ALT, I. DOTSENKO, M. KHUDAVERDYAN, A. RAUSCHENBEUTEL AND D. MESCHEDE, *Continued imaging of the transport of a single neutral atom*, Opt. Express **11**, 3498 (2003)

Contents

1	Introduction	1
2	Trapping of a single neutral atom	3
2.1	Magneto-optical trap	3
2.1.1	Operating principle	3
2.1.2	Experimental setup	5
2.2	Optical dipole trap	9
2.2.1	Dipole force on a two level atom	10
2.2.2	Dipole force on an Alkali-atom	12
2.2.3	Horizontal dipole trap	13
2.2.4	Vertical dipole trap	17
2.2.5	Imaging single trapped atoms	20
3	Number-locked loading of a dipole trap	27
3.1	Outline of the method	27
3.2	Experimental results	29
3.3	Analysis	30
3.3.1	Loss mechanisms	31
3.3.2	Quantitative study of atom losses	40
3.3.3	Conclusion	45
4	Spatial manipulation of individual atoms	47
4.1	3D transport of atoms	47
4.2	Precise calibration of the imaging scale	49
4.2.1	Using transportation	49
4.2.2	Using periodicity of the HDT	50
4.2.3	Conclusion	51
4.3	Extraction of an atom	51
4.3.1	Theoretical model of the width of the optical tweezers	52
4.3.2	Measurement of the width of the optical tweezers	55
4.3.3	Analysis	57
4.3.4	Effects not included into the theory	59
4.3.5	Towards ultimate resolution	59
4.4	Insertion of an atom	62
4.4.1	Insertion precision	63
4.4.2	Experimental studies of the insertion precision	66
4.4.3	Analysis	67
4.5	Insertion in the presence of other atoms	69
4.5.1	Insertion induced heating: Adiabatic model	69
4.5.2	Measurement of the heating effect	70

4.5.3	Analysis	71
4.5.4	Conclusion	71
4.6	Distance control between two atoms	72
4.6.1	Experimental realization	73
4.6.2	Experimental results	75
4.6.3	Analysis	79
4.6.4	Conclusion	80
4.7	Building an equidistant string of several atoms	80
4.7.1	Experimental realization	80
4.7.2	Experimental results	82
4.7.3	Analysis	82
4.7.4	Conclusion	83
4.8	Joining two atoms in one well of the standing wave	83
4.8.1	Experimental realization	83
4.8.2	Detection scheme	84
4.8.3	Experimental results	85
4.8.4	Analysis	86
4.8.5	Conclusion	87
5	Summary	89
6	Outlook	91
6.1	Quantum information processing	91
6.2	“Nano-chemistry”	92
6.3	Quantum simulations	92
A	Design and adjustment of the optical tweezers	95
A.1	Design goals	95
A.2	Design of the optical system	95
A.3	Adjustment of the optical tweezers	97
A.4	Experimental test of the performance of the VDT	98
B	Driving electronics of the EOM	99
C	Analysis of the ellipticity of the VDT	101
C.1	Tilted retro-reflecting mirror	101
C.2	Tilted lens	104
C.3	Analysis	107
D	Temperature of an atom from an ICCD image	109
	List of Figures	111
	List of Tables	112
	Bibliography	114

Chapter 1

Introduction

Technological advances such as laser cooling and trapping give us the possibility to experiments with ultracold atoms and even with new states of matter [1, 2, 3]. Atoms trapped in optical lattices have already led to the creation of Mott insulator state [4] and to possibility to experiment with single atoms [5, 6]. Moreover, a system of neutral atoms stored in optical lattices is a promising model system for new areas of research: In quantum information processing [7, 8], single atoms in different lattice sites can be used as qubits. In the area of quantum simulations [9, 10], optically trapped atoms can serve as a model system for a lattice of spin-1/2 particles interacting with each other allowing us, for example, to simulate hamiltonians from condensed matter physics. In chemistry, single atoms can be coherently bound into a molecule [11, 12, 13]. In all these experiments the creation of exactly controlled initial configuration and further control over external and internal degrees of freedom of the atoms is required.

There are two general approaches towards the creation of these experimental conditions: In the “top-down” approach one starts with a large sample of Bose-condensed atoms which are adiabatically loaded into a three-dimensional optical lattice. By inducing a quantum phase transition to the Mott insulator state [4, 14], a three-dimensional array with almost exactly one atom per lattice site is created. The control over the separations between the atoms in this approach is realized using the method of spin dependent transport [15]. Using this approach, the creation of large-scale entanglement using controlled collisions between the atoms in neighbouring lattice sites has already been demonstrated [16]. The production of dimer molecules using atoms in optical lattices has also been realized by starting with exactly two atoms per lattice site [17, 18, 19, 20, 21], where thousands of independent reactions in parallel were carried out. A draw-back of this approach is the small separation between atoms stored in adjacent sites which up to now makes the manipulation and detection at the level of an individual atom impossible.

In the “bottom-up” approach strings of optically trapped neutral atoms are built atom-by-atom while maintaining full control over the degrees of freedom of each individual atom. In our group single neutral atoms have been prepared and observed in optical dipole traps [5, 6]. When stored in a standing wave dipole trap, formed by a pair of counter-propagating laser beams, the absolute positions of the atoms can be optically measured

with sub-micrometer precision along the beam axis [22]. In addition, the atoms can be positioned along this axis using the dipole trap as an “optical conveyor belt” [6, 23]. In these experiments, the number of potential wells separating simultaneously trapped atoms can be exactly determined by optical means [22]. We have demonstrated that the state of an individual atom being part of an irregularly spaced string in the standing wave dipole trap can be selectively prepared and read out with high spatial resolution [24].

In this work I extend this list by the ultimate spatial manipulation of strings of atoms and present the first results concerning controlled interactions of two individual atoms. The method realized here allows us to control the positions of individual atoms of the string. The atoms are initially stored in random potential wells of a standing wave dipole trap as on an “object holder”. Individual atoms are then extracted using “optical tweezers” and inserted at predetermined positions on the object holder. I demonstrate the creation of small strings consisting of up to 7 atoms with equal separations. Furthermore, I have carried out an analysis of the processes of extraction and of insertion of the atoms with our optical tweezers. This analysis allows to identify the main effects limiting both the precision and the scalability.

Further, I present first results concerning the controlled interaction of two individual atoms inside the same micropotential of the standing wave of the dipole trap. In this experiment, one of the two atoms initially stored in different potential wells is extracted with the optical tweezers and placed into the potential well occupied by the second atom. By illuminating these two atoms with an additional laser beam we have deterministically induced inelastic interaction between the atoms.

Chapter 2

Trapping of a single neutral atom

Electromagnetic cooling and trapping of neutral atoms plays an essential role in our experiments, allowing us to isolate individual atoms in space and control their external degrees of freedom, i. e., number, position, temperature. We use two different types of traps: a magneto-optical trap and an optical dipole trap. Therefore, this chapter is divided into two parts covering our realization of the magneto-optical trapping (Sec. 2.1) and of the optical dipole trap for neutral cesium atoms (Sec. 2.2).

2.1 Magneto-optical trap

Cooling of atoms with near-resonant laser light has been first proposed three decades ago by T. Haensch and A. Shawlow [25]. After the first demonstration of the three dimensional cooling [26] and the subsequent modification with the inhomogeneous magnetic field, this idea evolved into a magneto optical trap (MOT) [27]. Since then, the MOT became a versatile tool for preparing samples of neutral atoms at submillikelvin temperatures and keeping them trapped for long times.

We use a specially designed MOT as a source of single cesium atoms for our experiments. The fluorescence signal from the MOT is imaged on a single photon detector, which allows us to count the exact number of atoms in real-time.

2.1.1 Operating principle

The working principle of the MOT relies on a velocity dependent cooling force to provide energy dissipation (Doppler cooling) and on a position dependent restoring force to provide spatial confinement of the atoms. The idea of the magneto optical trapping can be understood from a one-dimensional model, which can then be extended to a three-dimensional case.

Doppler cooling

Consider a two-level atom with a stable ground state and an excited state with a lifetime of $1/\Gamma$, where Γ is the natural linewidth. The levels are coupled by a radiative transition

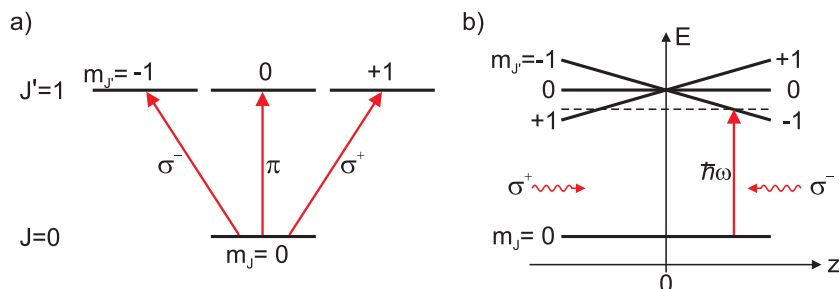


Figure 2.1: One-dimensional picture of the MOT. a) A model atom with $J = 0$ and $J' = 1$. The transitions with $\Delta m_J = -1, 0, 1$ can only be excited by σ^- , π and σ^+ -polarized light, respectively. b) A magnetic field gradient shifts the Zeeman sublevels such that the laser light from the beam from the right is preferentially absorbed, pushing the atom back to the center.

with resonance frequency ω_0 . The atom is illuminated by a laser beam with frequency ω and intensity I . The atom absorbs photons from the laser beam and spontaneously re-emits them. The corresponding scattering rate is given by

$$R_s(I, \Delta) = s_0 \frac{\Gamma}{2} \left[1 + s_0 + \left(\frac{2\Delta}{\Gamma} \right)^2 \right]^{-1}, \quad (2.1)$$

where $s_0 = I/I_0$ is the resonant saturation parameter, I_0 is the saturation intensity of the atomic transition, and $\Delta = \omega - \omega_0$ is the detuning of the laser from the atomic transition.

Suppose, the atom is moving in the field of the two counterpropagating laser beams, which are slightly red-detuned with respect to the atomic transition ($\Delta < 0$). Then, in the reference frame of the atom moving in the direction opposite to the propagation of one of the beams, the frequency of the laser light will be blue-shifted due to the Doppler shift, and the absolute value of the detuning Δ will be smaller for this beam. Therefore, according to Eq. 2.1, the absorption rate from the beam, opposite to the direction of the motion of the atom, will increase, and it will decrease for the other beam. Since the direction of the consequent re-emission of the photon is random, the average momentum transfer to the atom is in the direction opposite to its motion, thereby slowing down (or “cooling”) the motion of the atom. For small velocities the resulting force can be approximated by $F \sim v$, which resembles a motion of a particle in a viscous medium (“optical molasses”).

Position dependent force

Consider in addition to the previous model, that the angular momenta of the states of the model atom are $J = 0$ for the ground and $J = 1$ for the excited states. In the absence of a magnetic field the m_J -levels of the excited state are degenerate and are coupled to the ground state by different polarizations of the laser light, see Fig. 2.1a. The presence of a magnetic field shifts the excited states due to the linear Zeeman effect by

$$\Delta E = m_J g_J \mu_B B, \quad (2.2)$$

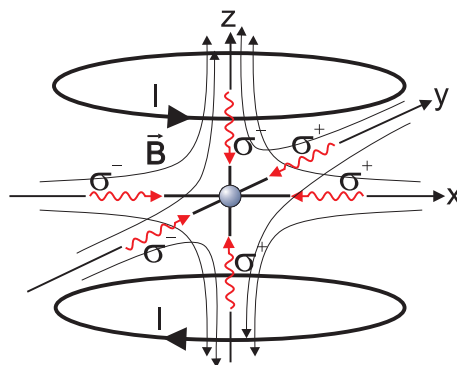


Figure 2.2: Three-dimensional schematic of the MOT. Two magnetic coils in anti-Helmholtz configuration produce the quadrupole field. Six circularly polarized laser beams exert cooling and trapping forces.

where g_J is the Landé g -factor and μ_B is the Bohr's magneton.

Suppose, the atom is placed in a linearly varying inhomogeneous magnetic field

$$B(z) = \frac{dB}{dz} z, \quad (2.3)$$

where dB/dz is the field gradient in the z -direction. Assume dB/dz is positive and $g_J > 0$. Then, for an atom on the right of the zero point of the magnetic field, the level $|J = 1, m_J = -1\rangle$ is shifted downwards, into resonance with the red-detuned cooling laser, see Fig. 2.1b. If the polarization of the laser beam from the right is σ^- , the absorption of the photons of this beam will increase. At the same time, if the polarization of the beam from the left is σ^+ , the corresponding photon absorption will be even reduced due to the increased detuning. This will result in a net force, pushing the atom to the left. Correspondingly, an atom on the left of the zero of the magnetic field gradient will be pushed to the right. This restoring force results in a one-dimensional localization of the atom. Together with the velocity dependent force this is a magneto optical trap, which can cool and trap neutral atoms.

The one-dimensional model of the MOT can be readily extended to the three-dimensional case. The six counter-propagating laser beams with the corresponding circular polarizations cross in one point. The necessary magnetic field gradient is produced by a magnetic quadrupole field with the zero of the magnetic field at the crossing point of the laser beams, see Fig. 2.2. This field can be produced by two coils in anti-Helmholtz configuration.

2.1.2 Experimental setup

The details of our MOT-system, i.e., the vacuum system, the cooling laser system and the magnetic coils, have been extensively described in previous theses of our group [28, 29]. Here, only a short overview of these components is presented.

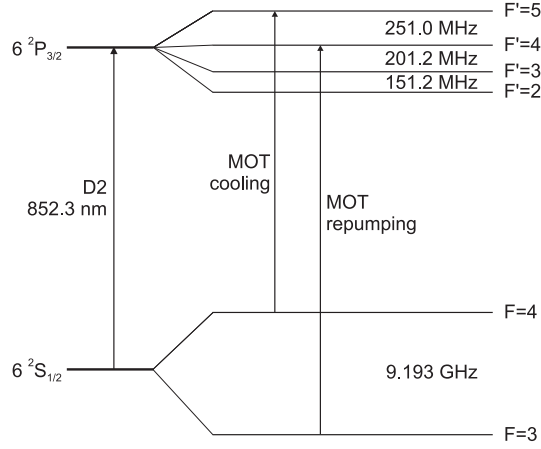


Figure 2.3: Simplified level scheme of the Cs atom. Shown are the transitions used for cooling and repumping in the MOT.

Vacuum setup

All our experiments are performed in a $30 \times 30 \times 125 \text{ mm}^3$ glass cell. It provides an optimal optical access from all the sides. The cell is attached to a vacuum chamber. A constantly working ion getter pump produces an ultra-high vacuum in the glass cell with a pressure of less than 10^{-10} mbar. A reservoir containing cesium is connected to the chamber by a valve, which is usually closed. Opening this valve about once a week for a few minutes sufficiently rises the cesium partial pressure for our experiments with single atoms.

Laser system

The closed transition from $F = 4$ to $F' = 5$ of the cesium D2 line ($\lambda = 852 \text{ nm}$) is used for cooling, see Fig. 2.3. Consequently, the frequency of the cooling laser is red detuned by approximately $\Gamma = 2\pi \cdot 5 \text{ MHz}$ from this transition. After an atom has absorbed a photon, it can spontaneously decay only to $F = 4$ and is ready to absorb the next cooling photon. There is, moreover, a small probability of off-resonantly exciting the atom to $F' = 4$ -level, from where it can decay to the $F = 3$ ground state. Due to the large hyperfine splitting the cooling laser does not excite this level. In order to return these atoms into the cooling cycle, a repumping laser excites the $F = 3$ to $F' = 4$ -transition. From the $F' = 4$ -state the atom can decay either back into the $F = 3$ -state and the repumping cycle repeats, or to the $F = 4$ -state, restoring the cooling cycle.

Geometrically, the MOT consists of three pairs of orthogonal laser beams, intersecting in one point inside the glass cell, see Fig. 2.4. The counter propagating beams are created by retro-reflection. The diameter ($2w_0$) of the MOT beams is about 2 mm with the typical power of $150 \mu\text{W}$ per beam, resulting in the saturation parameter of

$$s = s_0 \left[1 + \left(\frac{2\Delta}{\Gamma} \right)^2 \right]^{-1} = 0.5 \quad (2.4)$$

in each beam. The repumping laser is linearly polarized and is shined into the MOT area along the axis of the glass cell. We typically use 1 mW focused to about 0.5 mm. All the MOT lasers are diode lasers built in Littrow configuration, and their frequencies are actively stabilized using cesium polarization spectroscopy. Electronically controlled mechanical shutters are used to switch on and off each laser beam with a switching time of $< 100 \mu\text{s}$.

Magnetic coils

The quadrupole field of the MOT is created by two water-cooled coils in anti-Helmholtz configuration along the z -axis, see Fig. 2.4. They allow to run currents of about 16 A, thereby providing a high magnetic field gradient of 340 G/cm. The electronically controlled power supply of the coils allows us to switch between “high current” (16 A), “low current” (1.6 A) or “off”. The switching time is limited by eddy currents within the copper cooling plate, which take about 50 ms to decay.

With the high gradient of the magnetic field cesium atoms are randomly loaded into the MOT from the thermal background vapor at a loading rate of about 0.03 atoms/s. This slow dynamics of the atom number in the MOT is necessary for performing experiments at the level of few atoms. At the same time we need a possibility to quickly load atoms at the beginning of each experiment.

In order to speed up the loading process, we temporarily reduce the magnetic field gradient to $\partial B/\partial z = 34 \text{ G/cm}$ for the time of several tens of milliseconds. This increases the capture cross section of the MOT, thereby increasing the loading rate to about 50 atoms/s. Then, the field is switched to its initial value, confining the loaded atoms in the center of the MOT, and reducing the loading rate. Varying the loading time, one can select a specific average number of loaded atoms ranging from 1 to 50.

Atom counting

The atoms in the MOT can be counted by collecting their fluorescence light. Our atom counting method relies on the fact that each atom equally contributes to the intensity of the MOT fluorescence signal and on the high signal to noise ratio of our detection system, allowing us to distinguish discrete steps in the detected intensity for each capture or loss event in the MOT.

The fluorescence light from the MOT is first collected by a custom-designed diffraction limited objective [30]. Due to its high numerical aperture of 0.29, it collects light from about $\eta_{\text{obj}} = 2 \%$ of the solid angle. The light is then divided into two parts by the beam splitter. The reflected light is collected by an intensified CCD (ICCD, quantum efficiency of $\eta_{\text{ICCD}} = 10 \%$) camera, see Sec. 2.2.5. The transmitted light is focused onto an avalanche photodiode (APD, quantum efficiency of $\eta_{\text{APD}} = 50 \%$), see Fig. 2.4. In order to minimize the stray light background the entire optical path of the imaging system is wrapped in black paper and aluminum foil, the reflections of the MOT laser beams off the glass cell are carefully blocked, and the light is spectrally filtered using interference filters. Moreover, the light going to the APD is additionally spatially filtered using a pinhole [23, 29].

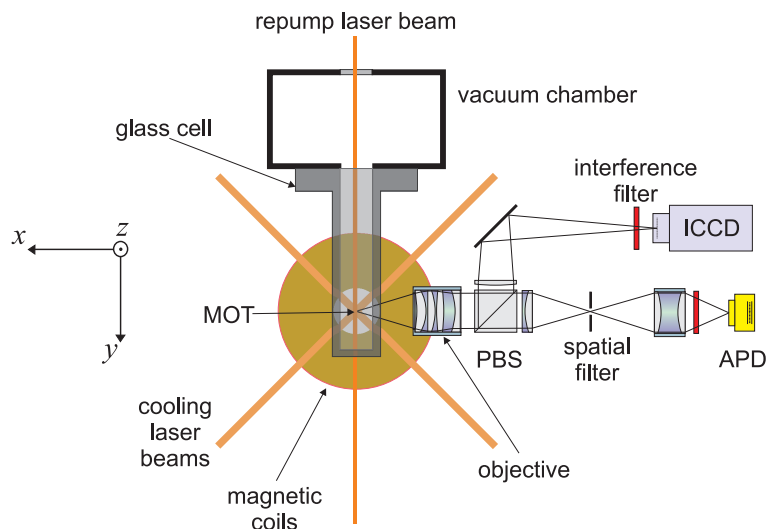


Figure 2.4: Experimental setup with the detection optics for the MOT fluorescence. The fluorescence light is collected and collimated by an objective. One part of the fluorescence signal is spatially and spectrally filtered and detected with an avalanche photo diode (APD). The other part is only spectrally filtered and sent into an intensified CCD camera.

The low background and the high signal to noise ratio of the detected fluorescence signal allows us to distinguish discrete levels in the detected intensity, see Fig. 2.5. For n trapped atoms we detect

$$N_n = (R_{\text{stray}} + n \cdot R_{1\text{atom}}) \cdot \tau_{\text{int}} \quad (2.5)$$

photons during the integration time τ_{int} . Here, R_{stray} is the count rate due to the stray light and the detector background, $R_{1\text{atom}}$ is the detected one-atom fluorescence rate, see Fig. 3.1a. For typical MOT parameters, we detect $R_{1\text{atom}} = 35000/\text{s}$ and $R_{\text{stray}} = 25000/\text{s}$. Synchronously, the CCD records about $R_{1\text{atom}}^{\text{CCD}} = 7000/\text{s}$.

The standard deviation of the photon number is fundamentally limited by Poisson statistics to $N_n^{-1/2}$. Fluctuations of the MOT laser beams including intensity, phase and pointing stability are taken into account in analogy with the description of intensity noise in laser beams by a global relative intensity noise $RIN = \delta N^2 / N^2$ where δN^2 represents the rms-value of these fluctuations. In our case $RIN = 0.01^2 - 0.02^2$.

In order to distinguish between n and $n + 1$ atoms, the total width of the peaks corresponding to neighboring atom numbers ($\Delta N = (N_n + RIN \cdot N_n^2)^{1/2}$) has to be compared to their separation $R_{1\text{Atom}} \tau_{\text{int}}$. In order to distinguish atom numbers with better than 95% confidence, the ratio

$$k_n = \frac{\Delta N}{N_{n+1} - N_n} = \left(\frac{R_{\text{stray}}}{R_{1\text{Atom}}} + n \right) \left(\frac{1}{n R_{1\text{Atom}} \tau_{\text{int}} + R_{\text{stray}} \tau_{\text{int}}} + RIN \right)^{1/2} \quad (2.6)$$

must be smaller than $1/4$. In our experiments, RIN begins to dominate this ratio for integration times $\tau_{\text{int}} \simeq 60$ ms. This time was chosen discriminating atom numbers from

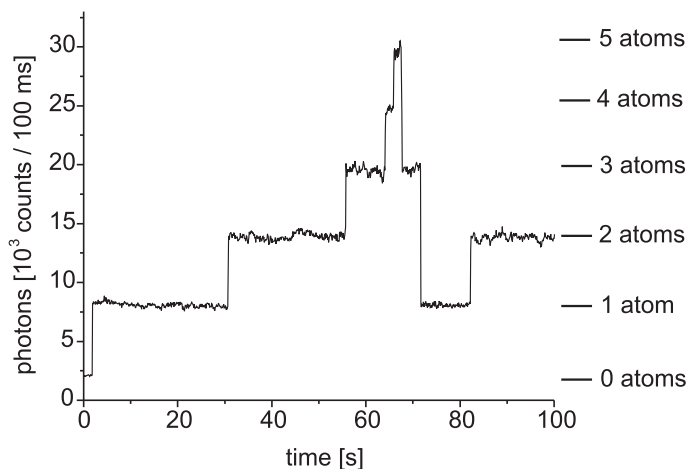


Figure 2.5: Count rate of the APD detecting the fluorescence from the MOT. Each trapped atom contributes the same amount of fluorescence to the signal. Each time an atom enters or leaves the trap the fluorescence signal increases or decreases step like, respectively. The exact number of trapped atoms can thus be unambiguously determined from the fluorescence signal. Note that this picture was taken in a system without the interference filter. Therefore, the one atom fluorescence rate is higher than the value given in the text.

the APD signal, since it is short compared to other experimental procedures, and longer times do not improve the signal to noise ratio. This method allows us to discriminate 1 to 20 atoms in the MOT with confidence level above 95 %.

2.2 Optical dipole trap

An alternative to the radiation pressure traps, such as the MOT, is an optical dipole trap. This trap offers certain advantages such as trapping of atoms in long living internal states in a conservative potential, reduced atomic scattering rate and long coherence times. The optical dipole trap relies on the electric dipole interaction with far-detuned light. The optical dipole force, acting as confining mechanism for neutral atoms in a dipole trap, was first considered by Letokhov in 1968 [31], who suggested that atoms might be one-dimensionally confined at the nodes or antinodes of a standing wave detuned far below or above the atomic resonance. Ashkin suggested three-dimensional traps for neutral atoms in 1978 [32]. The action of the dipole force on neutral atoms was demonstrated by Bjorkholm et al. in the same year [33]. The first demonstration of an optical trap for neutral atoms was done in 1986 by Chu et al. [34]. After this, dipole traps become a valuable, widely used tool for the manipulation of neutral atoms [35].

The action of the optical dipole forces is not restricted to neutral atoms, but affects any small polarizable particle. The first demonstration of the trapping of micron-sized particles was done in 1970 by Ashkin [36]. The further development of this technique [37] is widely used in biological, chemical and physics experiments as “optical tweezers” [38].

In our experiments we use two optical dipole traps. One of them is used as an “object holder” for neutral atoms loaded from the MOT. It is important to note, that also we call this trap “object holder”, the atoms are held free in space isolated from any contact with matter and not on the surface of a substrate. After the positions of all the atoms on the object holder have been determined, we use another dipole trap as “optical tweezers” to pick up a selected atom and to place it to some other position on the object holder. In this chapter I concentrate on the realization of the dipole trapping, whereas the spatial manipulation is covered in Ch. 4.

2.2.1 Dipole force on a two level atom

Classical model

The classical model gives an intuitive and transparent insight into the origin of the dipole force [35]. In this model the atom is a damped harmonic oscillator subject to the classical radiation field.

Consider an atom placed into laser light. The electric component of the field \mathbf{E} induces an atomic dipole moment \mathbf{p} that oscillates at the driving frequency ω :

$$\mathbf{p} = \alpha \mathbf{E}, \quad (2.7)$$

where $\mathbf{p}(\mathbf{r}, t) = \mathbf{e}p(\mathbf{r}) \exp(-i\omega t) + c.c.$, $\mathbf{E}(\mathbf{r}, t) = \mathbf{e}E(\mathbf{r}) \exp(-i\omega t) + c.c.$ and \mathbf{e} is the unit polarization vector. α is the complex atomic polarizability, which depends on the driving frequency ω .

The interaction potential of the induced dipole moment \mathbf{p} and the electric field \mathbf{E} is the dipole potential U_{dip} :

$$U_{\text{dip}} = -\frac{1}{2} \langle \mathbf{p} \cdot \mathbf{E} \rangle = |E|^2 \text{Re}(\alpha), \quad (2.8)$$

where $\langle \cdot \rangle$ denotes the time average over the rapid oscillating terms, and the factor $\frac{1}{2}$ takes into account that the dipole moment is induced and not a permanent one. Introducing $I = 2\varepsilon_0 c |E|^2$, one gets

$$U_{\text{dip}} = -\frac{1}{2\varepsilon_0 c} \text{Re}(\alpha) I. \quad (2.9)$$

This demonstrates that the potential energy of the atom in the field is proportional to the intensity I and to the real part of the polarizability. The latter describes the in-phase component of the dipole oscillation, showing the dispersive nature of the interaction. The dipole force itself is

$$\mathbf{F}_{\text{dip}}(\mathbf{r}) = -\nabla U_{\text{dip}}(\mathbf{r}) = \frac{1}{2\varepsilon_0 c} \text{Re}(\alpha) \nabla I(\mathbf{r}). \quad (2.10)$$

The considerations so far are valid for any polarizable neutral particle in any oscillating electric field.

The analytic form of the atomic polarizability $\alpha(\omega)$ is derived in Lorentz’s model of a classical harmonic damped oscillator. In this picture, an electron with the mass m_e and

elementary charge e is considered to be bound elastically to the core with an oscillation eigenfrequency ω_0 , corresponding to the optical transition frequency. The dipole radiation of the oscillating electron results in the damping $\Gamma = e^2\omega_0^2/(6\pi\epsilon_0 m_e c^3)$. The corresponding atomic polarizability is then

$$\alpha = 6\pi\epsilon_0 c^3 \frac{\Gamma/\omega_0^2}{\omega_0^2 - \omega^2 - i(\omega^3/\omega_0^2)\Gamma}. \quad (2.11)$$

Substitution of Eq. 2.11 into Eq. 2.9 yield the expression for the trap depth

$$U_{\text{dip}}(\mathbf{r}) = -\frac{3\pi c^2}{2\omega_0^3} \left(\frac{\Gamma}{\omega_0 - \omega} + \frac{\Gamma}{\omega_0 + \omega} \right) I(\mathbf{r}). \quad (2.12)$$

If the absolute value of the detuning $\Delta \equiv \omega - \omega_0$ is much smaller than the optical frequency ω_0 , which holds for our experiment, the rotating wave approximation can be applied to further simplify Eq. 2.12:

$$U_{\text{dip}}(\mathbf{r}) = -\frac{3\pi c^2}{2\omega_0^3} \frac{\Gamma}{\Delta} I(\mathbf{r}). \quad (2.13)$$

The last expression demonstrates the important point for dipole trapping that the sign of the dipole potential depends of the sign of the detuning. For $\Delta < 0$, which holds for our experiment, the dipole potential is negative and the interaction thus attracts atoms into the light field. Potential minima are therefore found at positions with maximum intensity.

Quantum model

In the quantum mechanical approach, the effect of far-detuned laser light on the atomic level can be treated as a perturbation in second order of the electric field, i. e. linear in terms of the light intensity. The corresponding Hamiltonian is $\hat{H} = -\hat{\mu} \cdot \mathbf{E}$, where $\hat{\mu} = -e\mathbf{r}$ is the electric dipole operator. The second order energy shift of the i -th atomic energy level in the non-degenerate case of the time independent perturbation theory is then given by

$$\Delta E_i = \sum_{j \neq i} \frac{|\langle j | \hat{H} | i \rangle|^2}{\mathcal{E}_i - \mathcal{E}_j}, \quad (2.14)$$

where \mathcal{E}_i is unperturbed energy. Further, a ‘‘dressed-state’’ view [39] for the relevant energies \mathcal{E}_i is applied considering the combined system of ‘‘atom plus field’’ [35]. In its ground state the atom has zero internal energy and the energy of the field is $n\hbar\omega$, where n is the number of photons. This results in the total energy $\mathcal{E}_i = n\hbar\omega$ for the unperturbed state. If a photon is absorbed by the atom, its energy becomes $\hbar\omega_0$, whereas the field energy is $(n-1)\hbar\omega$. This results then in the total energy $\mathcal{E}_j = \hbar\omega_0 + (n-1)\hbar\omega = -\hbar\Delta + n\hbar\omega$. Therefore, the denominator of Eq. 2.14 becomes $\mathcal{E}_i - \mathcal{E}_j = \hbar\Delta$.

For a two-level atom $\hat{H} = -\hat{\mu}E$, and the Eq. 2.14 simplifies to

$$\Delta E_g = \frac{|\langle e | \hat{\mu} | g \rangle|^2}{\Delta} |E|^2 = \frac{3\pi c^2}{2\omega_0^3} \frac{\Gamma}{\Delta} I \quad (2.15)$$

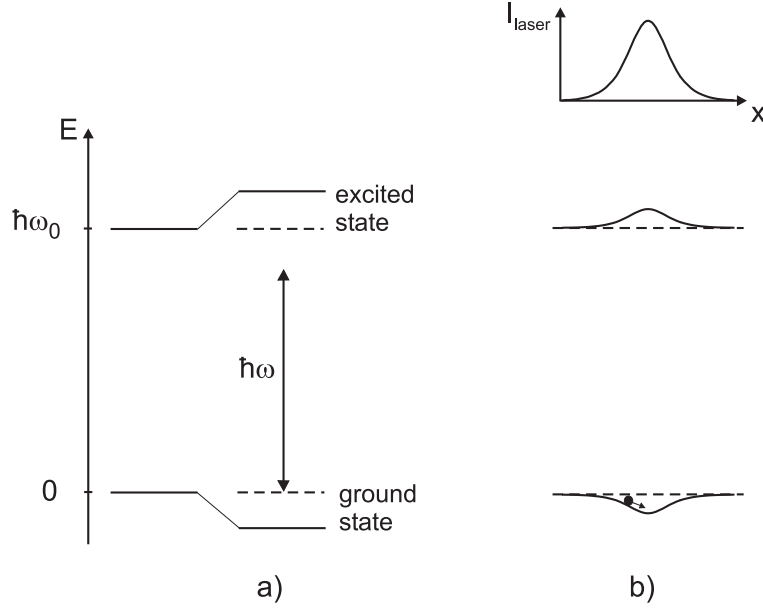


Figure 2.6: Light shifts for a two-level atom. a) Red-detuned light ($\Delta < 0$) shifts the ground state downwards and the excited state upwards by the same amount. b) A spatially inhomogeneous field like a Gaussian laser beam produces a ground state potential well, where an atom can be trapped.

for the ground state and

$$\Delta E_e = -\frac{3\pi c^2 \Gamma}{2\omega_0^3} \frac{I}{\Delta} \quad (2.16)$$

for the excited state, using the relations for the intensity of the field $I = 2\epsilon_0 c |E|^2$ and for the spontaneous decay rate $\Gamma = \frac{\omega_0^3}{3\pi\epsilon_0 \hbar c^3} |\langle e | \hat{\mu} | g \rangle|^2$. The result Eq. 2.15 shows that the optically induced shift, the “light shift”, of the ground state exactly corresponds to the dipole potential Eq. 2.13. The excited state shows the opposite shift, see Fig. 2.6a. In the interesting case of low saturation, the atom resides most of the time in its ground state. In a spatially modulated light field like a Gaussian beam, one can interpret the light shifted ground state as the trapping potential for the atom, see Fig. 2.6b.

The important difference between the classical and the quantum mechanical oscillator is the possible occurrence of saturation, which occurs at too high intensities of the driving field. But for the dipole trapping, only the unsaturated case is of relevance. As the consequence, Eq. 2.13 and Eq. 2.15 derived for these models agree.

2.2.2 Dipole force on an Alkali-atom

The existence of numerous possible resonant transitions in a Cs atom makes the calculations of the trapping potential less transparent. The classical model can approximately tackle this problem by applying Eq. 2.12 to each transition separately and adding up the

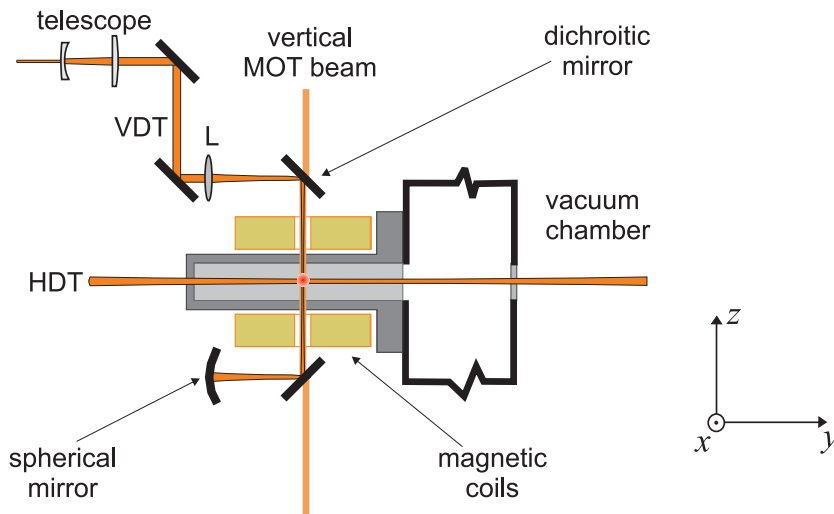


Figure 2.7: Beams of the HDT, VDT and the vertical beam of the MOT. Lens L focuses the incoming beam of the VDT at the position of the MOT. This beam is combined with the vertical beam of the MOT using a dichroic mirror. The spherical mirror retro-reflects the beam of the VDT to create a standing wave pattern. The beams of the HDT are focused at the position of the MOT and cross the VDT.

results weighted with each transition’s oscillator strength f_{osc} . The oscillator strength is used as a statistical weight of the strength of each transition.

For the trapping lasers in our experiment (1064 nm and 1030 nm), only D1- and D2-transition contribute significantly to the dipole force, whereas the relative contribution of the next strongest transition (to the $7P_{3/2}$) is only $3 \cdot 10^{-5}$ [29]. The corresponding oscillator strength for the cesium D1 ($\lambda_{\text{D1}} = 894$ nm, $\Gamma_{\text{D1}} = 2\pi \cdot 4.56$ MHz) and D2 ($\lambda_{\text{D2}} = 852$ nm, $\Gamma_{\text{D2}} = 2\pi \cdot 5.22$ MHz) lines are $f_{\text{osc,D1}} = 0.344$ and $f_{\text{osc,D2}} = 0.714$, respectively. One obtains from the contributions of the D1- and D2-transitions

$$U_{\text{dip}}(\mathbf{r}) = -\frac{3\pi c^2 A}{2} I(\mathbf{r}) \quad (2.17)$$

with

$$A = f_{\text{osc,D1}} \frac{\Gamma_{\text{D1}}}{\omega_{\text{D1}}^3} \left(\frac{1}{\omega_{\text{D1}} - \omega} + \frac{1}{\omega_{\text{D1}} + \omega} \right) + f_{\text{osc,D2}} \frac{\Gamma_{\text{D2}}}{\omega_{\text{D2}}^3} \left(\frac{1}{\omega_{\text{D2}} - \omega} + \frac{1}{\omega_{\text{D2}} + \omega} \right). \quad (2.18)$$

The quantum mechanical calculation of the light shifts including the multilevel structure of a cesium atom was done by D. Schrader [40].

2.2.3 Horizontal dipole trap

Historically, we had one standing wave optical dipole trap oriented horizontally (HDT), see Fig. 2.7. This trap we use as an “object holder”. The details about our horizontal dipole trap have been extensively described in the thesis of D. Schrader [40]. Here, I describe only the key properties, important for our experiments.

Trap parameters

The horizontal dipole trap consists of two counter propagating Gaussian laser beams with wavelength $\lambda_{\text{HDT}} = 1064$ nm, waist radius measured to be $w_{\text{HDT}} = 19$ μm by the oscillation frequency measurement, see Sec. 2.2.3. This waist and all other given beam sizes are to be understood as a $1/e^2$ -radius of the beam. The beams have the same waist position, linear polarization and optical power. The two beams are created by dividing a beam from a Nd:YAG laser, see Fig. 2.8a. Each beam goes first through an acousto-optic modulator (AOM) for the realization of an optical “conveyor belt”, see Sec. 4.1, and then the beams are overlapped to create a standing wave interference pattern with the waist at the position of the MOT, see Fig. 2.7. The corresponding trap profile, neglecting the Guoy phase as well as the curvature of the wavefronts of the Gaussian beams, is

$$U_{\text{HDT}}(x, y, z) = -U_{\text{HDT}}^0 e^{-\frac{2(x^2+z^2)}{w_{\text{HDT}}^2}} \cos^2(k_{\text{HDT}} \cdot y), \quad (2.19)$$

since the trap profile is proportional to the intensity distribution of the laser light, see Eq. 2.17. In the case of 100 % contrast of the standing wave, the depth of the HDT is

$$U_{\text{HDT}}^0 = 3\pi c^2 A \frac{P}{\pi w_{\text{HDT}}^2}, \quad (2.20)$$

where P is the laser power per beam.

For typical optical power $P = 1$ W per beam, the trap depth is $U_{\text{HDT}}^0/k_{\text{B}} = 0.8$ mK determined from the oscillation frequency measurement, see Sec. 2.2.3.

Single atom transfer efficiency

Our MOT allows us to prepare and reliably count single atoms. These atoms are then loaded into the HDT by simultaneously operating both traps during several tens of milliseconds. A high transfer efficiency of atoms between the MOT and the dipole trap is a prerequisite to our experiments.

The single atom transfer efficiency was measured by repeating the following sequence: One atom on average was prepared in the MOT. This atom was then loaded into the HDT and held for 100 ms. This was followed by the reloading of the atom back into the MOT for counting. The events with only one atom at the beginning were then post selected, in order to exclude any collision events between the atoms during this time, see Sec. 3.3.1. The ratio of the final number of atoms to the initial number of the loaded atoms yields the single atom transfer efficiency, which is in our case $98.7_{-1.1}^{+0.7}$ %. The error of this value comes from the binomial statistics.

Lifetime of atoms

The lifetime of atoms in the trap gives the estimate of the upper limit of the time scale for the experiments with the HDT.

In order to measure the lifetime, the following experimental sequence was executed: Initially, four atoms on average were loaded into the MOT and their initial number was

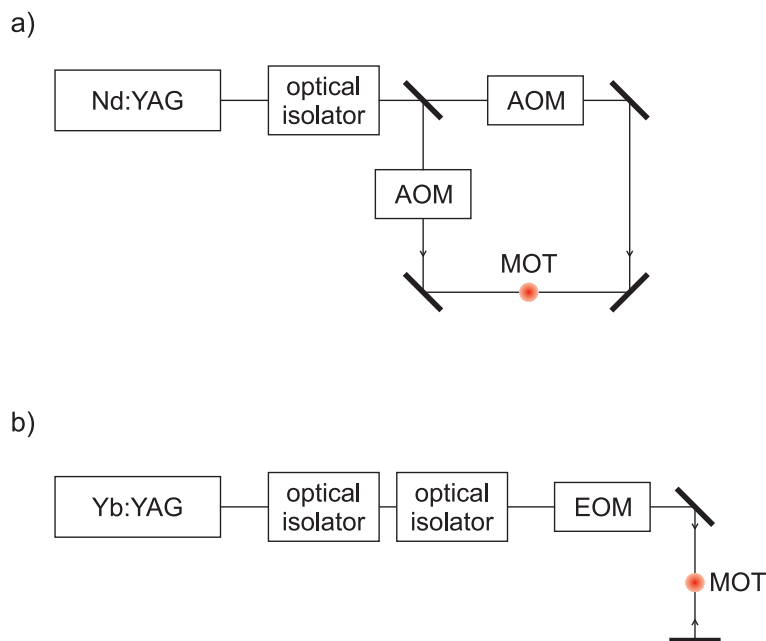


Figure 2.8: Block diagram of the laser systems of our dipole traps. a) The beam from a Nd:YAG laser is divided into two parts to create the horizontal standing wave dipole trap, overlapping with the MOT. b) The vertical standing wave dipole trap is created by retro reflecting the beam from an Yb:YAG laser. See text for details.

determined from the fluorescence signal. The atoms were then transferred into the HDT and the MOT was switched off. After certain time, the rest of the atoms was reloaded back into the MOT for counting. The survival probability of the atoms after storing them for a certain time was calculated as the ratio of the final number to the initial number of atoms. The result of this measurement for different storage times in the HDT is presented in Fig. 2.9.

An exponential function $p(t) = p_0 \exp(-t/\tau)$ with the free parameters τ and p_0 was fitted to the experimental points, see Fig. 2.9. The resulting $1/e$ -decay time is $\tau = 8(\pm 1)$ s, but $p_0 = 112(\pm 2)\%$, which is higher than expected 100%. This result indicates that the decay is not purely exponential, as it would be expected if the atom lifetime in the HDT was limited by background gas collisions only. Indeed, the experimental points suggest that the survival probability has a plateau shape for times shorter than one second, and only then begins to decay. This behavior can be understood assuming that the storage time in the trap is limited by heating effects [41]. The initial temperature of atoms in the trap is about $0.1 U_{\text{HDT}}^0$. Due to the heating effects in the HDT, the temperature of the atoms increases. After about one second the temperature reaches the value of the depth of the HDT and the atoms start to leave the trap.

In our case the heating effect is mainly caused by axial fluctuations of the standing wave pattern [42, 29]. These fluctuations come from the phase noise of the frequency synthesizer driving the AOMs of the HDT, see Sec. 4.1. In Sec. 2.2.5 we show that by

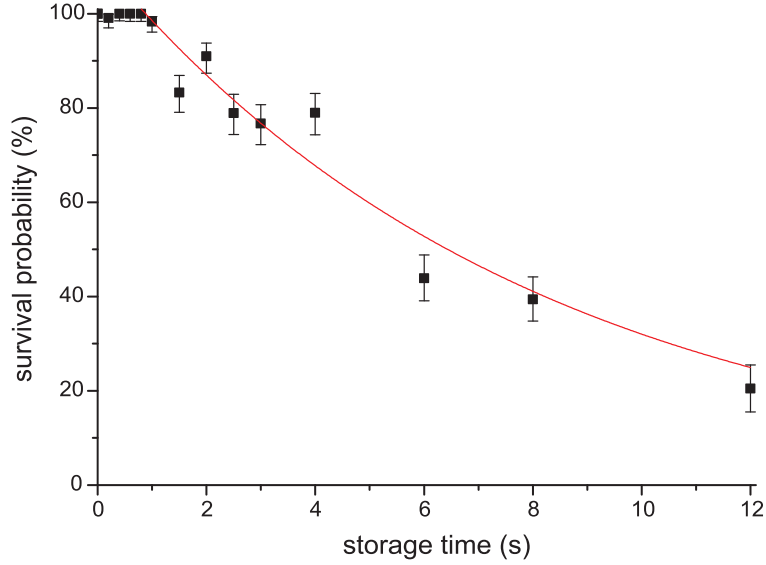


Figure 2.9: Measurement of the lifetime of the atoms in the HDT. The solid line is an exponential fit to the experimental data. Every point presents the result of about 30 repetitions of the sequence.

cooling atoms, we can reach the background limited lifetime of about 60 s.

Oscillation frequencies

In harmonic approximation, the axial and the radial oscillation frequencies of an atom in the center of the trap are connected with the depth of the trap U_{HDT}^0 and the waist of the Gaussian beam of the trap w_{HDT} by

$$\Omega_{\text{ax}} = 2\pi \sqrt{\frac{2U_{\text{HDT}}^0}{m_{\text{Cs}}\lambda_{\text{HDT}}^2}} \quad (2.21)$$

$$\Omega_{\text{rad}} = \sqrt{\frac{4U_{\text{HDT}}^0}{m_{\text{Cs}}w_{\text{HDT}}^2}}. \quad (2.22)$$

Therefore, by measuring these frequencies, one can independently calculate the waist of the Gaussian beam of the HDT and the depth of the trap for a certain optical laser power.

The method for measuring these frequencies is based on the fact that the atoms in a trap will be rapidly parametrically heated up and lost from the HDT, if the depth of the trap is modulated at exactly twice the oscillation frequency of the atoms in the trap [29]. For this, we load atoms into the trap, modulate the trap depth, and finally measure the survival probability of the atoms for this modulation frequency.

Since the trapping potential of the standing wave dipole trap has a Gaussian form in the radial directions and a sinusoidal form in the axial direction, the harmonic approximation holds only for cold atoms. As the atoms approach the top of the trap during the excitation,

the resonance frequencies of the trap are reduced. In order to take into account this unharmonicity, the whole frequency scan range was divided into the frequency intervals $\nu_1, \nu_2, \dots, \nu_N$, and in each interval the frequency was swept downwards from ν_k to ν_{k-1} , thereby following the unharmonicity of the trap as the atoms heated up. Moreover, we have detected even small excitations of the atoms in the trap by lowering the depth of the HDT to about 3 % of its initial value. In this case even small heating resulted in a measurable loss of the atoms.

The oscillation frequencies of our HDT are $\Omega_{\text{rad}}^{\text{HDT}}/2\pi = 3.6(\pm 0.2)$ kHz at 1.8 W and $\Omega_{\text{ax}}^{\text{HDT}}/2\pi = 265(\pm 8)$ kHz at 1.56 W, and were measured in [40]. This results in a depth of $U_{\text{HDT}}^0/k_B = 0.8(\pm 0.2)$ mK at 1 W of the optical power in each beam, and in a waist of $18.9(\pm 1.1)$ μm .

2.2.4 Vertical dipole trap

In order to pick up a selected atom and place it at some other position with high precision on the “object holder”, we use “optical tweezers”. As the optical tweezers for single atoms we use another standing wave optical dipole trap. This trap is oriented vertically (VDT), perpendicularly to the HDT, see Fig. 2.7. The details about the design and alignment of the trap are described in Appendix A. Below, I describe the key properties of the trap, important for our experiments.

Trap parameters

We use an Yb:YAG disk laser (model VersaDisk-1030-10-SF from Elektronik Laser System GmbH) with the maximum optical power of up to 25 W. The linearly polarized beam with a wavelength of $\lambda_{\text{VDT}} = 1030$ nm is focused on to the MOT, see Fig. 2.7. The waist of the beam is about $w_{\text{VDT}} = 9$ μm , see App. C. The standing wave is created by retro-reflecting the beam, see Fig. 2.8b. Since the beams of the VDT coincide with the vertical beams of the MOT, they are combined using a dichroic mirror, see Fig. 2.7.

The profile of the trap, neglecting the Guoy phase as well as the curvature of the wavefronts of the Gaussian beams, is described by

$$U_{\text{VDT}}(x, y, z) = -U_{\text{VDT}}^0 e^{-\frac{2(x^2+y^2)}{w_{\text{VDT}}^2}} \cos^2(k_{\text{VDT}} \cdot z). \quad (2.23)$$

For typical optical power of 0.6 W in the incoming beam we have a dipole trap depth of $U_{\text{VDT}}^0/k_B = 2.7$ mK, determined from the oscillation frequency measurement. Although this trap crosses the HDT, their interference patterns can be incoherently added due to the large detuning between the laser frequencies of these traps.

Single atom transfer efficiency

The single atom transfer efficiency was measured using the same method explained in Sec. 2.2.3 by loading single atoms from the MOT into the dipole trap and then reloading them back into the MOT. The measured efficiency is 100_{-5}^{+0} %.

Oscillation frequencies

The oscillation frequencies of the VDT have been measured using the method described in Sec. 2.2.3. The beam intensity modulation was realized with a high power electro-optic modulator (EOM) (from ALPHALAS GmbH) installed between two polarizers. The detailed description of the driving electronics of the EOM is given in Appendix B.

The axial frequency is $\Omega_{\text{ax}}/2\pi = 560(\pm 50)$ kHz, see Fig. 2.10a. The calculated corresponding depth of the VDT is $U_{\text{VDT}}^0/k_{\text{B}} = 2.7(\pm 0.5)$ mK for 560 mW of the laser power used in this experiment.

Figure 2.10b presents the results of the radial frequency measurement. We observe two peaks, which correspond to two oscillation frequencies $\Omega_{\text{rad1}}/2\pi = 12.8(\pm 0.7)$ kHz and $\Omega_{\text{rad2}}/2\pi = 18.0(\pm 1.2)$ kHz. The positions of the two peaks were reproduced two times for one adjustment of the experimental setup. This demonstrates that this effect was not a result of a drift of the VDT, but was rather characteristic for that adjustment. The presence of two oscillation frequencies means that the trap confinement on two radial directions is different, implying that the radial profile of the VDT is elliptic. This profile can be described by two waists $w_{\text{VDT1}} = 10.1(\pm 1.4)$ μm and $w_{\text{VDT2}} = 7.2(\pm 1.2)$ μm .

The ellipticity can be explained either by the fact that the reflected beam was slightly shifted with respect to the incoming beam of the VDT due to a slight tilt of the retro-reflecting mirror, or that the laser beam had a small astigmatic aberration, which can as well result in an ellipticity of the radial profile of the VDT at the position of the MOT. In the first case, the ellipticity depends on the adjustment for a given experiment. In the second case, the ellipticity is the same for all experiments. The numerical simulation and analysis of these two cases are presented in Appendix C. They show that both of these models can quantitatively explain the ellipticity of the trap during this measurement, and therefore explain the measured radial oscillation frequencies of the VDT. Consequently, at this point it is not possible to unambiguously conclude, which of these models is closer to the experimental situation. A separate measurement, characterizing the size of the optical tweezers by extracting atoms from the HDT described in Sec. 4.3, suggests that the astigmatic beam model is more appropriate.

Lifetime of atoms

The lifetime of atoms in the VDT was measured using the same method as for the HDT, see Sec. 2.2.3. The result of this measurement is presented in Fig. 2.11.

A fit of an exponential function $p(t) = p_0 \exp(-t/\tau)$ yields the $1/e$ -decay time of $\tau = 13(\pm 1)$ s. The second fit parameter is $p_0 = 111(\pm 4)\%$, which is higher than 100%. This suggests that the decay is not purely exponential, but rather limited by some heating effects, compare with the HDT in Sec. 2.2.3.

In our case the heating effects can be caused by pointing instability of the laser beam at the position of the atoms and by intensity fluctuations. The pointing instability can result in direct resonant excitation of the atoms, if the fluctuations of the two beams of the standing wave are correlated. If the fluctuations are not correlated, the pointing instability will result in a change of the contrast of the standing wave pattern, which results in the modulation of the trap depth, and therefore in parametric heating of the

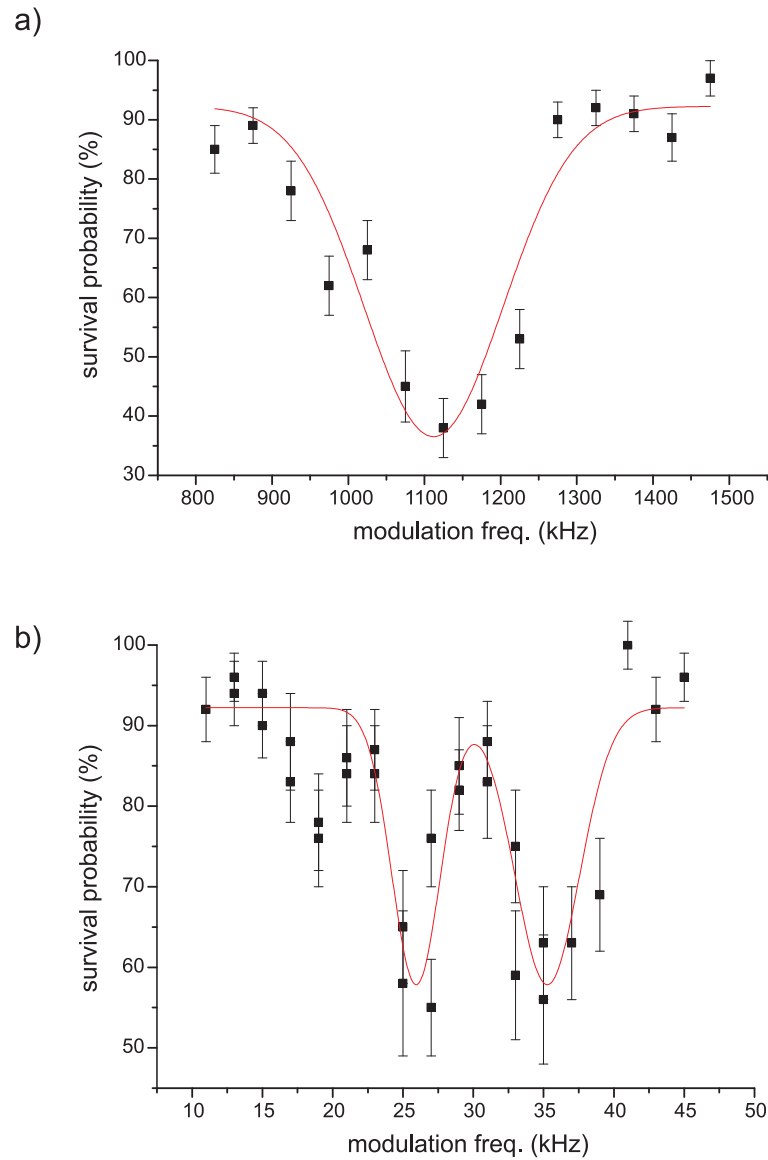


Figure 2.10: a) Axial oscillation frequency of the VDT. The points present the measured survival probability after parametric heating followed by the adiabatic lowering of the trap depth. The curve is a fitted Gaussian. b) Radial oscillation frequencies. The measured data (points) are fitted with a sum of two Gaussians. Every data point is the result of about 20 repetitions with on average 5 atoms per repetition.

atoms. The intensity fluctuations can result in the modulation of the trap depth, and therefore in parametric heating of the atoms in the trap as well.

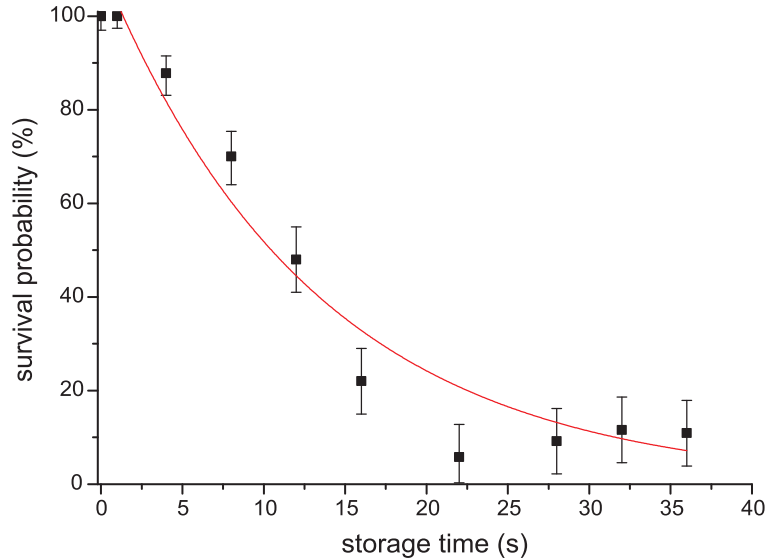


Figure 2.11: Measurement of the lifetime of the atoms in the VDT. The solid line is an exponential fit to the experimental data. Every point is the result of about 15 repetitions of the sequence.

2.2.5 Imaging single trapped atoms

The possibility to count atoms in the MOT allows us to load a well known number of atoms into the HDT. After this transfer the atoms occupy random potential wells forming a string of atoms with random separations. In order to manipulate individual atoms, we need to know the initial positions of the atoms in the HDT. For this purpose, we image the atoms using the ICCD camera, see Fig. 2.4.

However, direct imaging of the atoms in the HDT is not possible, for the scattering rate of the atoms in the HDT is low [40], and the interference filter before the ICCD camera additionally suppresses the photons scattered from the trap, see Fig. 2.4. This problem can be overcome by illuminating the trapped atoms with resonant or near-resonant light. During the illumination, each scattered photon adds energy $E_r = \hbar^2 k^2 / (2m_{\text{Cs}})$ on absorption and E_r on emission. Therefore, the atoms will be heated during the illumination. An atom initially at the bottom of the trap with a depth of $U = 1$ mK will scatter about $U / (2E_r) = 5600$ photons before the atom is lost from the dipole trap. Taking into account the efficiency of our imaging optics, we would only detect about 10 photons on the ICCD camera before the atom leaves the trap. Although this is in principle already enough to detect the atom, this method is obviously destructive.

Molasses cooling

A solution to this problem is to illuminate the trapped atom with three-dimensional optical molasses. We use the MOT beams for this purpose, however, we reduce the power of each beam to about $80 \mu\text{W}$ and red-detune them by about 1.5Γ , relative to the transition of the

free atom. Additionally, the levels of the atoms in the HDT are light shifted by about 6Γ . This results in the saturation parameter of $s = 0.01$ for each beam. The molasses cools the atom in the dipole trap, while up to $R_s = 170000$ photons/s are scattered. From this scattering rate we can estimate how many photons we expect to detect in our experiment:

$$R_{\text{det}} = \eta_{\text{obj}} \cdot \eta_{\text{BS}} \cdot \eta_{\text{F}} \cdot \eta_{\text{ICCD}} \cdot R_s = 120 \text{ photons/s},$$

where $\eta_{\text{obj}} = 0.02$ is the collection efficiency of the objective, $\eta_{\text{BS}} = 0.5$ is the loss on the beam splitter, $\eta_{\text{F}} = 0.7$ is the loss on the interference filter, and $\eta_{\text{ICCD}} = 0.1$ is the quantum efficiency of the APD, see Fig. 2.4. In the experiment we typically detect about 150 photons/s per atom in the HDT on the ICCD chip, which is in a good agreement with the estimation above.

The illumination of the atoms in the HDT with the optical molasses not only allows us to detect enough photons for atom imaging, it also continuously cools the atoms. Under this continuous cooling, the lifetime of the atoms in both dipole traps is increased. The results of the measurements of the increased lifetime of atoms in both traps is presented in Fig. 2.12. Here, we have used the method described in Sec. 2.2.3, with the modification that the atoms were additionally illuminated by the optical molasses. The lifetime was determined from the fit of $p(t) = p_0 \exp(-t/\tau)$. In this case, the $1/e$ -time in the HDT is $\tau_{\text{HDT}} = 57(\pm 11)$ s and $\tau_{\text{VDT}} = 62(\pm 7)$ s in the VDT, which are about one order of magnitude larger than the corresponding lifetimes without the molasses cooling. The fact that both time constants are equal within the error bars, and the exponential function fits the data reasonably well, suggests that this lifetime is limited by the background gas collisions.

Continued imaging

We image atoms in the HDT by collecting the fluorescence photons during the illumination with the optical molasses. Each detected photon produces about 350 counts on the CCD chip. The counts are concentrated in a 3×3 pixel area with about 50 % in the central pixel. Since our imaging optics has a magnification of $26.1(\pm 0.1)$, one CCD pixel of $13 \times 13 \mu\text{m}^2$ corresponds to $0.499(\pm 0.002) \mu\text{m}$ at the position of the atom (for more details about the calibration methods see Sec. 4.2). Figure 2.14a shows an image of a single atom trapped in the HDT with 1 s illumination time. The observed spot corresponds to about 160 detected photons. We determine the size $(\sigma_{\text{HDT}}^h, \sigma_{\text{HDT}}^v)$ and the position of the fluorescence spot by binning the pixels of the picture in the horizontal and vertical directions after suitably clipping the image to minimize the background noise, and by fitting the resulting histograms with Gaussians as shown in Fig. 2.13.

The $1/\sqrt{e}$ -half width of the fluorescence spot in the vertical direction is $\sigma_{\text{HDT}}^v = 3.31(\pm 0.08) \mu\text{m}$, which is smaller than the $1/\sqrt{e}$ -half width of the laser beam of the HDT of $b = 9.5 \mu\text{m}$. This shows that the atom is trapped close to the minimum of the HDT potential and remains cold during the illumination. The temperature of the atom can be estimated using a Fokker-Planck equation model, see App. D,

$$T = \frac{U_{\text{HDT}}^0}{k_{\text{B}}} \left(\frac{a}{b} \right)^2, \quad (2.24)$$

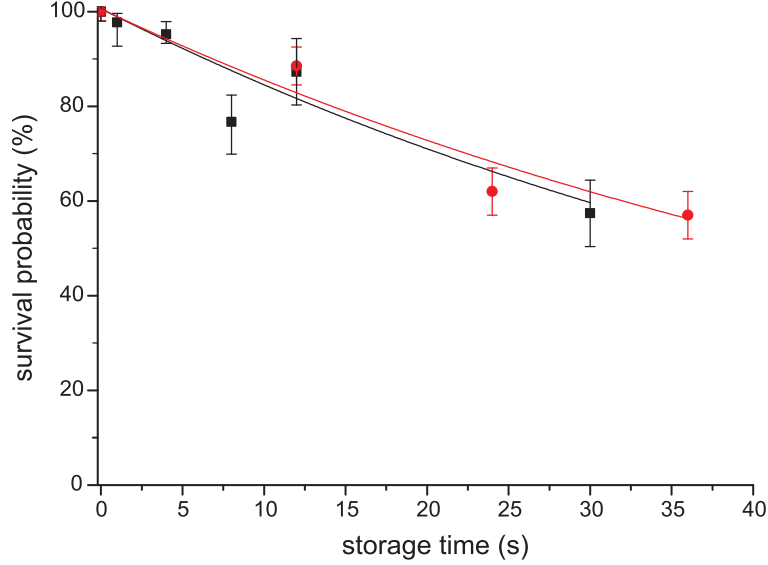


Figure 2.12: Measurement of the lifetime of the atoms in our dipole traps in presence of the optical molasses cooling. The squares present the measurement with the HDT. The solid line is an exponential fit to the experimental data. The circles present the measurement with the VDT with the corresponding exponential fit.

where $a = \sqrt{(\sigma_{\text{HDT}}^v)^2 - (\sigma_{\text{HDT}}^h)^2}$. Together with the horizontal width of $\sigma_{\text{HDT}}^h = 1.3(\pm 0.1) \mu\text{m}$ and $U_{\text{HDT}}^0/k_{\text{B}} = 0.8 \text{ mK}$, we obtain a temperature of $T = 80(\pm 20) \mu\text{K}$, which agrees well with the temperatures determined by other methods, see Sec. 4.3 and [29].

From the standing wave geometry we know that the axial confinement of the atoms is $\ll \lambda_{\text{HDT}}/2 = 0.532 \mu\text{m}$. However, the observed width of the fluorescence spot in the horizontal direction is $\sigma_{\text{HDT}}^h = 1.3(\pm 0.1) \mu\text{m}$. The deviation of the σ_{HDT}^h from the expected diffraction limited spot size of $\sigma_{\text{diff}} = 0.6 \mu\text{m}$ [23] is mainly due to the fact that one photon detected by the camera produces a spot on the CCD chip with an average $1/\sqrt{e}$ -half width of $\sigma_{\text{ICCD}} = 1.1(\pm 0.2)$ pixels, which corresponds to $0.6(\pm 0.1) \mu\text{m}$ [40]. The rms sum of σ_{ICCD} together with the σ_{diff} yields $\sigma_{\text{total}} = 0.9(\pm 0.1) \mu\text{m}$, which is less than the measured value of $\sigma_{\text{HDT}}^h = 1.3(\pm 0.1) \mu\text{m}$. The difference can come from aberrations in the imaging system. The most probable source of this aberration is a slight tilt of the imaging objective [43], which can result in astigmatism and coma.

Figure 2.14b shows an image one atom trapped in the standing wave of the VDT. This is the same atom that was in the HDT shown in Fig. 2.14a. The atom was first reloaded back into the MOT and then loaded into the VDT. The observed spot corresponds to about 440 photons. The vertical size $\sigma_{\text{VDT}}^v = 1.18(\pm 0.02) \mu\text{m}$ equals within the error bars the size σ_{HDT}^h , for the VDT is perpendicular to the HDT, and the atom is tightly confined along the vertical direction. The horizontal size is $\sigma_{\text{VDT}}^h = 1.5(\pm 0.1) \mu\text{m}$, which is smaller than the $1/\sqrt{e}$ -half width of the laser beam of the VDT of about $5 \mu\text{m}$, showing that the atom remains trapped in the bottom of the trap during the illumination.

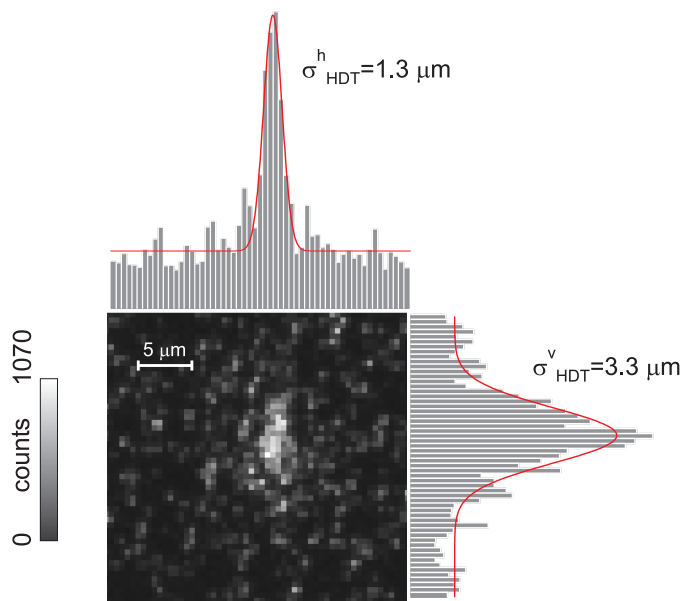


Figure 2.13: CCD image of one atom in the HDT (exposure time 1 s). The counts are binned in the vertical and horizontal directions and fitted with Gaussians to determine the size and the absolute position of the fluorescence spot in the horizontal and vertical directions.

If both traps are operated simultaneously, see Fig.2.14c, the atom is tightly confined in the horizontal and in the vertical directions simultaneously. For this image, the HDT was switched on in addition to the VDT, and the same atom is now confined in both traps. The fluorescence spot corresponds to about 100 detected photons. Due to the tight axial confinement of both traps, the sizes of the fluorescence spot should be equal and compatible with $\sigma_{\text{total}} = 0.9(\pm 0.1) \mu\text{m}$ in the absence of aberrations. The sizes are $\sigma_{\text{HDT+VDT}}^h = 1.06(\pm 0.08) \mu\text{m}$ and $\sigma_{\text{HDT+VDT}}^v = 1.16(\pm 0.06) \mu\text{m}$. They are equal within the error bars but are larger than σ_{total} , which can be attributed to the presence of aberrations on our imaging system. The fact that $\sigma_{\text{HDT}}^h = 1.3(\pm 0.1) \mu\text{m}$ is larger than $\sigma_{\text{HDT+VDT}}^h$ is the result that the atom in the HDT is confined in a region larger than the depth of focus of the objective ($6.4 \mu\text{m}$) [29], which results in a blurred image.

The difference in the number of the detected photons in all three cases can be attributed to the different light shifts of the atomic levels produced by the two dipole trap lasers.

Position of an atom

We have measured a horizontal width of the fluorescence spot in the HDT of $\sigma_{\text{HDT}}^h = 1.3(\pm 0.1) \mu\text{m}$, whereas the lateral localization of the atom in the standing wave of the HDT is 35-50 nm rms, depending on the trap depth and on the atomic temperature [22]. This difference indicates that the image of the atom is blurred, which limits the resolution.

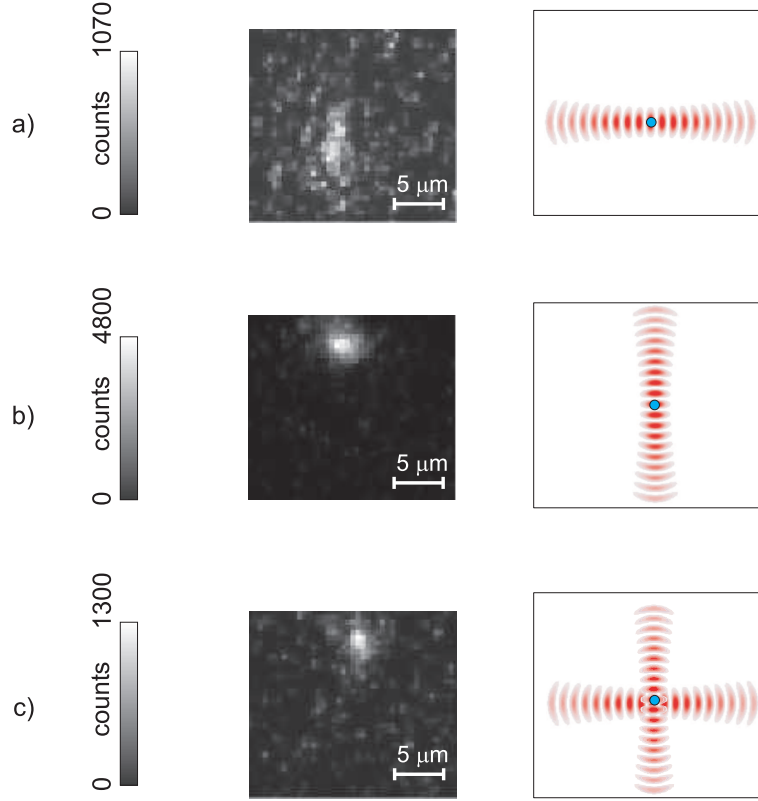


Figure 2.14: Images of the same atom trapped in our dipole traps (exposure time 1 s). a) The atom is trapped in a potential well of the HDT under continuous illumination with 3-D optical molasses. On the right side, the respective configuration of the traps is shown. b) The same atom reloaded first back into the MOT and than into the VDT. c) The same atom trapped simultaneously in two traps.

In order to understand the source of the blurring and be able to extract as much as possible information from the image, we discuss the steps of the image formation.

The influence of the imaging system on the image can be modeled by the point spread function (PSF) of the imaging system. The PSF determines how a single point $i(x, y)$ in the object plane is being imaged onto the image plane $I(h, v)$. Representing the object as a collection of points (x, y) , the image can be constructed by replacing the geometric image of each point $(h(x), v(y))$ with the PSF weighted by the intensity of this point. This operation is a convolution:

$$I(h, v) = \int_{-\infty}^{\infty} \int_{-\infty}^{\infty} i(x(h) - \chi, y(v) - \gamma) PSF(h(\chi), v(\gamma)) d\chi d\gamma + N(h, v), \quad (2.25)$$

where $N(h, v)$ is additive noise, originating from shot noise, stray light, electronic noise and dark counts of the detector. This noise additionally distorts the image. The problem of restoring the intensity distribution i in the object plane from the detected intensity distribution in the image plane I occurs in astronomy in numerous cases of mapping of

emission spectra and reconstruction of telescope images [44], as well as in chemistry and biology in fluorescence microscopy [45].

There are two classes of image processing techniques, which have been developed to tackle this problem: image restoration and parameter estimation. The aim of *image restoration* is to determine the intensity in the object plane, whereas *parameter estimation* fits a model of the object and the image formation to the data by optimizing a small set of model parameters [45]. In our experiments we use the parameter estimation method, since we are only interested in the lateral position of the atom.

We bin the pixels of the ICCD image in the vertical direction, obtaining a one-dimensional intensity distribution $I(h)$. This distribution is a convolution of the corresponding line spread function (LSF) and of a one-dimensional intensity distribution in the object plane. After integration of Eq. 2.25 in the vertical direction we have:

$$I(h) = \int_{-\infty}^{\infty} i(x(h) - \chi) LSF(h(\chi)) d\chi + N(h). \quad (2.26)$$

For all experiments in this thesis we approximate the LSF of our imaging optics by a Gaussian. Since the lateral localization of each atom in the HDT is much smaller than the width of the LSF ($\sigma_{\text{HDT}}^h = 1.3 \mu\text{m}$), we approximate $i(x)$ as a sum of delta functions corresponding to the positions of the atoms. This results in a sum of shifted Gaussians with the same parameters. By fitting a sum of Gaussians to the detected fluorescence $I(h)$, the deconvolution operation is effectively applied, neglecting noise. We define the position of the atom as the position of the maximum of the fitted LSF. Using this image processing method we are thus able to determine the position of each atom in the HDT along the trap axis with a precision of 140 nm [22], which is an order of magnitude smaller than the size of the fluorescence peak of $\sigma_{\text{HDT}}^h = 1.3 \mu\text{m}$ and even smaller than the wavelength of the fluorescence light of 852 nm and the size of a DT micropotential (532 nm). This precision is mainly limited by the statistical error, resulting from the shot noise of the detected photons, the background noise of our ICCD image and the position fluctuations of the HDT [22].

Conclusion

Continued illumination with the optical molasses of an atom in both of the dipole traps counteracts heating processes and allows us to nondestructively image atoms in the dipole traps. Additional processing of the images of the atoms allows us to determine the atomic positions in the HDT with submicrometer precision.

Chapter 3

Number-locked loading of a dipole trap

We experiment with few trapped atoms. In order to get enough data to make statistically significant statements about the result of an experiment, such as ones described in Sec. 4.6-4.8, the experiment should be repeated many times under the same initial conditions, e. g., starting with the same number of atoms. Although using our forced loading of the MOT, see Sec. 2.1, we can adjust the average number of loaded atoms, the exact number fluctuates according to Poissonian statistics. The atoms prepared in the MOT are transferred into the HDT, where all our experiments take place, and only the experimental shots with the desired number of atoms are post selected for the data analysis. Therefore, fluctuations of the atom number reduce the efficiency of the experiment. For example, the maximum probability to load exactly two atoms is about 0.3 and drops even further with increasing number of atoms. Performing experiments in the shortest time is important to reduce the effect of drifts and misalignment of the experimental setup. In order to speed up our experiments, we have implemented a method of loading a desired number of atoms into the dipole trap with high probability, which we call “number-locked loading” method.

3.1 Outline of the method

The basic idea is to use our computer control in order to transfer atoms from the MOT into the HDT and start the main experiment if and only if the current number of atoms in the MOT equals the desired number. Otherwise, it ejects the atoms from the MOT and loads the MOT again from the background gas by lowering the magnetic field gradient, see Sec.2.1.

The computer control consists of two programs, which we call “Experiment Control” [28] and “Experiment Manager”. Experiment Control allows us to program several experimental sequences, e. g., ejection of atoms from the MOT and loading the MOT from the background gas, transfer of atoms between the MOT and the HDT, etc. Experiment Manager counts the current number of atoms in the MOT, by collecting MOT fluorescence light and using a suitable calibration of the fluorescence count rate. Depending on the

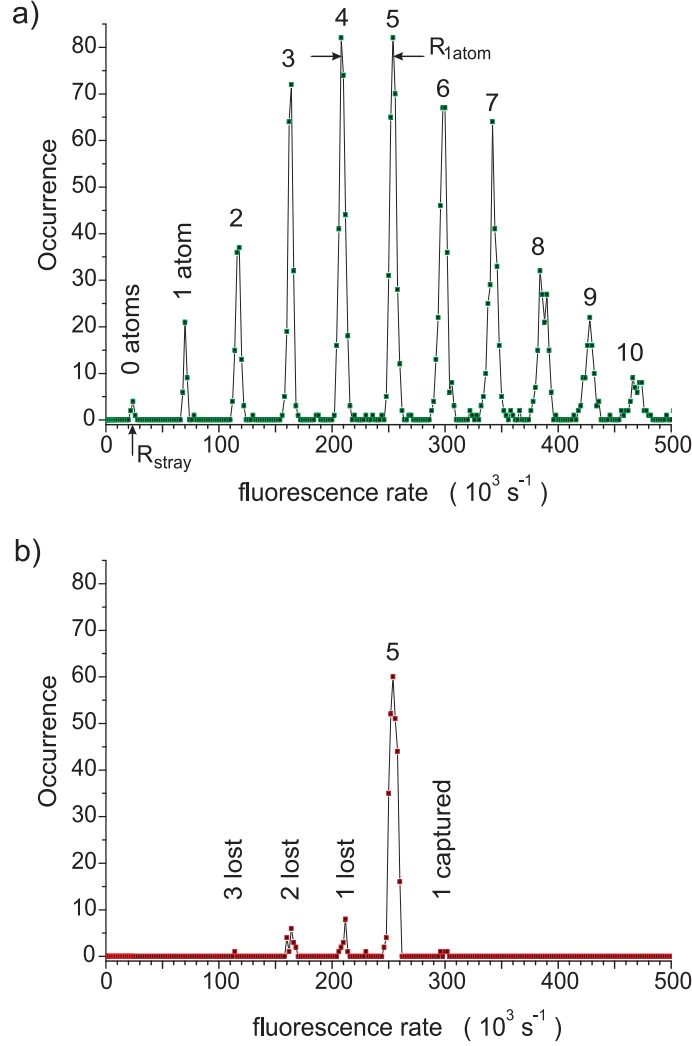


Figure 3.1: Histograms of the fluorescence rate in the MOT (integration time 60 ms). Each peak corresponds to a definite number of atoms. a) Fluorescence at the input of the discriminator after loading the MOT with five atoms on average. Each time the discriminator detected the presence of five atoms, they were transferred into the HDT and reloaded back into the MOT, where finally the fluorescence histogram (b) was recorded. This histogram corresponds to 300 times of detection of five atoms by the discriminator.

current number of atoms, this program sends a command the Experiment Control program to start a desired sequence, thus actively managing the experiment. In particular, using these programs we are able to prepare a desired number of atoms in the MOT, transfer them into the HDT and start the main experiment, thereby realizing the number-locking loading of the HDT. Since the two programs run on different computers, they communicate with each other via the TCP-protocol and have a communication delay of $125(\pm 25)$ ms, which will be important during the analysis of the experimental results.

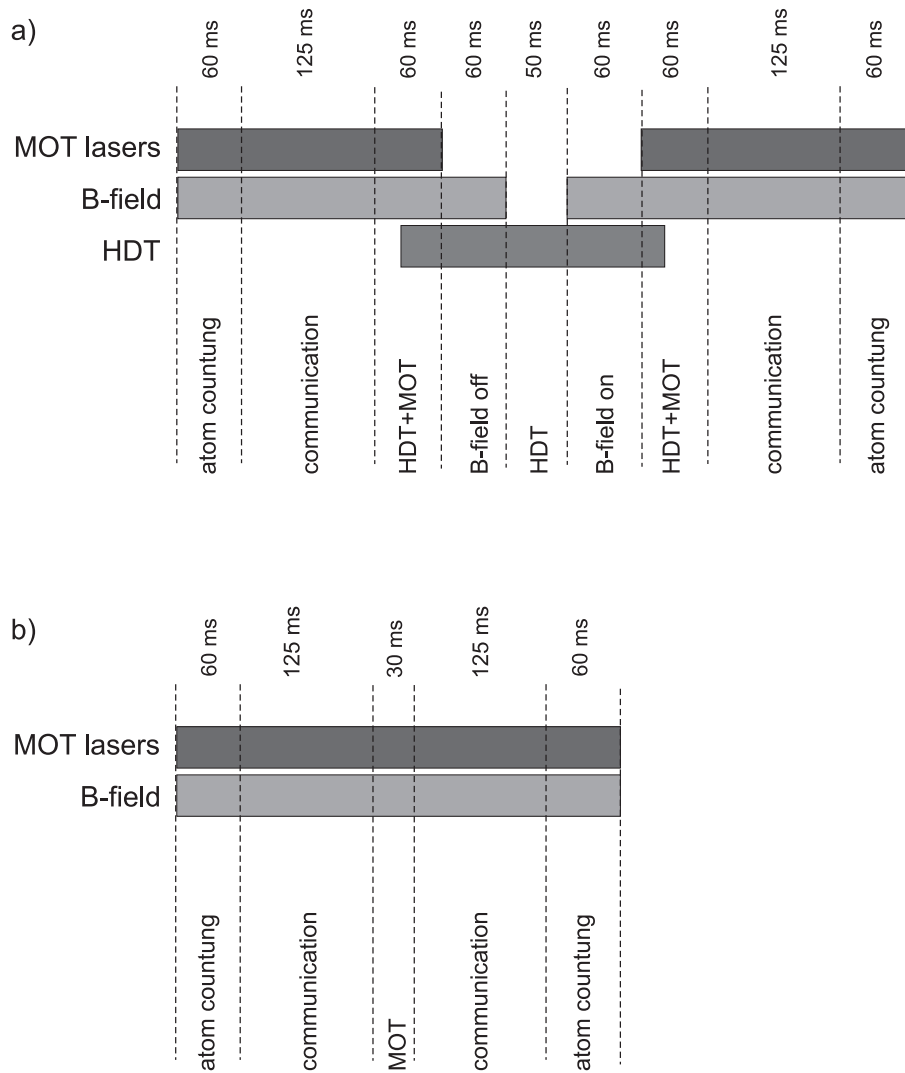


Figure 3.2: Experimental sequences of the preparation efficiency measurement. a) After counting the atoms, they are transferred from the MOT into the HDT and the magnetic field gradient is switched off. The atoms are then stored in the HDT. Finally, the magnetic field gradient is switched on and the atoms are transferred back into the MOT for counting. b) The same sequence but without the steps involving the HDT.

3.2 Experimental results

Figure 3.1 shows the fluorescence histogram from an experiment preparing five atoms. On the input of the discriminator the number of atoms is Poisson distributed, see Fig. 3.1a. Each time Experiment Manager detected five atoms, it has started the following sequence, see Fig. 3.2a: The atoms were first transferred into the HDT by overlapping both traps for 45 ms (the shutter delay is 15 ms). The MOT was then switched off, keeping the atoms for 50 ms in the HDT only. Since the atom counting in the HDT is not effective,

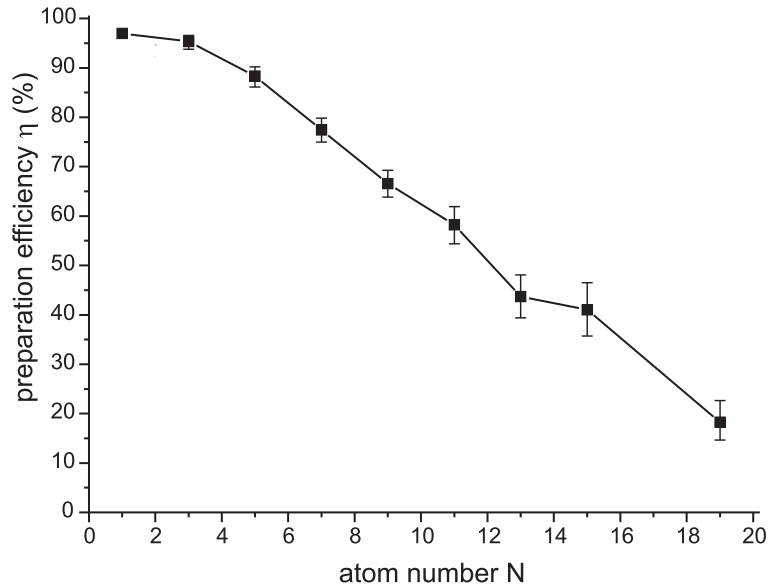


Figure 3.3: Efficiency of the preparation of N atoms in the HDT. Each point is the result of 300 successful detections of exactly N atoms by the discriminator.

see Sec. 2.2.5, we finally transfer the atoms back into the MOT. The resulting histogram of the photon counts is shown in Fig. 3.1b.

The peak corresponding to five atoms contains $\eta = 88\%$ of all events. In the other events atoms have been lost or an additional atom has been captured. This percentage η we define as five atom *preparation efficiency*. Because the atoms have to be transferred back into the MOT for counting, η is a lower bound for the probability of preparing the desired number of atoms in the dipole trap. For comparison, without the number-locked loading, the preparation efficiency for $N = 5$ atoms in the HDT is a factor of five smaller due to Poissonian fluctuations.

We have measured the preparation efficiency with our number-locked loading method for up to $N = 19$ atoms shown in Fig. 3.3. For each N , the average number of atoms loaded into the MOT from the background gas was accordingly adjusted.

3.3 Analysis

In order to study which factors limit the preparation efficiency in the HDT, we have analyzed the contributions to the preparation efficiency from all the steps of the process: preparation of the desired number of atoms in the MOT, transfer of these atoms into the HDT, holding the atoms in the HDT, reloading of the atoms back into the MOT, and keeping the atoms in the MOT for counting, see Fig. 3.2a.

3.3.1 Loss mechanisms

In the MOT

The determination of the current number of atoms in the MOT takes 60 ms. If the the number equals to the desired number, the main experimental sequence is started. The communication between the computer control programs additionally takes about 125 ms. The same holds for reloading atoms back from the HDT into the MOT. During this time $\Delta t_{\text{MOT}} = 370$ ms the atoms are stored in the high gradient MOT, and the number of atoms in the MOT can change due to single atom events, i. e., collisions with the background gas or capture of an additional atom from the background gas, and due to two-atoms collisions.

Collisions with the background gas and capturing. The probability that one atom is lost from the MOT due to a background gas collision increases with time as

$$p_{\text{backgr}}(t) = 1 - \exp\left(-\frac{t}{\tau_{\text{backgr}}}\right), \quad (3.1)$$

where the time constant of this process is $\tau_{\text{backgr}} \approx 55$ s, see Ch. 2. The same law holds for the probability to capture an atom from the background vapor:

$$p_{\text{capture}}(t) = 1 - \exp\left(-\frac{t}{\tau_{\text{capture}}}\right) \quad (3.2)$$

with the time constant $\tau_{\text{capture}} \approx 33$ s. Since both time constants are more than an order of magnitude smaller than Δt_{MOT} , these processes play only a minor role to the reduction of the preparation efficiency at this step.

Two-atom losses. The main contribution comes from two-atom collisions. This fact can be already seen from Fig. 3.1b. Here, if the peak corresponding to the two-atom losses stemmed from two uncorrelated single atom losses, then this peak should be quadratically smaller than the single atom losses peak, which is not the case. Therefore, the two-atom loss peak is the result of inelastic two-atom collisions such as fine structure changing collisions, radiative escape or hyper fine state changing collisions.

During a binary cold collision, two atoms approach each other, and as the interatomic separation R becomes small (< 1000 Å), the molecular interactions between the atoms start playing a role. The asymptotic dependency of the molecular potential depends on the atomic internal state. If both atoms are in the ground state, the interaction is between two induced dipole moments. This is known as Van-der-Waals potential. If one of the atoms is in the excited- and the other in the ground state, the interaction is described by the resonant dipole-dipole interaction.

- *Hyper fine state changing collisions* Consider two Cs atoms in the ground $^2S_{1/2}$ state approaching each other on one of the quasimolecular curves. The simplified picture of the ground state potentials including the hyperfine splitting between $F = 4$ and $F = 3$ levels is presented in Fig. 3.4. The attractive and repulsive quasimolecular curves cross at the interatomic separation at about 30 Å. If the atoms during the

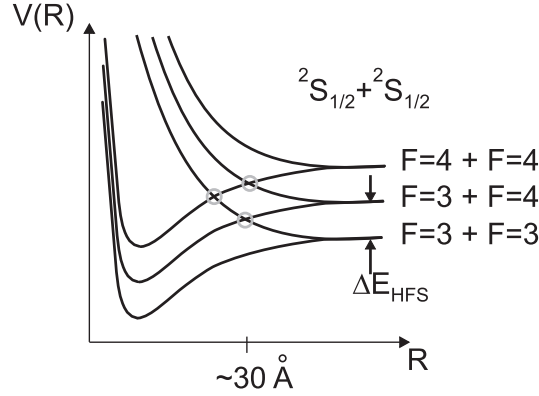


Figure 3.4: Schematic presentation of ground state collisions between two atoms. Two atoms in the ground state $S + S$ approach each other on one of the attractive quasimolecular potential curves. If the atoms reach the separation of the level crossings (circles), the hyper fine structure state of the “quasimolecule” changes. As the result, the atoms gain the energy ΔE_{HFS} and leave the collision region on the repulsive quasimolecular potential.

approach change the asymptote from the attractive to the repulsive one at one of the crossings, this will result in the release of energy corresponding to the single/double hyperfine splitting of $\Delta E_{\text{HFS}}/h = 9.2$ GHz, depending on the asymptote. This process is called a hyper fine state changing collision (HCC). The released energy corresponds to

$$\Delta E_{\text{HFS}}/2k_{\text{B}} = 0.22 \text{ K}$$

per atom for a single ΔE_{HFS} transition, which is on the order of the MOT escape energy. In the previous work [46], the MOT escape energy was measured to be $E_{\text{MOT}} = 0.2$ K, resulting in the loss of all products of this collision. The corresponding collision rate was about $\beta_{\text{HCC}} \approx 2 \cdot 10^{-11} \text{ cm}^3\text{s}^{-1}$ [46]. In our case, the MOT escape energy is on the same order of magnitude, but not known with precision enough to conclude whether all the products of the HCC collision are lost or recaptured by the MOT.

These collisions can take place without presence of an external laser field. The next two collision processes are light induced. For simplicity, we neglect the hyperfine splitting in the following.

- *Fine structure changing collisions* A colliding atom pair, initially with both atoms in the ground state moving on the $S + S$ -potential curve, absorbs a photon from the cooling laser to a strongly attractive excited state potential curve, see Fig. 3.5. The atoms are then accelerated towards each other on the $S + P_{3/2}$ -curve. If the atoms approach each other to a distance R_{FCC} , see Fig. 3.5a, before they spontaneously emit a photon, the change of the fine structure state can take place. The atoms then can leave the near-field region on the $S + P_{1/2}$ quasi-molecular potential. The released energy $\Delta E_{\text{FCC}} = E(P_{3/2}) - E(P_{1/2})$ is then equally distributed between

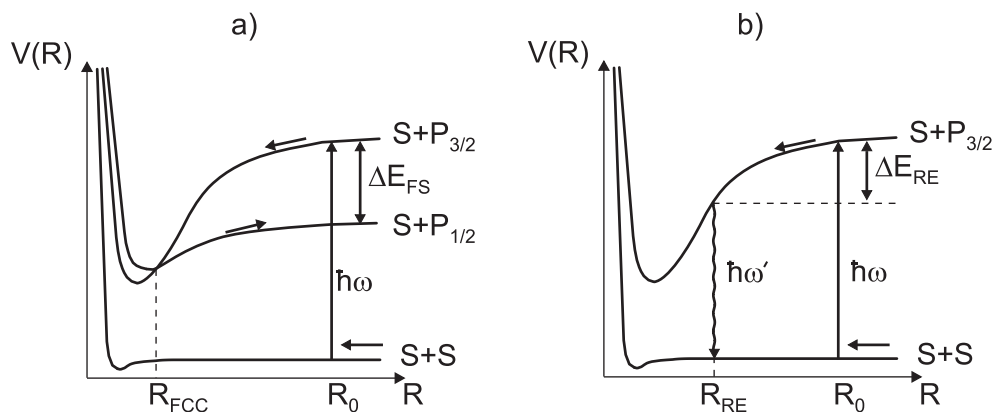


Figure 3.5: Schematic presentation of light induced collisions between two atoms. An atomic pair in the ground state $S + S$ at the separation R_0 is excited by the cooling laser to the quasimolecular potential $S + P_{3/2}$ at the separation $R_0 \approx 800 \text{ \AA}$. As the result, atoms start accelerating towards each other. a) The atoms reach the separation $R_{FCC} \approx 30 \text{ \AA}$, where the fine structure state of the atomic pair changes. As the result, the atoms leave the near-field region on the channel $S + P_{1/2}$ before the spontaneous emission of a photon takes place. b) If the photon emission takes place before the atoms reach the separation R_{FCC} , the atomic pair leaves the interaction region on the $S + S$ channel.

the two atoms. For Cs atoms

$$\Delta E_{FCC}/2k_B = 400 \text{ K}$$

per atom. Since this energy is much higher than a typical escape energy from the MOT, this process will always result in ejection of the two atoms from the trap. The corresponding collision rate is $\beta_{FCC} \approx 2 \cdot 10^{-11} \text{ cm}^3\text{s}^{-1}$ [46].

- *Radiative escape* If the atoms spontaneously emit a photon during the approach, see Fig. 3.5b, the atoms leave the near field region on the $S + S$ channel. This process is called radiative escape (RE). The released energy $\Delta E_{RE} = \hbar\omega - \hbar\omega'$ depends on the interatomic separation at the moment of the emission. The spectral probability density to release the energy around ΔE_{RE} in this process was shown in the semiclassical approximation [47] to be

$$P_{RE}(\Delta E_{RE}) = \frac{A}{(\Delta E_{RE})^{11/6}} \quad (\text{for } \Delta E_{RE} \gg k_B T), \quad (3.3)$$

where $A = 8.8 \cdot 10^{-25} \text{ J}^{5/6}$ is the weighted average over different collision channels for a Cs quasimolecule given in Table I of [47], T is the temperature of atoms in the MOT. Since the spectrum of the radiative escape is not discrete as for the HCC- and FCC-collision, but is continuous, only part of the collisions that have enough energy to overcome the capturing energy of the MOT will leave the trap. The corresponding loss rate for our trap is $\beta_{RE} \approx 9 \cdot 10^{-11} \text{ cm}^3\text{s}^{-1}$ [46].

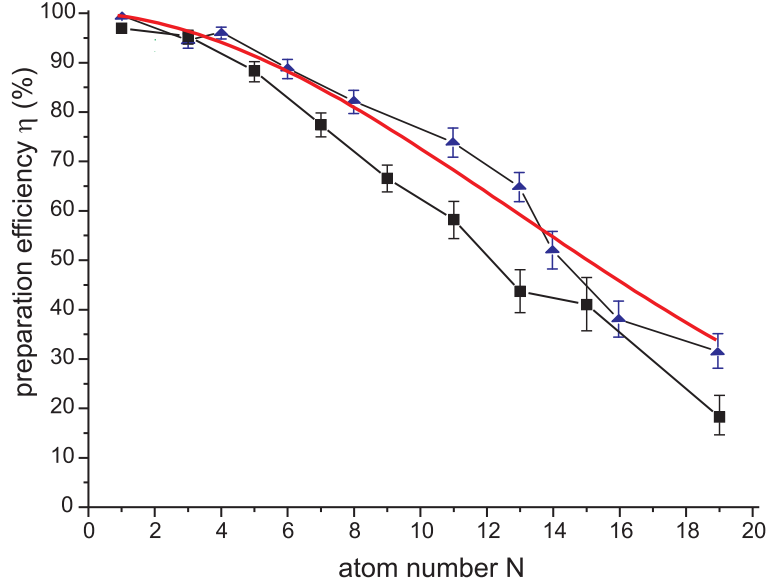


Figure 3.6: Efficiency of the preparation of N atoms in the MOT (triangles) and the corresponding fit. Each point is the result of 300 successful detections of exactly N atoms by the discriminator. For comparison, the preparation efficiency for the HDT from Fig. 3.3 is shown as well (squares).

Since the *loss rates* of all three processes are on the same order of magnitude, the *collision rate* of the RE-collisions is higher. This fact is important for the analysis of the atomic collisional dynamics during the simultaneous operation of the MOT and of the HDT. Since the depth of the HDT is three orders of magnitude smaller than the escape energy of the MOT, the losses from the HDT are dominated by RE-collisions.

The probability that a two-atom collision in the MOT with N atoms takes place during the time t is

$$p_{2\text{MOT}}(N, t) = 1 - \exp\left(-\alpha \frac{N(N-1)}{2} t\right). \quad (3.4)$$

Here the loss rate is

$$\alpha = \beta/V_{\text{MOT}}, \quad (3.5)$$

where V_{MOT} is the effective volume of the MOT and $\beta = (\beta_{\text{HCC}} + \beta_{\text{FCC}} + \beta_{\text{RE}}) \approx 13 \cdot 10^{-11} \text{ cm}^3\text{s}^{-1}$ [46].

Measurement. In order to single out the losses in the MOT, contributing to the reduction of the preparation efficiency, we have repeated the experiment as for Fig. 3.2a, but without the HDT, i. e., preparing N atoms in the MOT. The corresponding experimental sequence is shown in Fig. 3.2b.

Analysis. The result of this experiment is presented in Fig. 3.6 as triangles. For

every number of atoms N in this graph the probability that no atom is lost during the experimental sequence consists of three contributions:

$$\eta_{\text{MOT}}(N) = (1 - p_{\text{capture}}(\Delta t_{\text{MOT}})) \cdot (1 - p_{\text{backgr}}(\Delta t_{\text{MOT}}))^N \cdot (1 - p_{2\text{MOT}}(N, \Delta t_{\text{MOT}})). \quad (3.6)$$

We have fitted this function to the experimental data with α as a free fit parameter. The result for

$$\alpha^{\text{est}} = 0.014(\pm 0.001) \text{ s}^{-1}$$

is shown in Fig. 3.6 as a solid line.

In order to compare this loss coefficient to the literature value, we have to estimate the effective volume of our MOT, see Eq. 3.5. We approximate it with a sphere with the radius of $\sigma = 5.5 \mu\text{m}$, see below. This results in the loss coefficient of

$$\beta = 1 \cdot 10^{-11} \text{ cm}^3\text{s}^{-1}.$$

This value is an order of magnitude smaller than the literature value of $13 \cdot 10^{-11} \text{ cm}^3\text{s}^{-1}$ [46]. Most probably, the the difference is caused by our approximation of V_{MOT} . Another contribution might arise due to higher escape energy of our MOT, relative to 0.2 K from [46]. In this case all products of HCC-collisions and part of the products of RE-collisions are recaptured by the MOT, thereby reducing the two-atom loss rate.

Discussion. For comparison, we have plotted the result of the measurement with the HDT, see Fig. 3.3, as rectangles in the Fig. 3.6. Since the preparation efficiency in the HDT is only slightly differs from the efficiency in the MOT, we can conclude that the losses in the HDT are small. On the other side, the transfer of atoms between the MOT and the HDT involves the near resonant light of the MOT. Therefore, light induced collisions can take place at this step as well. Since the losses due to these collisions are small, but the duration of these steps is comparable, there should be some mechanism of *redistribution* of atoms between the micropotentials of the standing wave of the HDT until they are occupied by at most one atom, and the light induced collisions are no longer possible. We attribute this mechanism to the process of recapture of the products of the two-atom collisions in the HDT by the MOT, during the step of transfer of atoms from the MOT into the HDT, see Fig. 3.7.

In the dipole trap

The steps with the dipole trap in the experimental sequence Fig. 3.2a include the transfer of atoms from the MOT into the HDT, keeping atoms in the dipole trap and reloading back into the MOT. During this time ($\Delta t_{\text{HDT}} = 230 \text{ ms}$) single atoms can be lost due to the collisions with the background gas. During the transfer steps between the MOT and the HDT atoms can be captured by the MOT from the background vapor. In the HDT without the MOT light, FCC-collisions can take place if there are some potential wells occupied by more than one atom and at least one of the atoms is the $F = 4$ ground state.

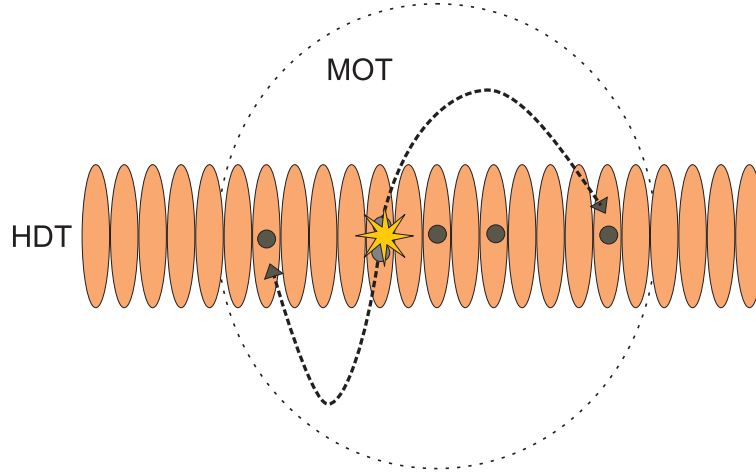


Figure 3.7: Collisional redistribution of atoms. Two atoms trapped in one of the HDT micropotentials collide and leave the HDT. The products of the radiative escape collision are recaptured by the MOT, cooled down and reloaded into the HDT.

Transfer efficiency. Additionally, an atom can be lost during the transfer of atoms between the MOT and the HDT. We have measured it in Sec. 2.2.3 to be

$$p_{\text{transfer}} = 98.7_{-1.1}^{+0.7} \% \quad (3.7)$$

Redistribution. In the experimental sequence, see Fig. 3.2, we transfer atoms from the MOT into the HDT by simultaneously operating these traps for 45 ms. Since the MOT lasers are still operating, all of the above mentioned light induced collisions take place in this step as well.

The difference to the collisions in the MOT arises from the geometry of the traps. In the MOT all atoms have a possibility to collide with each other. In contrast, in the HDT only the atoms trapped inside one micropotential can collide. Moreover, if a collision take place, some products of the collision can be recaptured by the MOT, which cools them and loads them back into the HDT, see Fig. 3.7. If the atoms are loaded into empty HDT micropotentials, there will be no more collisions. Otherwise, the repeats on until the atoms are redistributed or lost.

Theoretical estimation of the redistribution efficiency. Since the rate of the RE-collisions is much higher than rate of other two-atoms collisions, and the depth of the HDT is $U_{\text{HDT}}^0 = 0.8$ mK, which is three orders of magnitude smaller than the escape energy from the MOT, the losses from the HDT are dominated by the losses due to the RE-collisions. We can estimate using Eq. 3.3 that in

$$p_{\text{redist}}^{\text{est}} = \frac{\int_{U_{\text{HDT}}^0}^{E_{\text{MOT}}} P_{\text{RE}}(E) dE}{\int_{U_{\text{HDT}}^0}^{\infty} P_{\text{RE}}(E) dE} = 99.0 \% \quad (3.8)$$

of the cases the products of the RE-loss from the HDT are recaptured by the MOT. This result suggests that the redistribution process should be very effective, if the MOT is

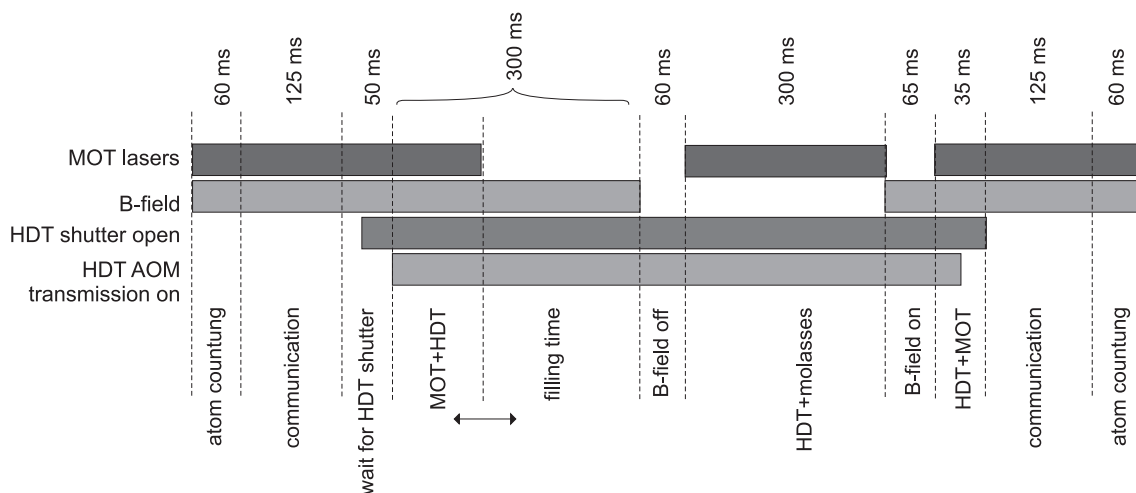


Figure 3.8: Experimental sequence for measurement of the time scale of the MOT induced redistribution process. After counting the atoms, they are transferred from the MOT into the HDT by overlapping the traps. The overlap time is varied between 3 and 300 ms. The filling time is necessary to keep the length of the experimental sequence constant. Then, the magnetic field gradient is switched off. The atoms in the HDT are illuminated by optical molasses during 300 ms to induce two-atom collisions in the HDT. Finally, the magnetic field gradient is switched on and the atoms are transferred back into the MOT for counting.

switched on long enough to redistribute the atoms until there are no multiply-occupied micropotentials any more.

Outline of the time scale measurement procedure. In order to experimentally determine the time scale of this process, the experimental sequence presented in Fig. 3.2 must be modified with a step where doubly occupied micropotentials are emptied. This can be done by illuminating the atoms in the HDT with the optical molasses. During this illumination, the light induced collisions take place, but the products of the collisions are not recaptured. Therefore, such illumination effectively removes atoms from doubly occupied HDT micropotentials, the effect known in literature as collisional blockade [48, 49]. Measuring the preparation efficiency with this modified sequence shown in Fig. 3.8, we should observe, that for increasing overlap times between the HDT and the MOT, the preparation efficiency increases and saturates for overlap times long comparable to the timescale of the redistribution process. In contrast, for shorter times the preparation efficiency will decrease down to the value, corresponding to absence of redistribution.

Estimation of the preparation efficiency for long overlap times. For overlap times longer than the timescale of the redistribution process we expect that the atoms are redistributed between different potential wells of the HDT. Therefore, we do not expect any two atom losses during the illumination of the atoms in the HDT with the optical

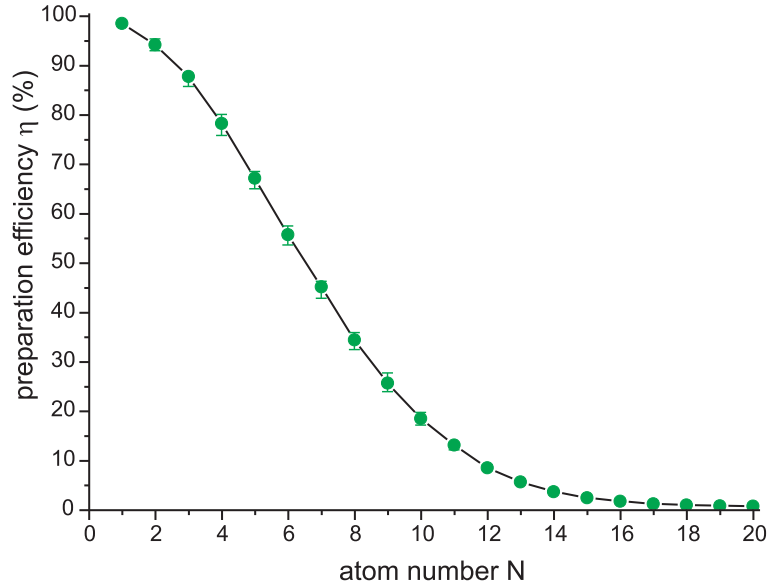


Figure 3.9: Simulated preparation efficiency of atoms in the HDT with the absence of the redistribution during the transfer from the MOT and loss of atoms from the doubly occupied potential wells of the HDT.

molasses. Consequently, in this case the preparation efficiency in the HDT should be comparable to the preparation efficiency presented in Fig. 3.3 using the experimental sequence Fig. 3.2a.

Estimation of the preparation efficiency for short overlap times. For short overlap times we expect that the redistribution does not take place. Therefore, the potential wells of the HDT, containing pairs of atoms, will be emptied during the illumination with the molasses. We have carried out a Monte-Carlo simulation to estimate distribution of atoms in the potential wells of the HDT after the transfer from the MOT.

We assume that the spatial distribution of atoms along the axis of the HDT after transfer from the MOT is Gaussian with $\sigma = 5.5 \mu\text{m}$. This size was measured by transferring single atoms from the MOT into the HDT, and then calculating the standard deviation of their positions.

In our simulation N atoms were placed into the potential wells of the HDT separated by 532 nm at positions randomly distributed according to the Gaussian probability distribution with $\sigma = 5.5 \mu\text{m}$. If there were two atoms in one well, this pair of atoms was removed from the HDT, simulating the absence of recapturing. By repeating this procedure for 2000 times for every N , the corresponding probability $\eta_{\text{molasses}}(N)$ of not losing any atom was computed.

The resulting preparation efficiency was then calculated as

$$\eta(N) = \eta_{\text{molasses}}(N) \cdot \eta_{\text{MOT}}(N) \cdot p_{\text{transfer}}^N. \quad (3.9)$$

The result is presented in Fig. 3.9, which gives us the estimation of the expected

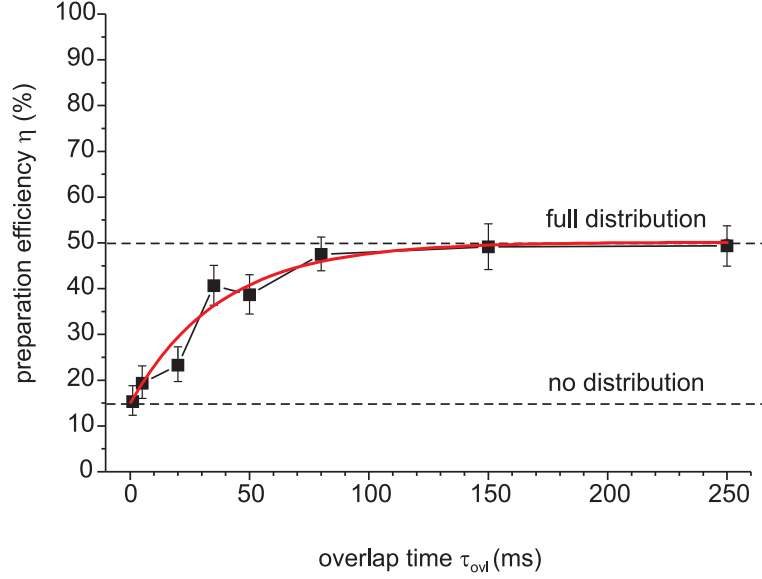


Figure 3.10: Dependence of the preparation efficiency on the overlap time between the MOT and the HDT for $N = 10$ atoms.

preparation efficiency for the experiment presented in Fig. 3.8 for the case of very short overlap times, i. e., of no redistribution.

Measurement of the time scale. We have measured the preparation efficiency for $N = 10$ atoms and varied the overlap time between 3 and 250 ms. In order to control it with the millisecond precision, we have used the AOMs of the HDT instead of the mechanical shutter to switch on the dipole trap. The atoms were then illuminated in the HDT with the optical molasses for 300 ms. Finally, they were transferred back into the MOT for counting, see Fig. 3.8. Figure 3.10 shows the result of this experiment.

Analysis. In Fig. 3.10 we see the expected saturation of the preparation efficiency for long times at $\eta_{\text{meas}}^{\text{long}} = 49^{+4}_{-4}$ %, which reasonably agrees with the expected $\eta_{\text{th}}^{\text{long}} \approx 60$ % for $N = 10$, see Fig. 3.3. For short overlap times, the preparation efficiency goes to a value of $\eta_{\text{meas}}^{\text{short}} = 15^{+4}_{-3}$ % at $\tau_{\text{ovl}} = 1$ ms, which agrees with the expected $\eta_{\text{th}}^{\text{short}} = 19(\pm 1)$ % for $N = 10$, see Fig. 3.9.

In order to be sure that this short time is enough for the efficient transfer of atoms from the MOT into the HDT, we have measured the single atom transfer efficiency for an overlap time of $\tau_{\text{ovl}} = 1$ ms to be $98.5^{+1.0}_{-1.5}$ %. This efficiency includes the transfer from the MOT into the HDT and back into the MOT for counting.

In order to estimate the timescale $\tau_{\text{redist}}^{\text{est}}$ of this process we have fitted the experimental data with the exponential function

$$\eta(\tau_{\text{ovl}}) = a \left[b - \exp\left(-\frac{\tau_{\text{ovl}}}{\tau_{\text{redistr}}^{\text{est}}}\right) \right] \quad (3.10)$$

with the free fit parameters a , b and $\tau_{\text{redistr}}^{\text{est}}$. The result of the fit with

$$a = 0.36(\pm 0.04), \quad b = 1.4(\pm 0.1) \quad \text{and} \quad \tau_{\text{redistr}}^{\text{est}} = 38(\pm 10) \text{ ms}$$

is presented as a solid line in Fig. 3.10. This time scale is compatible with the time constant of the light induced collisions in our HDT of $\tau_{\text{HDT}}^{\text{fit}} = 44(\pm 2)$ ms, see Fig. 4.25, where we have illuminated atoms in the HDT with the optical molasses and observed atomic losses on the decay of the fluorescence signal, see Sec. 4.8.2. The similarity of the timescales in these two experiments suggest that in Fig. 3.10 we observe a MOT assisted redistribution of atoms in the HDT.

Discussion

We can conclude that the reduction of the efficiency of preparing N atoms in the HDT is mainly caused by the losses in the MOT. Therefore, a reduction of the time which the atoms spend in the MOT, either the communication time between the programs of the computer control, or the APD integration time, will result in an increase of the preparation efficiency in the HDT. Physical effects such as “optical shielding” due to the repump laser [50], due to an additional “catalyst laser” [51] or due to the dipole trap laser [52] can be used as well to reduce the rate of two-atom losses.

Although the model of the low loss MOT assisted redistribution of atoms in the HDT allows us to quantitatively explain the results of our measurements, this is only an indirect experimental demonstration of this process. The final proof is a direct observation of the reduction of two atom losses as a function of the of the overlap time between the MOT and the HDT, see Fig. 3.10.

3.3.2 Quantitative study of atom losses

We have carried out a Monte-Carlo simulation of atom loss dynamics during the experiments, corresponding to the experimental sequences: measurement of the preparation efficiency in the HDT as the function of the number of atoms N (“HDT-sequence”), see Fig. 3.2a, the preparation efficiency in the MOT (“MOT-sequence”), see Fig. 3.2b, and the sequence for measuring the dependency of the preparation efficiency on the overlap time τ_{ovl} between the MOT and HDT (“overlap-sequence”), see Fig. 3.8. Finally, we compare the results of this simulation to the experimental data.

Outline of the algorithm

In order to calculate the probability of no loss during execution of the experimental sequence, in principal we have to divide the whole experimental sequence into infinitesimally short time bins and calculate the probabilities of no losses during each time interval. These probabilities for the whole sequence then have to be multiplied in order to calculate the probability of no loss during the whole experimental sequence, i. e., the preparation efficiency η . Physically this means that the time steps have to be much shorter the time between two loss events. Since the probabilities we calculate for each step are conditional

probabilities, which physically means that the probability of the collision on the current step depends on the result of the collisions in the previous steps, we have to calculate the final probabilities for all possible configurations during the process and sum them up with the corresponding statistical weights. Although the calculation of the corresponding conditional probabilities is straightforward, the analytic calculation of the weights of all different outcomes is non trivial. We overcome this difficulty by using a Monte-Carlo simulation.

In order to numerically simulate the loss processes, we divide the whole experimental sequence into time intervals $\Delta t = 5$ ms. The probability that any loss process takes place during this time is quite low and the probability that more than one such losses take place during this time is negligibly small, thereby fulfilling the above mentioned condition.

Parametrization of the physical processes

We have numerically taken into account all the processes leading to a change of the number of trapped atoms during the time interval Δt by parameterizing them with the corresponding probabilities:

- the probability that one atom is lost due to the the background gas collisions is $p_{\text{backgr}}(\Delta t)$ with the time constant $\tau_{\text{backgr}} = 55$ s (Eq. 3.1),
- the probability of capturing an atom by the MOT is $p_{\text{capture}}(\Delta t)$ with the time constant $\tau_{\text{capture}} = 33$ s (Eq. 3.2),
- the single transfer efficiency between the MOT and the HDT is p_{transfer} (Eq. 3.7),
- the probability that the MOT recaptures the atoms which have been expelled from the HDT by a Radiative-Escape collision is $p_{\text{redist}}^{\text{mc}}$,
- the probability that a two-atom collision between N atoms in the MOT takes place $p_{2\text{MOT}}(\Delta t, N)$ with the collision rate α^{mc} (Eq. 3.4),
- the probability that an inelastic light induced collision takes place in one micropotential of the HDT containing n atoms is

$$p_{2\text{molasses}}(\Delta t, n) = 1 - \exp\left(-\frac{n(n-1)}{2} \frac{\Delta t}{\tau_{\text{HDT}}^{\text{mc}}}\right),$$

where $\tau_{\text{HDT}}^{\text{mc}}$ is the time scale of this process.

Moreover, we have included in our simulation the probability that after a light induced collision in the MOT only one atom is lost as $p_{1\text{MOT}}$. Although up to date there is no theoretical explanation of this process, there is an experimental evidence that in our high gradient MOT such processes take place [46, 50]. In analogy, the same kind of process can take place in the HDT under the illumination with the optical molasses. We have included this process in our simulation as the probability $p_{1\text{molasses}}$ that after a light induced collision in the HDT one of the collided atoms stays trapped.

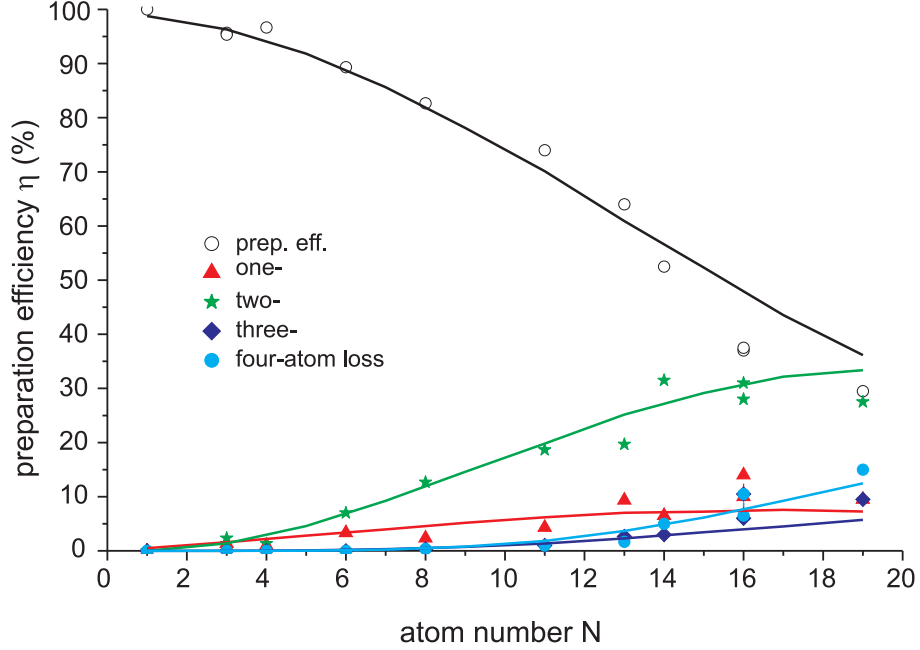


Figure 3.11: Simulation of the preparation efficiency of the atoms in the MOT (open circles). Additionally, the probabilities of one-, two-, three- and four-atom losses are shown. The result of the simulation is shown as solid lines.

We fix the time scales of the background gas collisions τ_{backgr} and of capturing τ_{capture} , whereas the rest of the parameters: $p_{\text{transfer}}^{\text{mc}}$, $p_{\text{redist}}^{\text{mc}}$, α^{mc} , $\tau_{\text{HDT}}^{\text{mc}}$, $p_{1\text{MOT}}$ and $p_{1\text{molasses}}$ we determine from the fit of the model to the experimental data.

Simulation

We have executed this simulation for the three experimental sequences described above. A computer program, realizing this algorithm, was written by one of my co-workers, Leonid Förster. The simulation was repeated 10^5 times for every atom number N from 1 to 19, and for τ_{ovl} from 0 ms to 250 ms, respectively.

Our prime goal is to describe the atom loss dynamics in the overlap-sequence. Nevertheless, we use the first two sequences in order to determine and fix part of the fit parameters: α^{mc} , $p_{1\text{MOT}}$, $p_{\text{transfer}}^{\text{mc}}$ and $p_{\text{redist}}^{\text{mc}}$.

MOT-sequence. We have first simulated the result of the MOT-sequence and determined the parameters α^{mc} and $p_{1\text{MOT}}$. For this purpose, we have computed the curves for several values of these parameters, and then chosen the best fitting curve, thereby carrying out the fit procedure manually. Since we do not have an analytic expression for the fit function, a calculation of the error bars of the resulting fit parameters is not possible.

The result for

$$\alpha^{\text{mc}} = 0.02 \text{ s}^{-1} \quad \text{and} \quad p_{1\text{MOT}} = 0.1$$

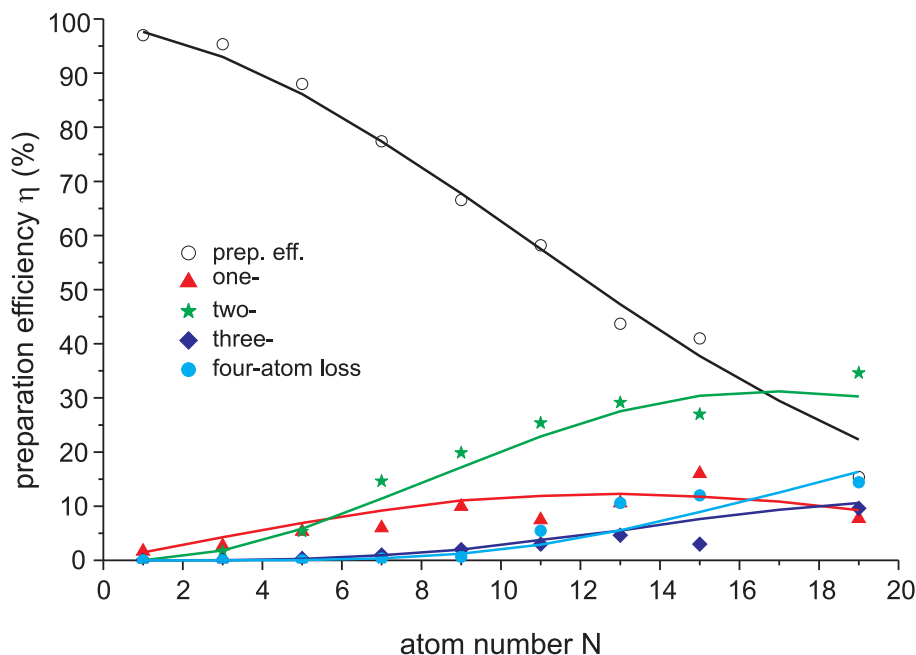


Figure 3.12: Simulation of the preparation efficiency of the atoms in the HDT (open circles). Additionally, the probabilities of one-, two-, three- and four-atoms losses are shown. The result of the simulation is shown as solid lines.

is shown in Fig. 3.11 as solid lines. Here, in addition to the plot in Fig. 3.6, we have also plotted the the experimental one-, two-, three- and four-atom loss probabilities.

HDT-sequence. At the second step, we have fixed the values of α^{mc} and $p_{1\text{MOT}}$ and simulated the HDT-sequence to determine the transfer efficiency between the traps $p_{\text{transfer}}^{\text{mc}}$ and the recapturing probability $p_{\text{redist}}^{\text{mc}}$ during the overlap of the HDT and the MOT. The result for

$$p_{\text{transfer}}^{\text{mc}} = 0.995 \quad \text{and} \quad p_{\text{redist}}^{\text{mc}} = 0.97$$

together with the atom losses is shown in Fig. 3.11 as solid lines.

Overlap-sequence. Finally, we have simulated the expected preparation efficiency for the overlap-sequence. Here, we have fitted $p_{\text{redist}}^{\text{mc}}$, $\tau_{\text{HDT}}^{\text{mc}}$ and $p_{1\text{molasses}}$. The result for

$$p_{\text{redist}}^{\text{mc}} = 0.9, \quad \tau_{\text{HDT}}^{\text{mc}} = 20 \text{ ms} \quad \text{and} \quad p_{1\text{molasses}} = 0$$

is shown in Fig. 3.13.

Analysis

Transfer efficiency. The obtained transfer efficiency of $p_{\text{transfer}}^{\text{mc}} = 99.5\%$ is consistent with the measured efficiency of $98.7_{-1.1}^{+0.7}\%$, see Sec. 2.2.3.

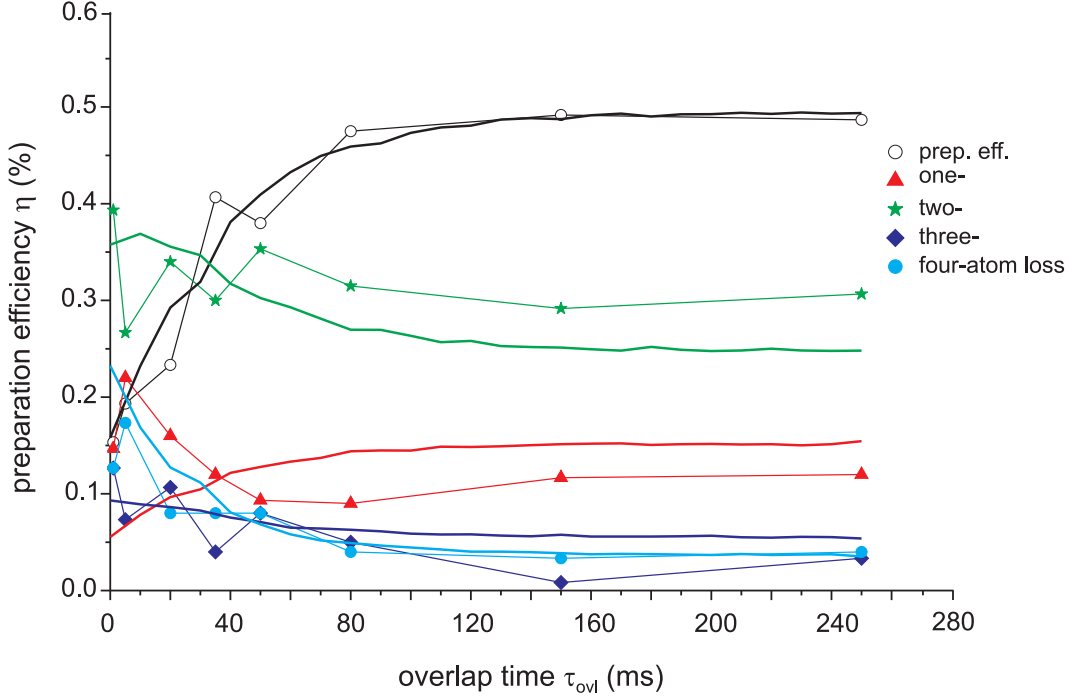


Figure 3.13: Simulation of the preparation efficiency for $N = 10$ as the function of the overlap time between the MOT and the HDT (open circles). Additionally, the probabilities of one-, two-, three- and four-atoms losses are shown. Solid lines show the result of the simulation.

Collision rates. The value of the collision rate in the MOT of $\alpha^{\text{mc}} = 0.02 \text{ s}^{-1}$ obtained in the simulation is somewhat larger than our estimation from the fit of the data in Fig. 3.6 of $\alpha^{\text{est}} = 0.014(\pm 0.001) \text{ s}^{-1}$. The difference can be attributed to the one-atom losses ($p_{1\text{MOT}} \neq 0$). Since not all two-atom collisions result in loss of both atoms, we need more collisions to have the same rate of two-atoms losses.

The resulting time scale of the light induced collisions in the HDT of $\tau_{\text{HDT}}^{\text{mc}} = 20 \text{ ms}$ is somewhat shorter than the result of the fit of the data from Fig. 4.25 of $\tau_{\text{HDT}}^{\text{fit}} = 44(\pm 2) \text{ ms}$. The difference comes from the fact that during the overlap-sequence, the atoms in the HDT are illuminated with the MOT laser beams, whereas in the experiment in Fig. 4.25, the atoms were illuminated with the optical molasses beams, which have less intensity and are further detuned. The fact that the time scale of the redistribution process of $\tau_{\text{redist}}^{\text{mc}} = 38(\pm 10) \text{ ms}$ is larger than $\tau_{\text{HDT}}^{\text{mc}}$ can be attributed to the fact that on average we need more than one collision to redistribute $N = 10$ atoms between different potential wells of the HDT.

Recapturing probability In our simulations we have obtained two different values of the recapturing probability: $p_{\text{redist}}^{\text{mc}} = 0.97$ for the HDT-sequence and $p_{\text{redist}}^{\text{mc}} = 0.9$ for the overlap-sequence. Although these values differ from each other, the general tendency of the expected high recapturing probability holds. The difference can be attributed to the

fact that these values are extracted from the results of two independent measurements and, therefore possibly, under slightly different experimental conditions.

One atom loss after collision in the MOT. The results of our simulations show that the probability that only one atom is lost after a light induced collision in our MOT is non zero, but rather on the order of $p_{1\text{MOT}} \approx 10\%$. The values of 10–30 % have been observed earlier in our MOT [46]. The fact that we do not see such an effect for the optical molasses ($p_{1\text{molasses}} \approx 0$) suggests that this is an effect of recapturing of one of the atoms after the two-atom collision by the MOT.

Atom loss dynamics. Although the results of the simulation show the expected from the redistribution decrease of the two atom losses as the function of the overlap time between the MOT and the HDT, see Fig. 3.13, we do not see this tendency in the experimental data for the two atom losses, see stars in Fig. 3.13.

For short overlap times ($\tau_{\text{ovl}} = 0.40$ ms) the tendency of our simulated curve for one-atom losses completely differs from the tendency of the experimental data, see triangles in Fig. 3.13. The experimental data show first a decrease of the one atom losses, which then slightly increases to a constant value. In contrast, in our simulation we see a monotonic increase of the single atom losses with the time. This increase of the losses with τ_{ovl} can be attributed to the increase of the time the atoms spend in the MOT, which due to $p_{1\text{MOT}} \neq 0$ increases the single-atoms losses.

Moreover, our simulated graph for the two atom losses is systematically lower than the experimental points, whereas the graph for the single atom losses is systematically higher. This indicates that in our model we underestimate the two atom and overestimate the single atom losses. The source might be the fact that we have used the same value of $p_{1\text{MOT}}^{\text{mc}}$ for the analysis of the data of the MOT- and for the overlap-sequence, disregarding that these were two independent measurements.

3.3.3 Conclusion

We have realized a method of number-locked loading of a dipole trap, beating the Poissonian fluctuations by a factor of 2–5. Analysis of the performance of our method, i. e., of the preparation efficiency, shows that light induced inelastic collisions in the MOT are the main factor limiting the performance. Moreover, we have found out that the transfer of atoms from the MOT into the HDT is a reach dynamical process, where light induced collisions between cold atoms play a key role. We found an evidence of a low loss MOT induced process of redistribution of atoms between the micropotentials of the standing wave of the HDT. We have studied this process experimentally and theoretically. Although our experimental data does not allow us to unambiguously conclude about the efficiency of this redistribution, our models, where this process is highly effective, explain most of the experimentally measured data. The presence of such a low loss redistribution mechanism would then open a route towards preparation of an optical lattice with a filling factor very close to one with thermal atoms from the MOT, without preparing a BEC and using a Mott insulator transition.

Chapter 4

Spatial manipulation of individual atoms

Building quantum systems atom-by-atom requires a full control over the spatial position of each building block of the system. We realize this control in three steps: At the beginning, the necessary number of atoms is prepared on our “object holder”, the horizontal dipole trap (HDT). Analysis of an image of these atoms at the second step yields information about the initial spatial positions of the atoms. And finally, using this initial information, we use our “optical tweezers”, the vertical dipole trap (VDT), to extract and place one-by-one the atoms at the target positions on the object holder. The first two steps are extensively described in Ch. 2 and Ch. 3, whereas the question of the spatial manipulation of atoms is the aim of this chapter.

This chapter starts with the explanation of how the transportation of a single atom in all three dimensions using our dipole traps is realized (Sec. 4.1). Since atoms have to be transported over distances up to $100\ \mu\text{m}$ with the submicrometer accuracy, it is essential to obtain a precise calibration of camera pixel separation to atom position in the object plane of the microscope objective (Sec. 4.2). The technique of the extraction of an atom with the optical tweezers out of the HDT is explained and analyzed in Sec. 4.3, whereas the insertion of an atom is the topic of Sec. 4.4. Using this technique we have demonstrated that starting with two initially arbitrary separated atoms in the HDT, we are able to rearrange them to have an atomic pair with a well defined final separation (Sec. 4.6). This technique is then applied to a larger number of atoms to create strings of equidistantly separated atoms (Sec. 4.7). And finally, we demonstrate that two atoms can even be joined in a single potential well of the standing wave of the HDT (Sec. 4.8).

4.1 3D transport of atoms

We transport atoms in the x - y -plane using the HDT. Vertical transport of the atoms along the z -direction is realized by the VDT.

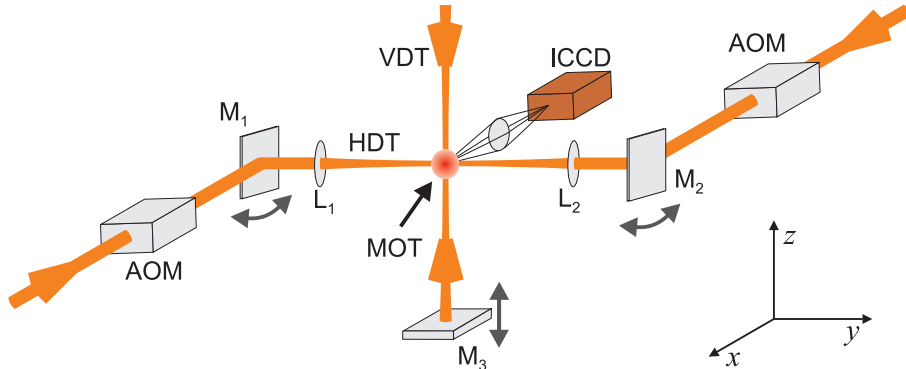


Figure 4.1: Scheme of the experimental setup for atom rearrangement. Atoms in the HDT can be moved along the y -direction using the optical “conveyor belt” technique, whereas the movement in the x -direction is realized by tilting the mirrors M_1 and M_2 . Atoms in the VDT can be transported along the z -direction by moving the retro-reflecting mirror M_3 . The imaging optics is situated perpendicularly to the plane of the traps.

Transportation along the y -direction

An “optical conveyor belt” [6] along the trap axis is realized by means of acousto optic modulators (AOMs) installed in each arm of the HDT, see Fig. 4.1. Mutually detuning the AOM driving frequencies using a dual-frequency synthesizer (model DFD 100 from APE Berlin), detunes the frequencies of the two laser beams by $\Delta\nu = \nu_1 - \nu_2$. As a result, the standing wave moves along the axis of the trap with the velocity $v_y = \lambda\Delta\nu/2$.

We transport an atom by first accelerating the standing wave to a maximum velocity and then decelerating it in the same way to bring the atom to a stop. For this purpose, the frequency difference $\Delta\nu$ is linearly increased to its maximum value in a predetermined time and then decreased to zero in the same time. This results in a uniform acceleration and deceleration during the transportation. Our DFD synthesizer allows us to program up to 8 different transportation distances. Programming a set of new transportation distances takes about 800 ms. Each of them can then be triggered within 2 ms during the experiment. This fact will be important for the analysis of the time necessary for building an equidistant string of seven atoms, see Sec. 4.7.

The optical conveyor belt allows us to transport the atoms over millimeter distances with submicrometer precision [22, 6] within several milliseconds. The accuracy of the transportation distance is limited to 190 nm by the discretisation error of our digital synthesizer [22]. In this experiment we typically transport atoms over a few tens of micrometers within a few hundred microseconds.

Transportation along the x -direction

Translation of the HDT along the x -direction is realized by synchronously tilting the mirrors M_1 and M_2 , see Fig. 4.1, in opposite directions around the z -axis using piezoelectric actuators. For tilt angles smaller than 0.1 mrad the variation of the interference pattern is small and to a good approximation pure x -translation is realized.

Experimentally, the transportation of atoms is realized by linearly ramping the voltage on the actuators, which results in a transportation with the constant speed.

We typically move atoms in the x -direction by two times the waist radius of the HDT (ca. $40 \mu\text{m}$) with a precision of a few micrometers within 50 ms. The maximum transportation distance is limited to about $40 \mu\text{m}$ by the dynamic range of the actuators. The minimal transportation time is limited to about 10 ms by the bandwidth of the PZT-system.

Transportation along the z -direction

The VDT acts as optical tweezers and extracts and reinserts atoms in the z -direction. To axially move the standing wave pattern of the VDT, the retro-reflecting mirror M_3 is mounted on a linear PZT stage (model P-621.10L from PI Germany), see Fig. 4.1.

In our experiments the VDT transports an atom over the distance of $70 \mu\text{m}$ along the z -axis by applying a sinusoidal half wave voltage ramp to the PZT within 50 ms. This transportation distance is more than three waists of the HDT, and therefore is enough for the extraction of an atom out of the HDT, see Sec. 4.3. The precision of the transportation is limited to a few micrometers by the hysteresis of the piezo-crystal, whereas the transportation time is limited by the inertia of the mirror.

4.2 Precise calibration of the imaging scale

Information about the initial positions of the atoms to be manipulated is extracted from an ICCD image. Since atoms have to be transported over large distances up to 1 mm with submicrometer accuracy, it is essential to obtain a precise calibration of camera pixel separation to atom position in the object plane of the microscope objective.

Already from the design of the imaging system this correspondence can be estimated from the optical magnification of the system to be $\alpha_{\text{magn}} = 0.47(\pm 0.05) \mu\text{m}/\text{pixel}$, see Sec. 2.1.2. But the 10 % error in the calibration results already in the $10 \mu\text{m}$ uncertainty for the $100 \mu\text{m}$ transportation distance. Therefore, we have used two other calibration methods to reduce this uncertainty.

4.2.1 Using transportation

For this method we use our possibility to transport atoms with our optical conveyor belt along the y -direction over any desired distance with submicrometer precision. By taking the images of the atom before and after the transport we are thus able to find the correspondence between the known transportation distance and the distance in pixels on the ICCD.

We load exactly one atom into the HDT and transport it over a fixed distance of $15 \lambda_{\text{HDT}}$. The transportation distance in pixels from about 50 transports is $31.99(\pm 0.13)$. The resulting calibration parameter is thus

$$\alpha_{\text{trans}} = 0.499(\pm 0.002) \mu\text{m}/\text{pixel}.$$

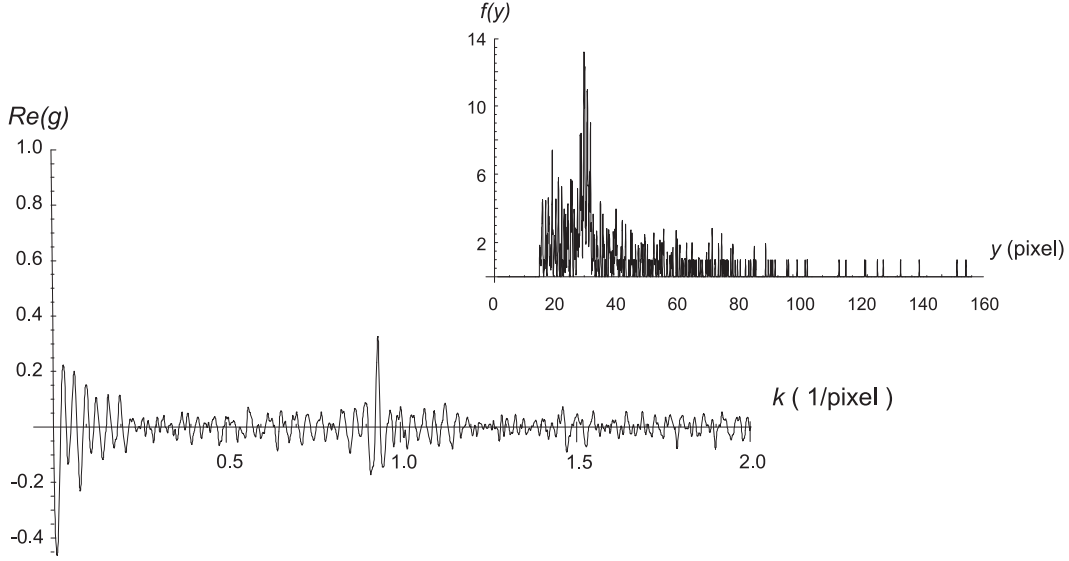


Figure 4.2: Histogram of measured distances and its fourier transform. The only one prominent contribution at $k_0 = 0.9336$ wells/pixel corresponds to the periodicity of $\lambda_{\text{HDT}}/2$ in the object plane of the microscope objective. The inset shows the original function $f(y)$. Here, for presentation purposes each delta function was replaced by a Gaussian with the width of 0.05 pixel.

This value is compatible with the estimation α_{magn} , but the precision is now an order of magnitude better.

4.2.2 Using periodicity of the HDT

For this calibration we take advantage of the fact that the atoms in the HDT are trapped in the potential minima separated by exactly $\lambda_{\text{HDT}}/2 = 532$ nm. Therefore, the measured distance between two simultaneously trapped atoms d given in units of camera pixels must correspond to an integer multiple of $\lambda_{\text{HDT}}/2$ in the object plane:

$$\alpha d = n\lambda_{\text{HDT}}/2, \quad (4.1)$$

where α is the calibration parameter in $\mu\text{m}/\text{pixel}$. In order to determine α we have first accumulated about 500 images with two to four atoms trapped in the HDT. Then we have determined the interatomic separations in each image, resulting in $n \approx 700$ distance values d_i , shown in Fig. 4.2. In order to avoid any inaccuracy caused by overlapping peaks at short distances, only separations of more than $10 \mu\text{m}$ then were taken into account. To find the periodicity of the distribution we construct a function built by summing the delta functions at the positions of each d_i

$$f(y) = \frac{1}{n} \sum_{i=1}^n \delta(d_i - y) \quad (4.2)$$

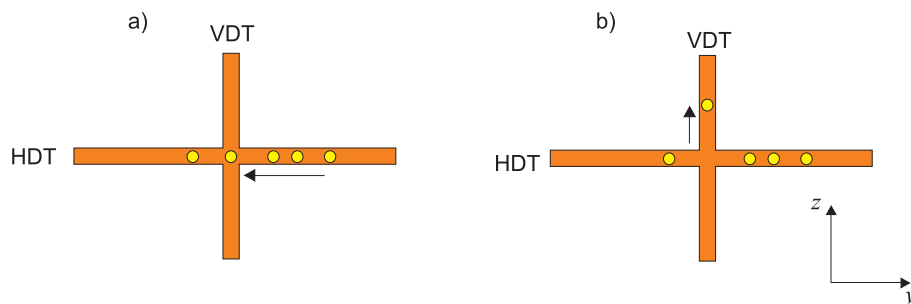


Figure 4.3: Extraction of an individual atom out of the string. a) The target atom is transported to the position of the VDT. b) By axially moving the VDT, the target atom is extracted out of the HDT.

and Fourier transform it:

$$g(k) = \frac{1}{\sqrt{2\pi}} \int_{-\infty}^{\infty} f(y) e^{2\pi i k y} dy = \frac{1}{\sqrt{2\pi}} \sum_{i=1}^n e^{2\pi i k d_i}. \quad (4.3)$$

The real part of the Fourier transform of $g(k)$ is shown in Fig. 4.2. The most prominent peak at $k_0 = 0.9336(\pm 0.0003)$ 1/pixel corresponds to the spatial frequency of the standing wave pattern:

$$k = \frac{\alpha}{\lambda_{\text{HDT}}/2}. \quad (4.4)$$

This yields the calibration parameter $\alpha = 0.4967(\pm 0.0002)$ $\mu\text{m}/\text{pixel}$.

The error of this value is dominated by the statistical error due to the finite sample and the 130 nm-uncertainty in the determination of each distance [22]. The statistical error is estimated by randomly selecting a subset of $n/2$ distances and determining α by the above mentioned calculations on this subset. Using 20 different subsets the standard deviation $(\delta\alpha)_{n/2}$ was determined. The statistical error for the full set is therefore $(\delta\alpha)_n = (\delta\alpha)_{n/2}/\sqrt{2}$. The slight modification of the wave length λ_{HDT} in the Rayleigh zone by the Guoy phase is on the order of 10^{-5} and hence negligible here.

4.2.3 Conclusion

Both methods give a precision enough for the transportation with submicrometer precision. The transportation method is relatively fast to implement and straightforward to analyze. In contrast, the Fourier analysis method is more involved, but yields an order of magnitude higher precision of the calibration parameter. Therefore, we have used the transportation method for all experiments in this thesis. We have used the Fourier method for the analysis of the experimental data of the distance control experiment, see Sec. 4.6.

4.3 Extraction of an atom

Knowing the initial positions of the atoms in the HDT, atoms can be selectively extracted with the optical tweezers. For extraction, the VDT-optical tweezers needs to overcome the

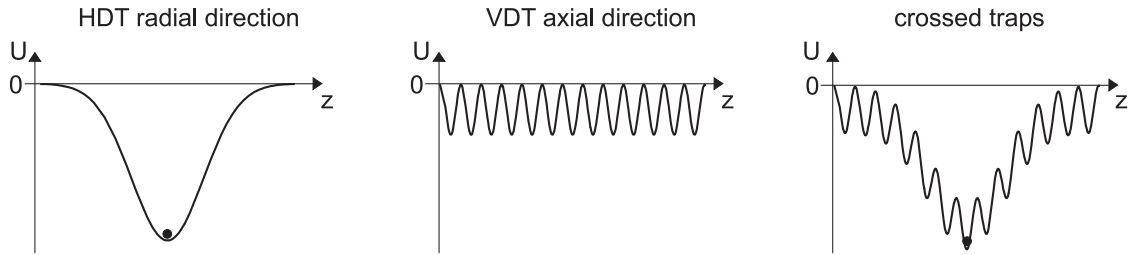


Figure 4.4: Trapping potentials along the z -axis. The trapping potential in the overlap region of the two traps is the sum of the Gaussian profile of the radial confining potential of the HDT and of the standing wave of the VDT. An atom at the bottom of the HDT experiences light forces of the standing wave, too.

HDT trapping forces. In both the HDT and VDT standing wave dipole traps confinement in the axial direction is almost two orders of magnitude tighter than in the radial direction, the maximal axial forces are thus much larger than the radial forces. For comparable potential depths of the HDT and the VDT, an atom in the overlap region will therefore always follow the axial motion of the traps.

We extract a selected atom out of the string trapped in the HDT, by first transporting the target atom to the position of the VDT, see Fig. 4.3a, followed by switching on the VDT adiabatically and moving its standing wave pattern upwards in the z -direction, see Fig. 4.3b. Successful extraction of a single atom not only requires efficient handling of the atoms between the HDT and VDT traps. In addition, other atoms present in the vicinity must remain undisturbed. We have thus defined and analyzed a minimal separation of atoms tolerable on extraction, which is equivalent to an effective “width of the optical tweezers”.

4.3.1 Theoretical model of the width of the optical tweezers

For extraction by the optical tweezers, motion occurs in the y - z -plane only. A two-dimensional model is used to analyze the extraction operation of an atom. In this model motion in the traps is treated classically, for at the atomic temperature of about $60 \mu\text{K}$ for the typical depths of the traps in our experiments the mean oscillatory quantum numbers are $n_{\text{rad}} \approx 90$, $n_{\text{ax}} \approx 3$ for the VDT, and $n_{\text{rad}} \approx 400$, $n_{\text{ax}} \approx 6$ for the HDT.

We consider two crossed standing wave optical dipole traps. For simplicity, we assume that all the spatial manipulations are carried out within the Rayleigh-range of the standing wave dipole traps, i. e., we neglect the change of the curvature of the wave fronts. In this approximation, each dipole trap is described by three parameters: the waist radius of the Gaussian beam, the depth of the trap, and the periodicity of the standing wave. Atoms are trapped in the different potential wells of the standing wave of the HDT and are extracted along the z -direction with the VDT. Therefore, we consider one-dimensional potentials along the z -axis at different y -positions in the y - z -plane with $x = 0$.

In order to separate the effect of the potential shape and the atomic motion on the process of extraction, we first model the case of atoms at zero temperature, where the energy of the atoms is well defined. Then, the influence of the thermal energy distribution

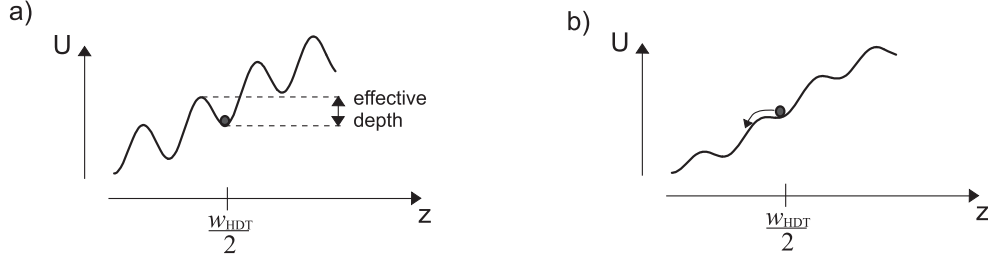


Figure 4.5: Decrease of the effective depth of the potential well. Due to the Gaussian shape of the confining potential of the HDT in the z -direction, the depth of the standing wave pattern reaches its minimum at the distance $w_{\text{HDT}}/2$ from the axis of the HDT. If the effective depth is larger than zero, the atom remains trapped in the standing wave and will be finally extracted with the VDT a). If the depth is smaller, the atom always rolls down during the extraction b).

is discussed.

Tweezers potential

Consider an atom at rest trapped at the bottom of a micro-potential of the HDT at $y = 0$, which coincides with the axis of the VDT. At this position the HDT-potential in the z -direction has a Gaussian shape with waist w_{HDT} and depth U_{HDT}^0 . After switching on the VDT, in addition to the Gaussian potential of the HDT, a periodic potential with depth U_{VDT}^0 and period $\lambda_{\text{VDT}}/2$ is superimposed in the z -direction. Since the HDT and VDT laser frequencies are far apart, the trapping potentials are added incoherently, and the atom is then additionally subject to the forces of the VDT standing wave, see Fig. 4.4.

During extraction of an atom out of the HDT, the VDT is moved axially, causing a shift of the standing wave modulation pattern along the z -direction. The trapped atom is transported at the bottom of one of the local potential minima of the sum potential away from the axis of the HDT. Due to the Gaussian shape of the radial confining potential of the HDT, the depth of the local minima changes along the z -axis and reaches its minimum at the distance $z_{\text{max}} = w_{\text{HDT}}/2$ from the axis of the HDT. The effective depth of the corresponding potential well, see Fig. 4.5, can be approximated as

$$U \approx U_{\text{VDT}}^0 - \frac{1}{\pi\sqrt{e}} \frac{\lambda_{\text{VDT}}}{w_{\text{HDT}}} U_{\text{HDT}}^0, \quad (4.5)$$

The condition that the VDT extracts the atom from the HDT is

$$U > 0. \quad (4.6)$$

Hence, the lower limit for the VDT potential is

$$U_{\text{VDT}}^0 > \frac{1}{\pi\sqrt{e}} \frac{\lambda_{\text{VDT}}}{w_{\text{HDT}}} U_{\text{HDT}}^0. \quad (4.7)$$

Now, consider an atom is trapped at some other position $y \neq 0$ along the HDT. The potential along the z -direction will be the sum of the same Gaussian potential well of

the HDT with depth U_{HDT}^0 and of the periodic potential of the VDT, but now with the reduced depth

$$U_{\text{VDT}}(y) = U_{\text{VDT}}^0 e^{-\frac{2y^2}{w_{\text{VDT}}^2}}. \quad (4.8)$$

The sum of the two potentials at the lateral position y generalizes Eq. 4.5,

$$U(y) \approx U_{\text{VDT}}^0 e^{-\frac{2y^2}{w_{\text{VDT}}^2}} - \frac{1}{\pi\sqrt{e}} \frac{\lambda_{\text{VDT}}}{w_{\text{HDT}}} U_{\text{HDT}}^0. \quad (4.9)$$

Consequently, there exists some region $-y_{\text{T}} < y < y_{\text{T}}$ along the HDT, where condition Eq. 4.6 holds, and where atoms will be extracted with the VDT. Figure 4.6a shows the probability P_{HDT} for an atom to remain trapped in the HDT after the extraction as the function of the lateral position y . The critical position y_{T} defined by the condition $U(y_{\text{T}}) = 0$ is

$$y_{\text{T}} = \frac{w_{\text{VDT}}}{\sqrt{2}} \sqrt{\ln \left(\pi\sqrt{e} \frac{w_{\text{HDT}}}{\lambda_{\text{VDT}}} \frac{U_{\text{VDT}}^0}{U_{\text{HDT}}^0} \right)}, \quad (4.10)$$

which characterizes the width of the optical tweezers, y_{T} , as a function of the trap parameters for atoms at zero temperature. Equation 4.10 shows, that the reduction of U_{VDT}^0 by decreasing the power of the laser beam of the VDT reduces the lateral region y_{T} , from which the atoms will be extracted, thereby reducing the size of the optical tweezers. For $T = 0$ K, i. e., for minimal kinetic energy of the atoms, and neglecting quantum effects, this region can be made arbitrary small at $U_{\text{VDT}}^0 = \frac{\lambda_{\text{VDT}}}{\pi\sqrt{e}w_{\text{HDT}}} U_{\text{HDT}}^0$.

Thermal atomic motion

Let us model atomic motion in the dipole trap by an ensemble in thermal equilibrium at temperature T in a three-dimensional harmonic potential. We assume that the energy of the atoms is Boltzmann-distributed [53]:

$$f(E, T) = \frac{1}{2(k_{\text{B}}T)^3} E^2 e^{-E/(k_{\text{B}}T)}. \quad (4.11)$$

For an atom at fixed energy E the condition for the extraction analogous to Eq. 4.6 is:

$$U(y) - E > 0, \quad (4.12)$$

where $U(y)$ is given by Eq. 4.9. Since for a given temperature T the fraction of atoms with an energy above U is

$$p(U) = \int_{\max\{U, 0\}}^{U_{\text{HDT}}^0} f(E, T) dE, \quad (4.13)$$

the probability P_{HDT} for an atom to remain trapped in the HDT after the extraction as a function of the lateral position y is

$$P_{\text{HDT}}(y) \equiv p(U(y)) = \frac{1}{2} e^{-\frac{U(y)}{k_{\text{B}}T}} \left[\left(\frac{U(y)}{k_{\text{B}}T} + 1 \right)^2 + 1 \right], \quad (4.14)$$

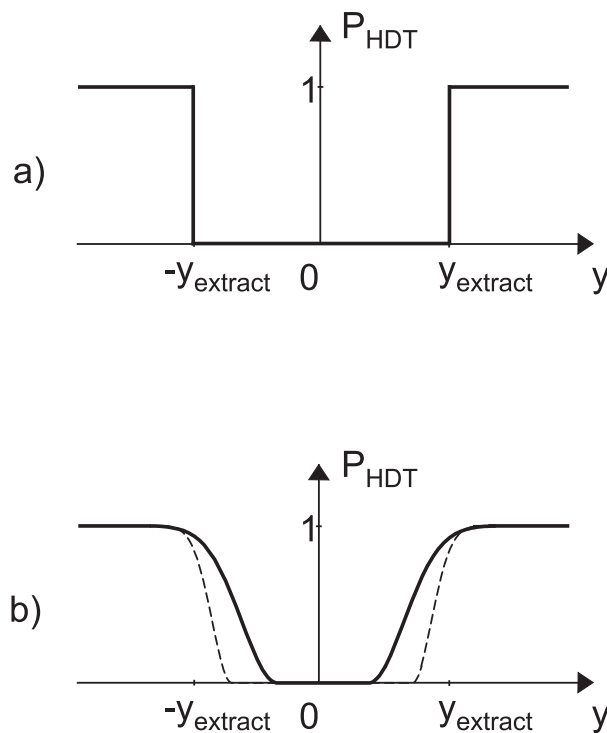


Figure 4.6: Probability for an atom to remain trapped in the HDT after the extraction. a) atoms at $T = 0$ K. b) atoms at temperatures T_1 (solid line) and T_2 (dashed line), with $T_1 > T_2$.

where we have changed the upper limit of the integral from U_{HDT}^0 to infinity in order to get an analytic solution.

Figure 4.6b shows P_{HDT} for the same trap parameters as 4.6a. Atomic motion causes “softening” of the edges of the extraction zone P_{HDT} . An increasing temperature causes narrowing of the region of the efficient extraction. For quantitative analysis we define the minimal width of the optical tweezers $2y_{\text{T}}^{\text{min}}$ such that the extraction efficiency at the center of the VDT is 99 %:

$$P_{\text{HDT}}(y = 0) = 0.01, \quad (4.15)$$

and the probability to extract an atom at $y_{\text{T}}^{\text{min}}$ is 1 %:

$$P_{\text{HDT}}(y_{\text{T}}^{\text{min}}) = 0.99. \quad (4.16)$$

4.3.2 Measurement of the width of the optical tweezers

We have experimentally determined the width $2y_{\text{T}}$ of the optical tweezers as a function of the depth of the VDT by loading the HDT with atoms distributed over a region larger than y_{T} , extracting atoms with the VDT, and analyzing the distribution of the atoms remaining in the HDT.

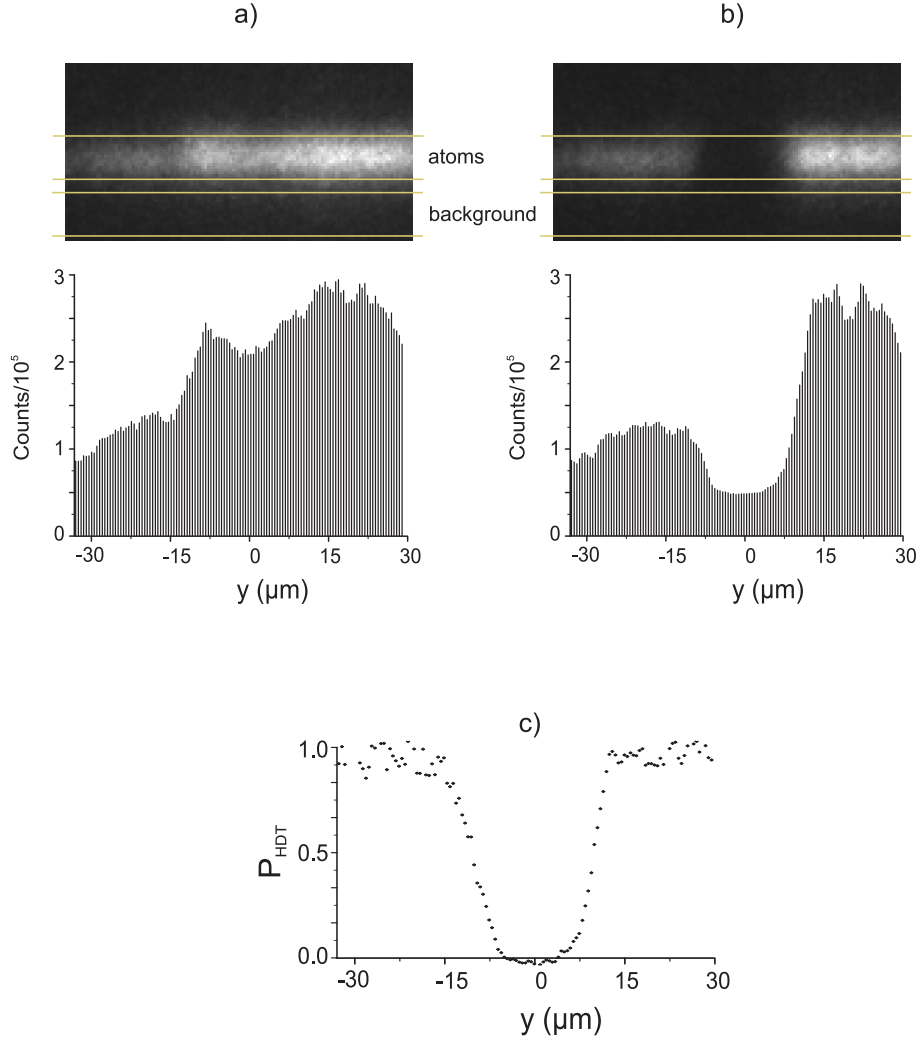


Figure 4.7: Image analysis for the determination of the width of the tweezers. a) The picture shows 40 added images (exposure time 1 s) of about 50 atoms each trapped in the HDT. b) Added images after the extraction of the atoms with the VDT and expelling the extracted atoms. The histograms in a) and b) show the corresponding intensity histograms after the summation of the pixels in the vertical direction in the selected region before the correction for the background. c) The experimentally measured probability for an atom to remain trapped in the HDT P_{HDT} .

Experimental sequence

We have carried out the following experiment: At the first step, a large number of about 50 atoms was loaded into the HDT. Since after the transfer from the MOT, their lateral distribution only extends over the MOT size of about $2\sigma_{\text{MOT}} = 11 \mu\text{m}$, which is already about the waist of the VDT beam, this distribution has been broadened. This was realized by switching off one of the trap laser beams and letting the atoms freely expand along

the HDT axis for $t = 1$ ms. Since the laser beam was switched off within 1 ms, which is adiabatic with respect to the axial oscillation frequency, the atoms were adiabatically cooled to $T_{\text{final}} = \frac{1}{2}T_{\text{init}} \approx 30 \mu\text{K}$ [29]. This results in an average velocity of an atom along the HDT $v_y = \sqrt{k_B T_{\text{final}}/m}$, and therefore in the final spread of the atoms over $2\sqrt{\sigma_{\text{MOT}}^2 + (v_y t)^2} \approx 80 \mu\text{m}$. At the second step, under the continuous illumination of the optical molasses, the first photo of the atoms in the HDT with an integration time of 1 s was taken, see Fig.4.7a. At the third step, the molasses was switched off, the VDT was adiabatically switched on and moved axially, thereby extracting the atoms out of the HDT. At the fourth step, the VDT was switched off to expel the extracted atoms. And finally, the second fluorescence image of the remaining atoms in the HDT was recorded, see Fig.4.7b.

In this measurement, the depth of the HDT was fixed ($U_{\text{HDT}}^0/k_B = 0.8$ mK), whereas the depth of the VDT was changed over two orders of magnitude from 0.3 to 16.8 mK. For better signal-to-noise ratio we repeat this experiment 40 times for each depth of the VDT and add up all initial, see Fig. 4.7a, and all final images, see Fig. 4.7b.

Calculation of P_{HDT}

The experimental P_{HDT} was then calculated from the initial and final images according to the following procedure: After suitably clipping the images to minimize the background noise, see region “atoms” in Fig. 4.7a-b, the pixels of the picture were binned in the z -direction to obtain histograms for the intensity distribution along the axis of the HDT. Each histogram is then corrected for the background noise on the CCD chip. The noise was estimated by binning the pixels of a region of the image of the same size but without the atoms, see region “background” in Fig.4.7a-b. And finally, the probability P_{HDT} was obtained as the normalized final intensity distribution, by dividing the histogram of the final image by the one of the initial image, see Fig.4.7c. The corresponding plots for $U_{\text{VDT}}^0/k_B = 0.3$ mK to 16.8 mK are presented in Fig. 4.8.

4.3.3 Analysis

In Fig. 4.8, the measured data are compared to the theoretical model described by Eq. 4.14. Free fit parameters for the data of Fig. 4.8a include the temperature T of the atoms, the waist of the VDT w_{VDT} along the axis of the HDT, and the position of the VDT y_0 , relative to the picture. The fit to the data set for the depth of the VDT at $U_{\text{VDT}}^0/k_B = 0.3$ mK, corresponding to a power of the incoming VDT laser beam of 0.06 W, yields

$$T = 60(\pm 1) \mu\text{K} \quad \text{and} \quad w_{\text{VDT}} = 11.6(\pm 0.2) \mu\text{m},$$

see Fig. 4.8a. The temperature thus obtained is in the range of the typical temperatures measured by other methods [54]. Also, the measured value of the waist of the VDT along the axial direction of the HDT is in reasonable agreement with the waist $10.1(\pm 1.4) \mu\text{m}$ determined from the oscillation frequency measurements in the VDT. In Fig. 4.8b-h we have plotted the model function $P_{\text{HDT}}(y)$ at $U_{\text{VDT}}^0/k_B = 3.1$ mK, 0.6 mK, 1.1 mK,

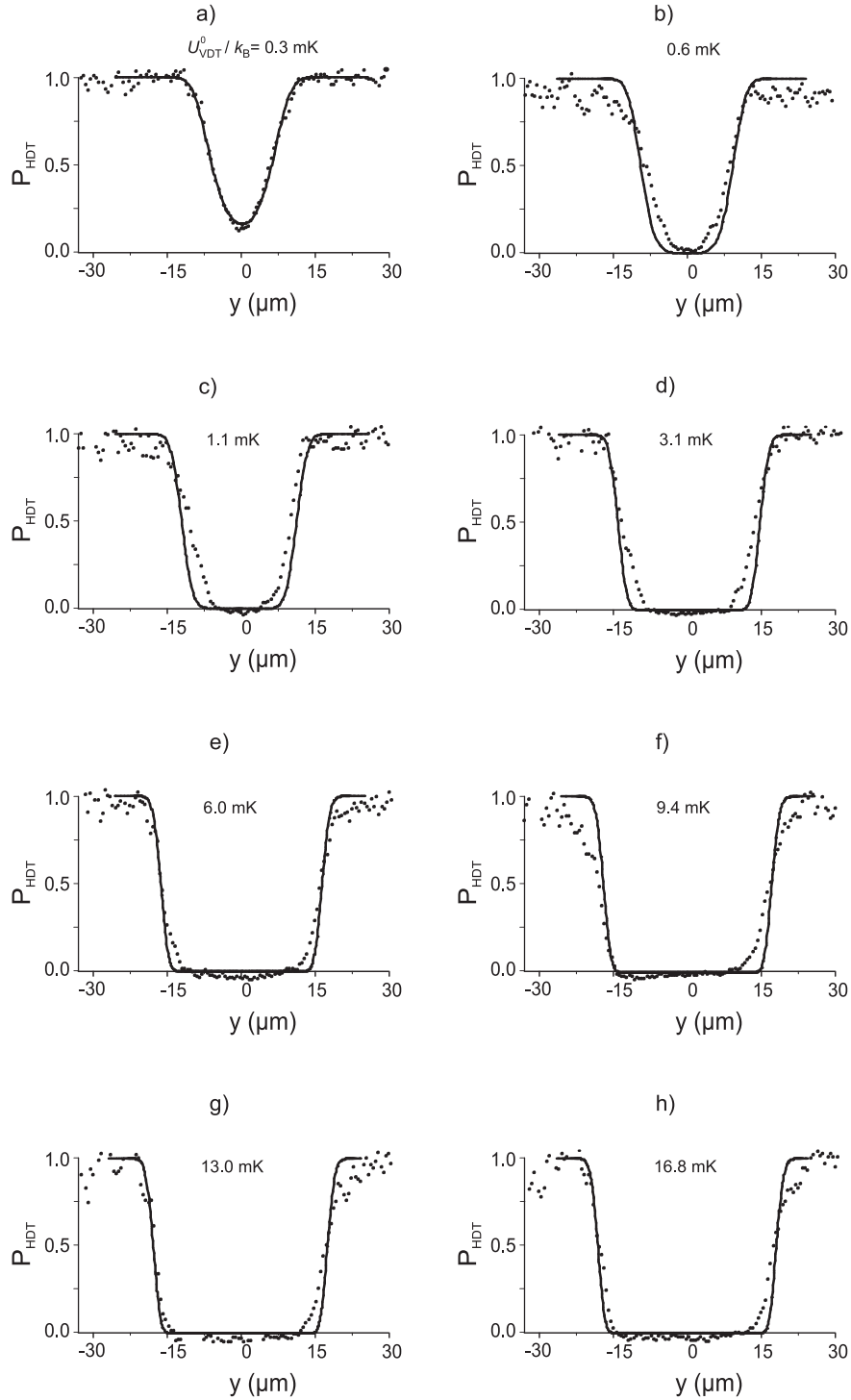


Figure 4.8: Comparison of the experimental data and the respective theoretical expectation. a) Fit of P_{HDT} (solid line) to the experimental data (points) for $U_{\text{VDT}}^0/k_B = 0.3$ mK. b-h) The function P_{HDT} with parameters from a) except $U_{\text{VDT}}^0/k_B = 0.6$ mK, $U_{\text{VDT}}^0/k_B = 1.1$ mK, $U_{\text{VDT}}^0/k_B = 3.1$ mK, $U_{\text{VDT}}^0/k_B = 6.0$ mK, $U_{\text{VDT}}^0/k_B = 9.4$ mK, $U_{\text{VDT}}^0/k_B = 13.0$ mK and $U_{\text{VDT}}^0/k_B = 16.8$ mK, respectively. The depth of the HDT is $U_{\text{HDT}}^0/k_B = 0.8$ mK.

3.1 mK, 6.0 mK, 9.4 mK, 13.0 mK and 16.8 mK, respectively, without further adjustment of T and w , finding good agreement with experimental data.

Using the quantitative definitions Eq. 4.15 and Eq. 4.16 we can determine the optimal width of the optical tweezers for our current experimental parameters, i. e., for the depth of the HDT of 0.8 mK and the atomic temperature of $T = 60 \mu\text{K}$. Using Eq. 4.15 we find the optimal depth of the VDT at $U_{\text{VDT}}^0/k_{\text{B}} = 0.51 \text{ mK}$. The corresponding width of the optical tweezers is calculated with Eq. 4.16 to be $2y_{\text{T}}^{\text{min}} = 2 \cdot 11.7 \mu\text{m}$, see Tab. 4.1.

4.3.4 Effects not included into the theory

Blurring of the image

We calculate the function P_{HDT} by analyzing the ICCD images. The effect of the blur on the camera chip on the resulting profile of $P_{\text{HDT}}(y)$ can be estimated by convoluting the LSF of the imaging system, see Sec. 2.2.5, with the respective function $P_{\text{HDT}}(y)$. Numerical simulations show that for the data presented in Fig. 4.8 this effect is negligibly small. Therefore, blurring of the imaging system was not taken into account.

Fluctuations and drifts of the traps

Radial fluctuations and drifts of the VDT with respect to the HDT result in the fluctuation of the center of the extraction region. Since for the above described experiment we have added up many images, the obtained extraction region is effectively broadened. In Sec. 4.6 we have measured these drifts of the traps to be less than micrometer. Therefore, the broadening caused by this effect on the determination of P_{HDT} is negligibly small.

Heating of atoms

The increase of the depth of the potential well with a trapped atom due to the adiabatic switching on of the VDT results in adiabatic heating of the atom [29]. Due to the Gaussian radial profile of the VDT, this heating is maximum at the center of the VDT and drops down further away along the axis of the HDT. Since for hotter atoms the slope of P_{HDT} at y_{T} is “softer”, see Fig. 4.6, our theoretical model overestimates this slope. The systematically stronger slope of the theoretical curve with respect to the experimental data in Fig. 4.8 can thus be attributed to this effect. Nevertheless, this effect does not significantly change the value of y_{T} ($P_{\text{HDT}}(y_{\text{T}}) = 0.99$), for at this lateral position the depth of the VDT, see Eq. 4.8, is exponentially reduced, and therefore the heating effect is small.

4.3.5 Towards ultimate resolution

Ultimate resolution of the optical tweezers is realized, if a single potential well of the HDT is addressed only, i. e., if the width of the optical tweezers $2y_{\text{T}} < 2 \cdot 0.532 \mu\text{m}$. Here, we use our model in order to develop strategies for the reduction of the width of our optical tweezers. The width depends on the depth and waist of the VDT, of the HDT, and on the temperature of the atoms in the HDT. Variation of the depth of the traps can be straight

Table 4.1: Width of the tweezers $2y_T^{\min}$ for different parameters

	$\frac{U_{\text{HDT}}}{k_B}$ (mK)	$\frac{U_{\text{VDT}}}{k_B}$ (mK)	T (μK)	$\frac{w_{\text{HDT}}}{\lambda_{\text{VDT}}}$	$\frac{w_{\text{VDT}}}{\lambda_{\text{VDT}}}$	F_r	y_T^{\min} (μm)
current experiment							
1	0.8	0.51	60.0	19	9.8	0.015	11.7
stronger focusing of optical tweezers							
2	0.8	0.51	60.0	19	4.9	0.025	5.9
3	0.8	0.51	60.0	19	2.45	0.025	2.9
lower atom temperature							
4	0.8	0.017	1.0	19	4.9	0.48	2.9
5	0.8	0.0088	0.084	19	2.45	0.92	0.5

forwardly realized by changing the power of the respective laser (up to up to 20 W for the VDT laser and 1.2 W for each beam for the HDT laser). Changing the waist size of the traps is connected with the design of new lens systems, and lowering of the atomic temperature requires the implementation of e. g. the Raman sideband cooling technique [55].

In the following analysis we concentrate on the dominating influence of beam properties and atomic motion. We ignore further experimental effects not included in our model, see above, which become relevant for ultimate precision.

Universal extraction function

We rewrite, first, the extraction efficiency from Eq. 4.14 in terms of dimensionless parameters:

$$\frac{U(y)}{k_B T} = s_T \left(e^{-\frac{2y^2}{w_{\text{VDT}}^2}} - F_r \right), \quad (4.17)$$

where the normalized tweezers potential depth

$$s_T = \frac{U_{\text{VDT}}^0}{k_B T} \quad (4.18)$$

compares the tweezers trap depth with atomic temperature, and

$$F_r = \frac{1}{\pi\sqrt{e}} \frac{U_{\text{HDT}}^0}{U_{\text{VDT}}^0} \frac{\lambda_{\text{VDT}}}{w_{\text{HDT}}} \quad (4.19)$$

is a relative measure of forces exerted by the VDT ($\sim U_{\text{VDT}}^0/\lambda_{\text{VDT}}$) and the HDT ($\sim U_{\text{HDT}}^0/w_{\text{HDT}}$). Condition of the extraction Eq. 4.7 translates into

$$F_r < 1.$$

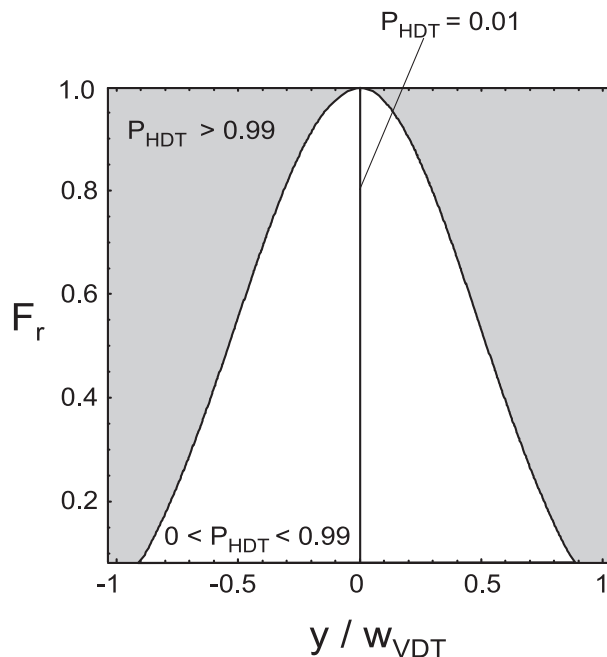


Figure 4.9: Contour plot for $P_{\text{HDT}}(y_{\text{T}}^{\text{min}}, F_{\text{r}}) = 0.99$. Outside the white area atoms will remain trapped in the HDT with at least 99 % probability.

The condition Eq. 4.15 that the target atom is extracted out of the HDT with 99 % efficiency, is satisfied for

$$s_{\text{T}} = \frac{8.4}{1 - F_{\text{r}}}. \quad (4.20)$$

Using this equation together with Eq. 4.16 we determine the connection between the minimal width of the optical tweezers $y_{\text{T}}^{\text{min}}$ and the dimensionless parameter F_{r} :

$$P_{\text{HDT}}(y_{\text{T}}^{\text{min}}, F_{\text{r}}) = 0.99, \quad (4.21)$$

which is plotted in Fig. 4.9.

From this figure we can already infer a strategy for improved resolution: the F_{r} value should be about unity, the waist of the VDT should be as small as possible. The increase of F_{r} can be done by increasing the depth of the HDT, reducing w_{HDT} and the temperature T of the atoms, see Eq. 4.19 and Eq. 4.18.

Examples of optical tweezers

Table 4.1 we have collected potential parameters for the dipole traps for improved extraction resolution. The traps and tweezers width in the first line corresponds to our current setup. In lines 2-3 we project parameters for improved resolution by changing the focusing properties of the VDT (2 and 4 times tighter, respectively) without modification of the HDT. In lines 4 and 5 the additional influence of reduced atomic temperatures is shown

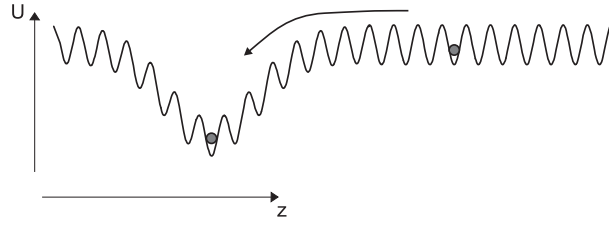


Figure 4.10: Axial insertion. An atom trapped in one of the potential wells of the standing wave of the VDT, is inserted into the Gaussian potential well of the HDT by axially moving the VDT along the z -direction.

($1 \mu\text{K}$ and ca. $0.1 \mu\text{K}$ which can be obtained with Raman cooling [56] and quantum degenerate gases). The last two lines show that by stronger focusing of the HDT the ultimate resolution can be reached without additionally cooling the atoms.

4.4 Insertion of an atom

After extraction, an atom is trapped in the potential of the VDT. In order to re-insert the atom into a potential well of the HDT, the VDT potential is merged with the HDT and finally switched off. There are two alternative methods to insert an atom back into the HDT: “axial insertion” and “radial insertion”. Some properties of these two methods, e. g., insertion precision, is the same for both methods. Whereas the difference becomes apparent, when we try to insert an atom with the VDT into the HDT, which holds another atom and the final interatomic separation is smaller than the size of the optical tweezers, which will be discussed in Sec. 4.5.

Axial insertion

In this case, the process of extraction of an atom is simply reversed: the VDT axially transports the atom to the axis of the HDT, see Fig. 4.10, and then the VDT is adiabatically switched off, leaving the atom in the HDT. The whole process of axial insertion takes about 70 ms.

Radial insertion

For radial insertion, the two traps are first radially separated by displacing the axis of the HDT in the positive x -direction, see Fig. 4.11a. Then the atom in the VDT is transported downwards to the vertical position of the horizontal trap, see Fig. 4.11b. Along the x -axis, the atom in this configuration is confined in the Gaussian-shaped radial potential of the VDT. In the next step, the VDT is then merged with the Gaussian-shaped radial potential of the HDT by moving the HDT radially towards the x -position of the VDT, see Fig. 4.11c. In the final step the VDT is adiabatically switched off, which releases the atom to the HDT, see Fig. 4.11d. The process of radial re-insertion takes about 210 ms.

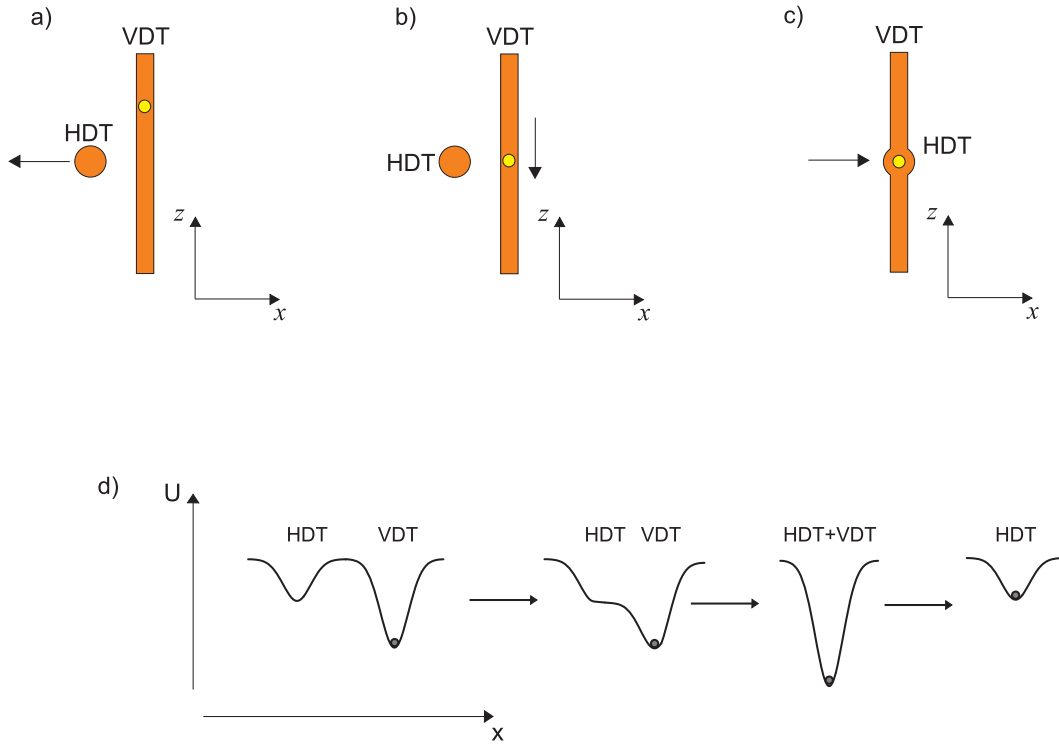


Figure 4.11: Radial insertion of an atom. a) An atom in the VDT after the extraction. The traps are separated by moving the HDT along the x -direction. b) The atom in the VDT is transported to the z -position of the HDT. c) The traps are merged by moving the HDT along the x -direction towards the VDT. d) Evolution of radial potentials of the traps along the x -axis for steps b) and c).

The ultimate goal of insertion is to securely drop an atom into a given HDT micropotential, for instance spaced exactly a given number of wells from its neighbor, but without influencing the neighboring atom.

4.4.1 Insertion precision

There are two independent effects influencing the precision of the insertion, i. e., how accurately an atom can be placed into a desired HDT micropotential: the atomic thermal motion in the transversal potential of the VDT and the fluctuations of the center of the optical tweezers relative to the HDT.

Transversal distribution in the VDT

Before contact with the HDT atoms trapped in the VDT are modeled as an ensemble in thermal equilibrium at a temperature T . For atomic temperatures much smaller than the depth of the VDT, the atoms can be considered to be trapped in a three-dimensional harmonic potential with the oscillation frequencies given by Eq. C.3 and Eq. C.7. In the

harmonic approximation all three degrees of freedom are decoupled, and the energy of each one-dimensional motion is Boltzmann-distributed with the same temperature T :

$$f_1(\varepsilon, T) = \frac{1}{k_B T} e^{-\varepsilon/k_B T}. \quad (4.22)$$

For a fixed energy ε , the probability to find an atom at position y in a potential $U(y) = m\Omega^2 y^2/2$ is

$$p_\varepsilon(y) = \frac{1}{\pi \sqrt{y_0^2 - y^2}}, \quad (4.23)$$

for $|y| \leq y_0$. Here $y_0 = \sqrt{\frac{2\varepsilon}{m\Omega^2}}$ is the turning point, and $\Omega = \Omega_{\text{rad}}$ is the radial oscillation frequency of the VDT. Integration of $p_\varepsilon(y)$ over all energies ε weighted with the Boltzmann factor gives the spatial distribution of a thermal atom:

$$\begin{aligned} p_T(y) &= \int_0^\infty p_\varepsilon(y) f_1(\varepsilon, T) d\varepsilon \\ &= \sqrt{\frac{m\Omega^2}{2\pi k_B T}} e^{-m\Omega^2 y^2/(2k_B T)}, \end{aligned} \quad (4.24)$$

which is a Gaussian distribution with the width

$$\delta y_{\text{therm}} = \frac{w_{\text{VDT}}}{2} \sqrt{\frac{k_B T}{U_{\text{VDT}}^0}}. \quad (4.25)$$

This width can also be expressed in terms of the VDT waist radius and the s_T -parameter, combining the tweezers trap depth and the temperature, see Eq. 4.18:

$$\delta y_{\text{therm}} = \frac{w_{\text{VDT}}}{2s_T^{1/2}}. \quad (4.26)$$

Spatial fluctuations of the tweezers axis

For insertion, the atoms must be inserted into the HDT at some target position. Since the VDT and the HDT laser beams are guided by independent mechanical setups, their relative position is subject to radial and axial fluctuations. In our model these fluctuations are taken into account by δy_{fluct} representing the rms-amplitude of the fluctuations of the VDT axis in the HDT frame of reference.

For our typical experimental parameters, the width of the thermal distribution is on the order of $0.5 \mu\text{m}$, and the rms amplitude of the axis fluctuations is about $0.5 \mu\text{m}$. Assuming these fluctuations are Gaussian distributed, the rms-amplitude of the combined fluctuations is

$$\delta y_{\text{insert}} = \sqrt{\delta y_{\text{therm}}^2 + \delta y_{\text{fluct}}^2}. \quad (4.27)$$

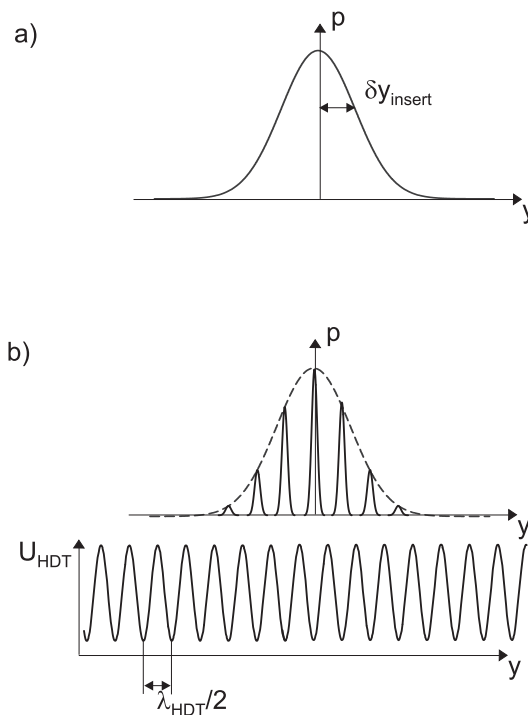


Figure 4.12: Spatial distribution $p(y)$ with the width y_{insert} is projected onto the standing wave of the HDT as both traps are merged (a). This distribution after the projection (b). The width of the envelope remains almost unchanged, but the probability is spatially modulated with the periodicity of the HDT.

The new Gaussian distribution of the probability of finding an atom along the HDT axis $p(y)$ has thus the width $\delta y_{\text{insert}} \approx 0.7 \mu\text{m}$, which is larger than the size of one HDT micropotential. Therefore, this distribution extends over several potential wells of the HDT, see Fig. 4.12a.

Insertion into HDT micropotentials by “projection”

For the last step of the insertion, the traps are merged and the VDT is finally switched off. Due to the periodicity of the HDT, the distribution $p(y)$ changes for $\delta y_{\text{insert}} \gtrsim \lambda_{\text{HDT}}/2$: its envelope reflects the width of the original distribution before the traps were merged, but under this envelope the distribution is now modulated with the periodicity of the standing wave of the HDT, see Fig. 4.12b. The distribution in each approximately harmonic micropotential is described again by a Gaussian of width

$$\delta y_{\text{micropot}} = \frac{\lambda_{\text{HDT}}}{2\sqrt{2\pi}} \sqrt{\frac{k_{\text{B}}T}{U_{\text{HDT}}^0}},$$

where T is the temperature.

It is clear that the insertion precision will be enhanced with improving localization of the atoms, i. e., with lower atomic temperature and deeper VDT potentials. Ultimately, for

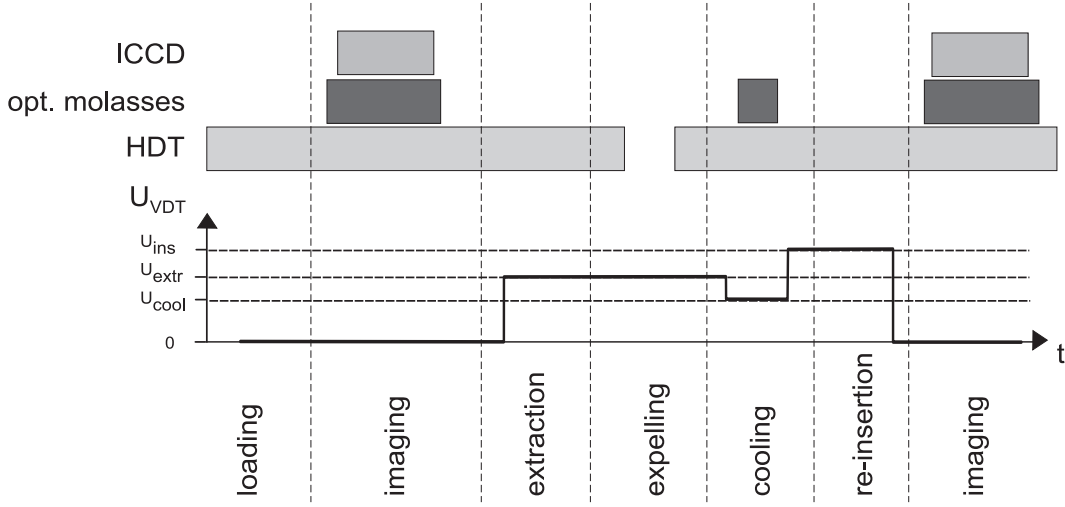


Figure 4.13: Experimental sequence for the characterization of the insertion precision. After loading on average one atom into the HDT it is imaged with the ICCD, which is followed by the extraction of the atom with the VDT. If there are more than one atom at the beginning of the sequence, the not extracted atoms are expelled by switching off the HDT for a short time. The extracted atom is then cooled and re-inserted into the HDT. The last image reveals the final position of the atom after the re-insertion.

$\delta y_{\text{insert}} \ll \lambda_{\text{HDT}}/2$ the final distribution will be concentrated into a single micropotential. This limit corresponds to “perfect” insertion of an atom into a single target micropotential. It is not yet realized in our experiment but will be discussed further.

4.4.2 Experimental studies of the insertion precision

We have carried out a series of measurements in order to experimentally study the dependence of the insertion precision on atomic temperature and on the depth of the VDT predicted by the model above. For this purpose we have loaded one atom on average into the HDT. This atom was then extracted with the VDT, cooled with optical molasses, and re-inserted back into the HDT, see Fig. 4.13. If there were initially several atoms loaded into the HDT, the rightmost atom was extracted, and the rest of the atoms was expelled out of the HDT by switching it off for 30 ms, while holding the extracted atom with the VDT. We have always cooled the atoms at the same conditions, i. e., at the same depth of the VDT and with the same parameters of the optical molasses. This has been realized by first lowering the depth of the VDT from the “extraction level” (U_{extr}) to the “cooling level” (U_{cool}) and by switching on the optical molasses for 100 ms. After the cooling, the depth of the VDT was ramped to the desired for the insertion value U_{ins} . The temperature was varied by performing the measurement with and without the cooling step in the experimental sequence.

We have calculated the standard deviation of the final positions of the atoms after several repetitions of the same experiment, yielding the insertion precision δy_{insert} . For $\delta y_{\text{insert}} \geq 0.5\lambda_{\text{HDT}}/2$ we can neglect the discretization of the positions due to the

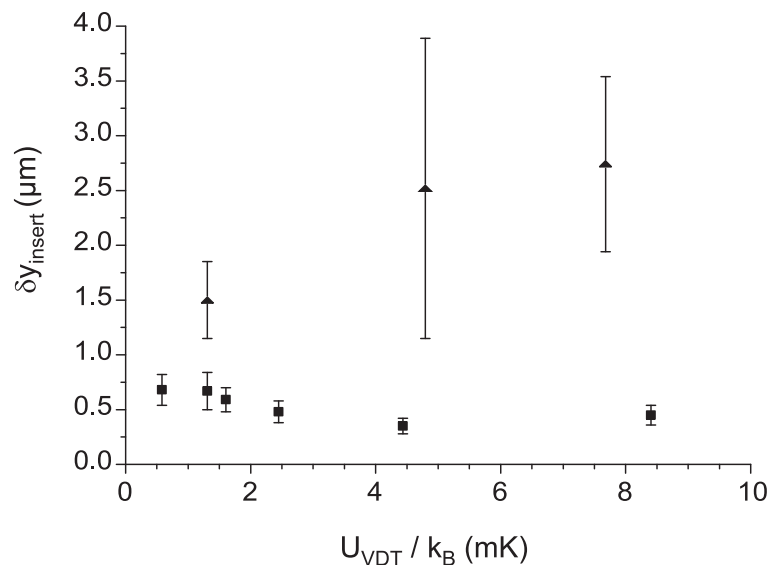


Figure 4.14: Insertion precision with and without cooling. The triangular points present the insertion precision for the experimental sequence without cooling of the atoms before re-insertion. The rectangular points are the results of the insertion precision with the cooling step. The depth of the HDT was fixed. In this experiment we have used the axial insertion method. Every point corresponds to about 25 repetitions of the experiment.

periodicity of the HDT [57].

4.4.3 Analysis

Figure 4.14 shows the result of the measurement for depths of the VDT between 0.6 mK and 8.4 mK, a fixed depth of the HDT ($U_{\text{HDT}}^0/k_B = 0.8$ mK), and with and without the cooling step.

Temperature of the atoms

Squares and triangles in Fig. 4.14 present the result of the measurement with and without cooling, respectively. The insertion precision in the case of the cooled atoms is on the order of 500–700 nm, whereas for the case without cooling it is several micrometers. This qualitatively demonstrates the temperature dependency of the insertion precision.

Depth of the VDT

In order to quantitatively analyze the dependence of the insertion precision on the depth of the VDT, the experimental data (squares in Fig. 4.14) were compared with the theoretical prediction given by the function Eq. 4.27 with y_{therm} from Eq. 4.25. For this purpose we

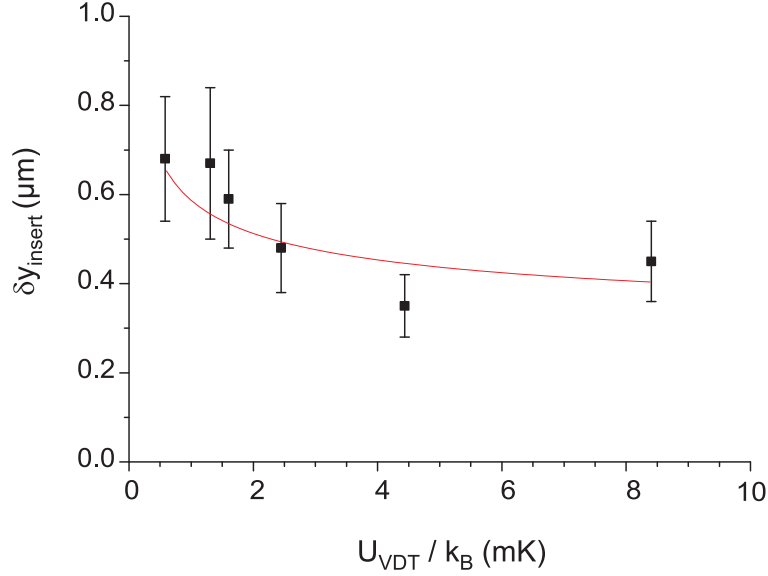


Figure 4.15: Insertion precision as the function of the depth of the VDT. The solid line is the fit of Eq. 4.28 to the experimental data (the rectangular points from Fig.4.14).

have rewritten this function as

$$\delta\delta y_{\text{exp}}(U_{\text{VDT}}) = \sqrt{\frac{b^2}{\sqrt{U_{\text{VDT}}}} + \overline{\delta y_{\text{fluct}}^2}}, \quad (4.28)$$

where we have also included the fact that atoms were cooled with the molasses at the VDT depth U_{cool} and then the depth of the VDT was ramped to the value, where the insertion took place (U_{VDT}). During this adiabatic ramping, the temperature of the atom adiabatically changes to the value of $T = T_0 \sqrt{U_{\text{VDT}}/U_{\text{cool}}}$ [29]. We have independently determined the contributions to $\overline{\delta y_{\text{fluct}}}$, i. e., the fluctuation of the VDT during this experiment (ca. 200 sec). The drifts of the VDT were measured by observing an atom in the VDT to be $\overline{\delta y_{\text{fluct}}} = 0.26(\pm 0.03) \mu\text{m}$. Equation Eq. 4.28 was then fitted to the experimental data with the fit parameter b . The parameter $b = \frac{w_{\text{VDT}}}{2} \frac{\sqrt{T_0}}{\sqrt[4]{U_{\text{cool}}}}$ yields the combination of the waist of the VDT, of the trap depth where the atom was cooled and the temperature. The result of the fit is presented in Fig. 4.15 with

$$b = 0.52(\pm 0.05) \mu\text{m mK}^{1/4}. \quad (4.29)$$

For $w_{\text{VDT}} = 10.1(\pm 1.4) \mu\text{m}$ and $U_{\text{cool}}/k_B = 1.6(\pm 0.3) \text{mK}$ we calculate the corresponding temperature of the atom in the VDT after the cooling with the optical molasses to be

$$T_0 = 13(\pm 4) \mu\text{K}.$$

This temperature is smaller than the temperature of the atoms in the HDT cooled with the optical molasses ($60 \mu\text{K}$). The difference between these values can be attributed to

the fact that the cooling process in the HDT is impaired by the multi mode nature of our HDT laser [24].

Periodicity of the HDT

A reconstruction of the periodically modulated probability distribution $p(y)$ of finding an atom along the HDT axis, as it is shown in Fig. 4.12b, requires accumulation of many images of individual atoms. Since the axial fluctuation of the HDT δy_{HDT} during the time of the experiment is on the order of the periodicity of the HDT, the measured positions of atoms do not show any periodic bunching. However in an experiment, where we have prepared a pair of atoms with a fixed separation, see Sec. 4.6, the distribution of the separations between the atoms show this periodic structure, see Fig. 4.21. Since the separations were measured relative to other atoms in the HDT and not relative to the ICCD camera, the axial fluctuations of the HDT were effectively suppressed, which allowed direct mapping of the periodically modulated probability distribution $p(y)$.

4.5 Insertion in the presence of other atoms

A radical difference of the two alternative insertion methods mentioned in Sec.4.4 occurs if the HDT already holds an atom within the width of the optical tweezers. Since during axial insertion the VDT exercises the same manipulations as during the extraction of an atom, this method limits the minimal final distance between the atoms in the HDT to the width of the optical tweezers, because otherwise the atom in the HDT will be extracted downwards by the VDT during the re-insertion, see Fig. 4.16a-b. In contrast, if the two traps are merged radially, the VDT does not exert any forces pushing an atom out of the HDT, see Fig. 4.16c-d. Consequently, for radial insertion there are no limitations on the final allowed distance. In particular, the final distance between two atoms can be zero. In this case, the two atoms will be joined in a single micro-potential of the standing wave of the HDT. The advantages of radial insertion are accompanied by a drawback due to the occurrence of an additional heating mechanism.

4.5.1 Insertion induced heating: Adiabatic model

Consider an atom trapped in the HDT at the y -position of the VDT, when the traps are axially separated along the x -direction. Along this direction the radial potentials of the two traps with the respective depths U_{HDT}^0 and U_{VDT}^0 have Gaussian shape each. For $k_{\text{B}}T \ll U_{\text{HDT}}^0$, the atom is trapped near the bottom of the potential well of the HDT. This trap is then moved along the x -direction towards the vertical trap just before the traps are merged, see Fig. 4.17. The atom has a potential energy of approximately $E_{\text{a}} \approx U_{\text{VDT}}^0 - U_{\text{HDT}}^0$, with respect to the bottom of the potential well of the VDT.

After the merger, the atom with energy E_{a} is trapped in the sum potential of the two traps. Adiabatically switching off of the VDT causes the atom to be adiabatically cooled

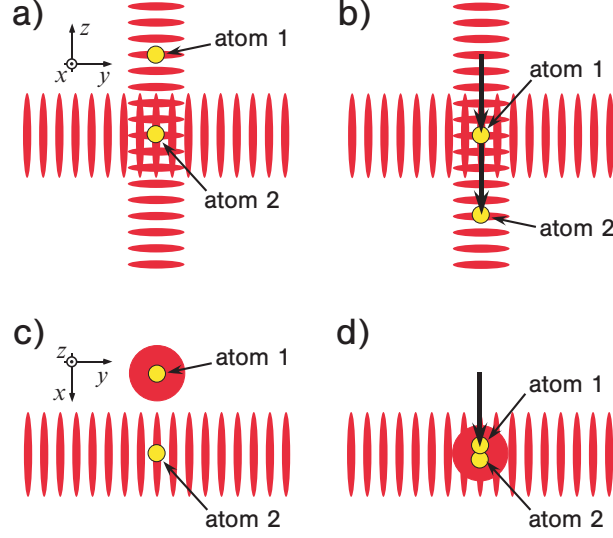


Figure 4.16: Insertion of an atom with the VDT into the HDT, which holds another atom, if the y -separation between atoms is smaller than the width of the optical tweezers. a)–b) During the axial insertion, atom 2 will be extracted downwards with the VDT out of the horizontal trap. c)–d) If the two traps are merged radially, both atoms will remain trapped in the HDT.

to the final atomic energy [29]:

$$E_a^{\text{final}} = E_a \sqrt{\frac{U_{\text{HDT}}^0}{U_{\text{HDT}}^0 + U_{\text{VDT}}^0}}. \quad (4.30)$$

The condition for the atom to remain trapped in the HDT is $E_a^{\text{final}} < U_{\text{HDT}}^0$, yielding an upper limit for the depth of the VDT

$$U_{\text{VDT}}^0 < 3U_{\text{HDT}}^0, \quad (4.31)$$

otherwise the atom will be lost.

4.5.2 Measurement of the heating effect

In order to experimentally check the model, we have carried out the following experiment: One atom on average was loaded into the HDT. The atom was then transported to the y -position of the VDT axis. For the third step, the HDT with the atom was transported in the x -direction, and the VDT was switched on. At the fourth step, the atom was transported back towards the VDT as it would occur during the radial insertion. Thereafter the VDT was switched off adiabatically. The final image reveals the presence or the absence of the atom in the HDT after this manipulation. Figure 4.18a shows the survival probability of an atom in the HDT after this manipulation.

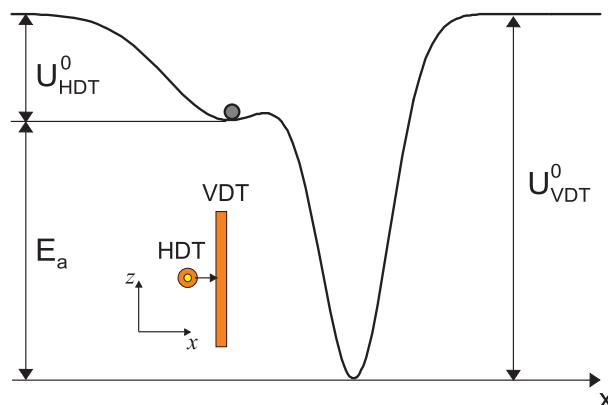


Figure 4.17: Radial potential of the two traps. During the radial merging of the traps, an atom in the radial potential of the HDT has a potential energy E_a , relative to the bottom of the potential well of the VDT. The inset shows the respective geometry of the traps.

4.5.3 Analysis

Experimental data in Fig. 4.18a show that starting from a VDT depth of 2.5 mK the atoms in the HDT were heated up and lost during the radial insertion procedure. Since the depth of the HDT for this experiment was 0.8 mK, the condition Eq. 4.31 results in $U_{\text{VDT}}^0 < 2.4$ mK, which reasonably agrees with the experimentally observed value. This result gives us the upper limit on the depth of the VDT.

At the same time, the lower limit on the depth of the VDT is dictated by the insertion precision, which deteriorates with the reduction of the VDT depth. Figure 4.18b shows the insertion precision, measured for the same depth of the HDT using the radial insertion method. For VDT depths below about 1.2 mK the insertion precision is dominated by the thermal component, see Eq. 4.25.

The non shaded regions in Fig. 4.18 give the range of the experimentally useful depths of the VDT. For our typical experimental parameters there is a non empty overlap of the experimentally useful ranges for the depth of the VDT. This region can be further enlarged by increasing the depth of the HDT, see Eq. 4.31.

4.5.4 Conclusion

Summarizing, both methods of insertion allow the same high precision on the order of the periodicity of the HDT. Although we have not yet reached the ultimate precision, i. e., secure insertion of an atom into a desired micropotential of the HDT, we have identified the main limiting factors: thermal motion of the atom in the VDT and radial fluctuations of the VDT-tweezers relative to the horizontal trap. The first factor can be reduced by increasing the spatial confinement of the atom in the VDT, i. e., by increasing the trap depth and reducing the atomic temperature. Active stabilization of the positions of the traps would result in the reduction of their fluctuations.

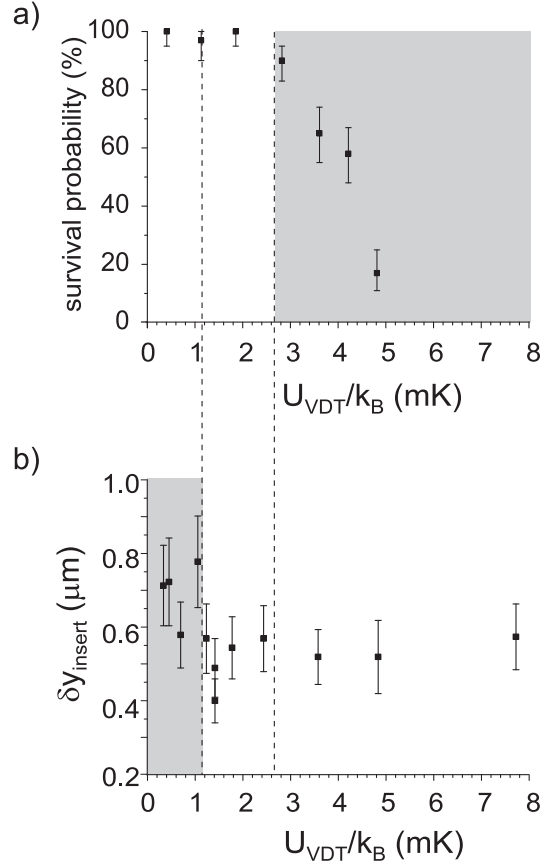


Figure 4.18: Optimal depth of the VDT. a) The survival probability of an atom in the HDT as a function of the depth of the VDT. Every point is the result of about 35 repetitions of the experiment. b) The insertion precision (radial insertion) as a function of the depth of the VDT. Every point corresponds to about 35 repetitions with a single atom. The shaded areas show the experimentally useless ranges of the depth of the VDT.

Moreover, working with several atoms in the HDT, the radial insertion method does not limit the final distance between the atoms after the re-insertion. It can be made even as small as zero. By suitably selecting the depths of the traps, e. g., 1.2 mK to 2.4 mK for the VDT and 0.8 mK for the HDT, this re-insertion can be done effectively and without loss of the atoms due to the insertion. On the other side, the axial insertion is intrinsically faster, which is important for working with strings with many atoms, see Sec. 4.7.

4.6 Distance control between two atoms

Now, the combination of the techniques to trap a string of atoms in the HDT (Sec. 3.2), determine the initial positions of the individual atoms (Sec.2.2.5), extract a selected atom (Sec. 4.3), and re-insert this atom at any target position in the string (Sec. 4.4) is used to realize an active control of the separation between two atoms. In this experiment we

prepare two atoms in the HDT with the target separation $d_t = 15 \mu\text{m}$.

4.6.1 Experimental realization

Repositioning procedure

At the beginning, two atoms on average were loaded into the HDT. The following experimental sequence was then executed irrespectively of the actual number of atoms. However, for the analysis of the experimental data we have post-selected the events with initially two atoms. The initial positions of the atoms along the HDT were determined from the first ICCD image, see Sec. 2.2.5. The HDT transported then the atoms along the y -axis so that the righthand atom stopped at the position of the VDT, see Fig. 4.19a. The VDT then extracted this atom out of the horizontal trap, see Fig. 4.19b. While holding this atom with the VDT, the remaining atom was transported along the y -direction so that it stopped at the nominal target distance $d_t = 15 \mu\text{m}$ to the right from the axis of the VDT, see Fig. 4.19c. The extracted atom was then cooled using the optical molasses during 100 ms and radially re-inserted into the HDT. For this purpose the traps were first separated by displacing the axis of the HDT along the x -direction, see Fig. 4.19d. Then, the atom in the VDT was transported downwards to the z -position of the HDT, see Fig. 4.19e. In the final step the extracted atom was inserted at the desired position by shifting the HDT radially to the x -position of the VDT and adiabatically switching off the VDT, see Fig. 4.19f. The second ICCD image was recorded to check the outcome of the manipulation sequence, see Fig. 4.19g.

In this algorithm, the two transportation distances with the HDT, s_1 and s_2 , have to be calculated from the initial positions of the atoms y_1 and y_2 , from the position of the VDT y_{VDT} and from the nominal final distance d_t .

Position of the VDT In order to reduce the influence of the radial drifts of the VDT, its position was measured once per 200 repetitions. This was realized by repeating the sequence, analogous to the one, used for the characterization of the insertion precision, see Fig. 4.13. In this sequence single atoms were inserted into the HDT with the optical tweezers. The mean value of the final position of the re-inserted atoms gave then the y -position of the VDT in pixels, y_{VDT} .

Transportation distances The rearrangement algorithm requires two transports along the HDT axis. They have to be calculated from position of the VDT y_{VDT} , the nominal target distance d_t and the initial positions y_1 and y_2 of the lefthand and of the righthand atoms, respectively. After the first transport, the atom 2 have to be at the position of the VDT. Therefore, the first transportation distance is

$$s_1 = -(y_{\text{VDT}} - y_2)\alpha,$$

where α is the pixel-to- μm calibration coefficient, see Sec. 4.2. After the second transport, the atom 1 have to be at the distance d_t to the right from the VDT. Therefore, the second transportation distance is

$$s_2 = (y_1 - y_2)\alpha + d_t.$$

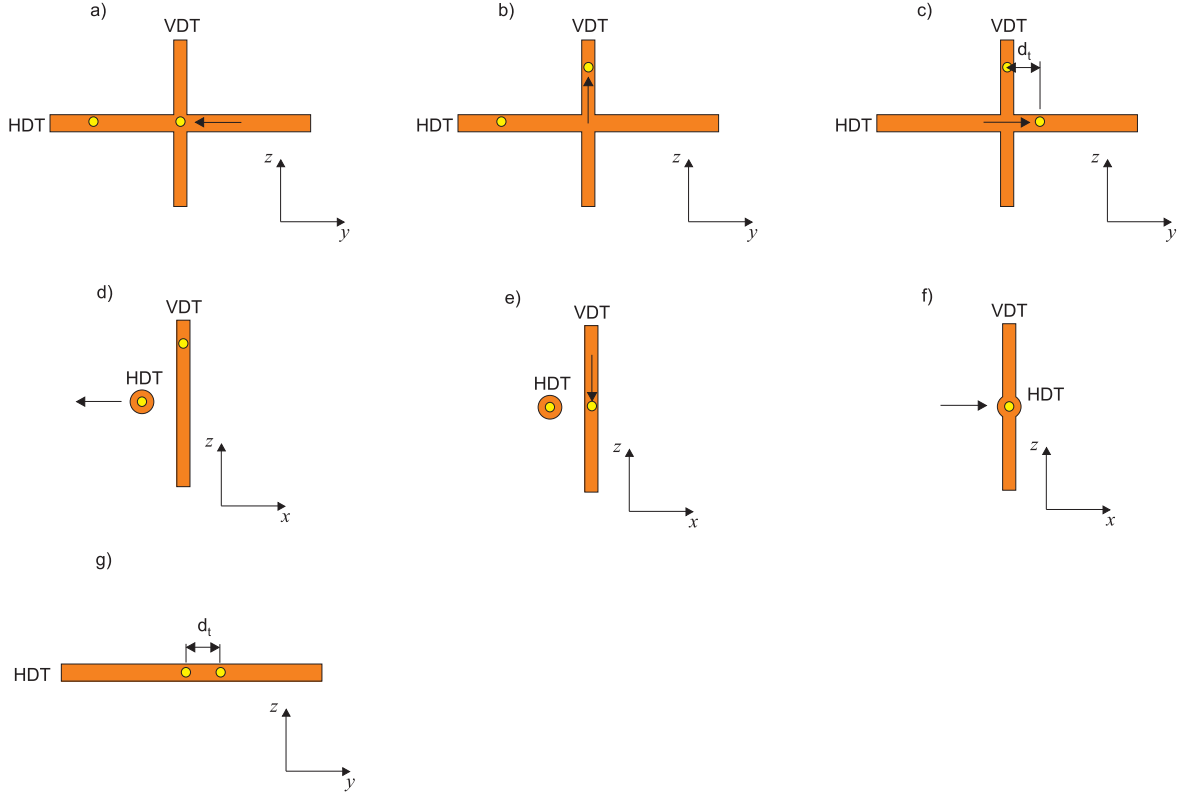


Figure 4.19: Steps of the distance control. a) The righthand atom is transported to the y -position of the VDT and the VDT is switched on. b) This atom is extracted upwards with the optical tweezers. c) The atom in the HDT is transported to the position d_t to the right from the VDT. d) The axes of the two dipole traps are separated. e) The atom in the VDT is transported downwards to the z -position of the HDT. f) The HDT is moved in the x -direction towards the VDT. g) After switching off the VDT, the pair of atoms in the HDT with the desired separation d_t is prepared. Note that the figures d-f are viewed along the y -direction, whereas the rest along the x -direction.

Experimental parameters

For this experiment we have used the HDT with the depth of $U_{\text{HDT}}^0 = 0.8$ mK using 1 W of the laser power in each arm of the standing wave. The VDT was used with 0.3 W in the incoming beam, which corresponds to the depth of $U_{\text{VDT}}^0 = 1.5$ mK. We have used the same depth of the VDT for the extraction, for cooling and for the re-insertion on the atoms.

During this experiment atoms have to be transported over different distances along the y -axis, depending on the initial position of the atoms. The transportation over different distances was then realized by varying the transportation time t_D :

$$d = a \frac{t_D^2}{4}, \quad (4.32)$$

keeping the acceleration of $a = 1000$ m/s constant. In this experiment we have transported

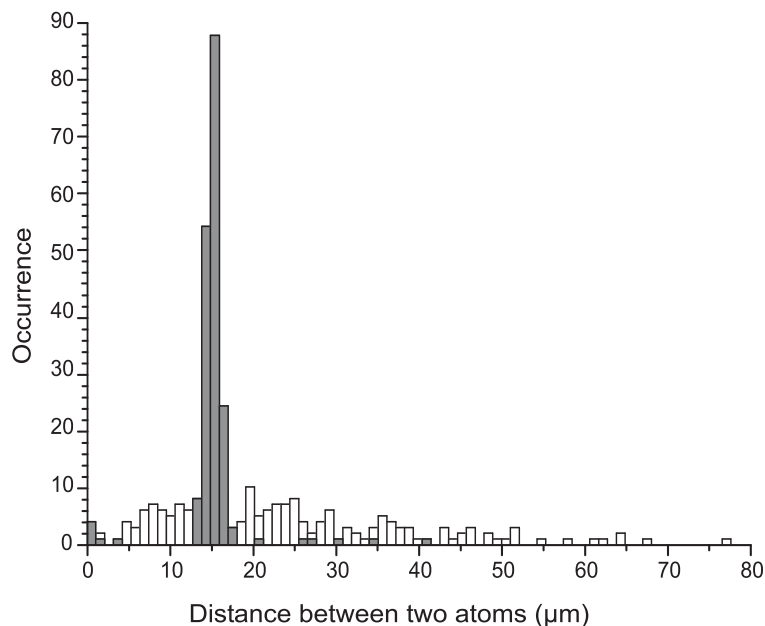


Figure 4.20: Actively controlling the distance between simultaneously trapped atoms in the HDT. The white histogram shows the broad distribution of the initial atomic separations for about 190 pairs. The grey histogram shows the final distribution of distances for the same pairs after the distance control operation (target distance $d_t = 15 \mu\text{m}$). It is narrowed down to a width of only $\delta d_m = 0.78 \mu\text{m}$ rms, centered around $d_m = 15.27 \mu\text{m}$.

over the distances of up to $100 \mu\text{m}$, which corresponds to the transportation times of up to $600 \mu\text{s}$.

The entire experimental sequence took about 5100 ms. This includes preparing of the atoms in the MOT and loading them into the HDT (200 ms), first exposure (1000 ms), readout of the image and its analysis (800 ms), reprogramming the DFD (840 ms), spatial manipulation of the atoms (460 ms), taking the second image (1000 ms) and its readout and analysis (800).

For this experiment we have used the calibration constant of $\alpha_{\text{trans}} = 0.499 \mu\text{m}/\text{pixel}$ determined in a separate calibration measurement using the transportation method. The Fourier analysis of the final experimental data showed that the calibration constant, corresponding to the current experiment, was $\alpha_{\text{Fourier}} = 0.4967 \mu\text{m}/\text{pixel}$, see Sec. 4.2. This constant was then used for the analysis of the experimental data.

4.6.2 Experimental results

During this experiment the experimental sequence was executed for about 1400 times. The events with only 2 atoms at the beginning were then post selected.

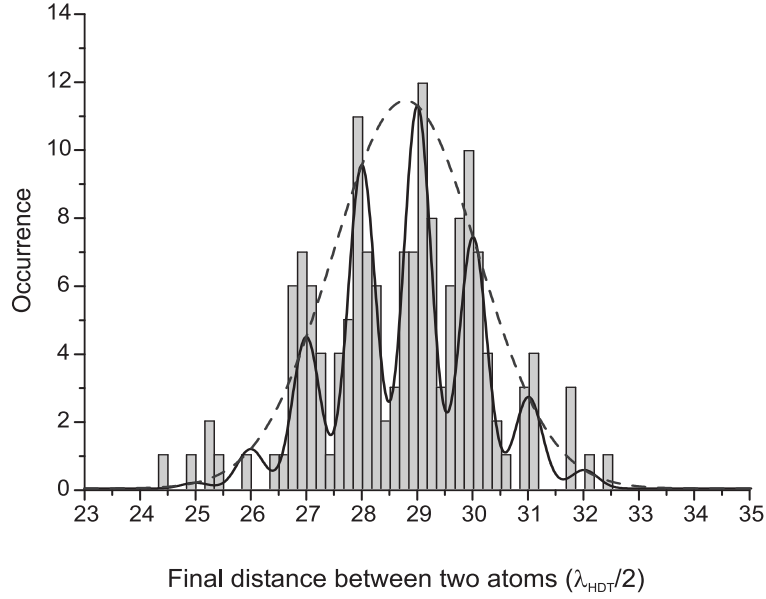


Figure 4.21: Zoom of the distribution of the final distances displayed in Fig. 4.20. The histogram clearly shows that the final distances are integer multiples of the standing wave period of $\lambda_{\text{HDT}}/2$ and that the final distribution extends over only 3-4 standing wave potential wells. The solid line is a theoretical fit with a Gaussian envelope (dashed line) centered at $d_{\text{Gauss}} = 15.31 \mu\text{m}$ and having a $1/\sqrt{e}$ -halfwidth of $\delta d_{\text{Gauss}} = 0.71 \mu\text{m}$. The narrow peaks under this envelope have a $1/\sqrt{e}$ -halfwidth of $\delta d_{\text{Gauss}} = 0.130 \mu\text{m}$, corresponding to the precision of our distance measurement.

Final and initial distances

Figure 4.20 shows a histogram (bin size $\lambda_{\text{HDT}} = 1064 \text{ nm}$) of the initial distances (white) and final distances (grey) between the atoms for about 190 pairs. Initially, atoms have random distances up to about $80 \mu\text{m}$. In contrast, the final distribution is strongly peaked with the mean value of

$$d_{\text{m}} = 15.27(\pm 0.06) \mu\text{m}$$

and a standard deviation of

$$\delta d_{\text{m}} = 0.78(\pm 0.05) \mu\text{m}.$$

The $1/\sqrt{e}$ -width of the distribution thus extends over only few potential wells of the HDT.

Discretization of the final distances

This spread of the final distances over only a few potential wells is strikingly apparent in Fig. 4.21, where the histogram of the distribution of the final distances is displayed for a smaller bin size of $\lambda_{\text{HDT}}/12 = 89 \text{ nm}$. The distribution is clearly peaked with a 532 nm , indicating that the final distances are integer multiples of the standing wave period $\lambda_{\text{HDT}}/2$ [22].

To demonstrate this fact quantitatively, the experimental data were fitted with the sum of eight Gaussian functions, keeping the distance between the peaks constant and the height of each of them lying on the envelope of another Gaussian function:

$$f(d) = \sum_{i=1}^8 a \exp\left(-\frac{((d_f + i) - d_{\text{Gauss}})^2}{2(\delta d_{\text{Gauss}})^2}\right) \exp\left(-\frac{(d - (d_f + i))^2}{2w_p^2}\right). \quad (4.33)$$

As the fit parameters were taken: the center of the envelope d_{Gauss} , the $1/\sqrt{e}$ -halfwidth of the envelope δd_{Gauss} , the $1/\sqrt{e}$ -halfwidth of the individual peak w_p and the center of the first peak d_f . The individual peaks reflect our ability to determine the distances between individual atoms with a sub-micrometer precision. Whereas the envelope reflects the accuracy of the distance control procedure.

The envelope is centered at

$$d_{\text{Gauss}} = 15.31(\pm 0.07) \mu\text{m}$$

and having a halfwidth of

$$\delta d_{\text{Gauss}} = 0.71(\pm 0.05) \mu\text{m}.$$

These values are in a good agreement with the corresponding values d_m and δd_m determined from the statistical analysis of the data, see above. The position of the first small peak is at

$$d_f = 24.00(\pm 0.03) \lambda_{\text{HDT}}/2,$$

demonstrating that the small peaks are situated exactly at the positions of the potential minima of the HDT. Whereas the halfwidth of each small peak is

$$w_p = 0.130(\pm 0.010) \mu\text{m},$$

corresponds to the precision of the distance measurement. In a previous experiment we have determined the precision of the distance measurement using only one ICCD image is $0.135(\pm 0.030) \mu\text{m}$ [22].

This result is a direct evidence for the ability to control the distance between two simultaneously trapped atoms on the scale of the wells of the standing wave potential.

Efficiency

As was already noted in the Sec. 4.3, in order to selectively extract an atom out of the HDT, its separation from the other atoms in the string should be larger than the size of the optical tweezers. This can be seen in Fig.4.22, where the final distances between the atoms are plotted as the function of the initial distances. This demonstrates that the distance control method reliably works for initial distance greater than $10 \mu\text{m}$. Whereas if the atoms are initially too close to one another and one tries to extract one of them, the action of the VDT on the second atom will be non-negligible and will lead to uncontrolled effect, e.g. extraction, ejection, etc. Therefore, for the calculation of the efficiency of

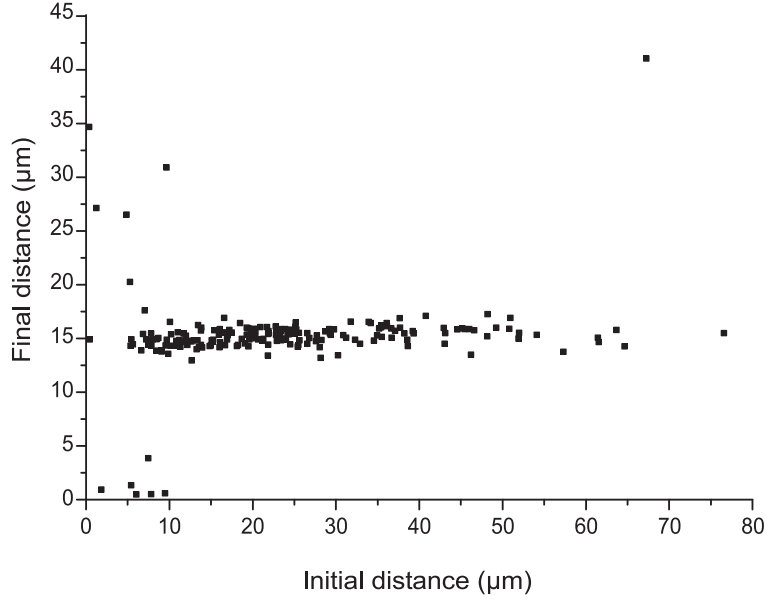


Figure 4.22: Correlation between the final and the initial distance measurement.

the distance control operation was done after post selecting the events with the initial interatomic separations of more than $10 \mu\text{m}$. We define the efficiency of the distance control operation as the ratio of the number of successful events with two atoms trapped at the desired distance after the operation to the number of all events where two atoms were initially present in the HDT and separated by more than $10 \mu\text{m}$.

In this experiment the extracted efficiency was about 80 %. We have determined that it was mainly limited by the intensity fluctuations of our laser of the VDT caused by the back-coupling of the retro reflected beam to the resonator of the laser. These fluctuations caused then parametric heating of the atoms in the VDT, thereby increasing their loss rate. After installing the second optical isolator at the output of the Yb:YAG laser of the VDT, see Fig. 2.8b, this back-coupling was reduced. Therefore, an independent measurement analogous to the previous one, but with less shots, was carried out to determine the improved efficiency. In this case, the efficiency of the distance control operation was

$$p_{\text{DC}} = 98_{-5}^{+2} \text{ \%}.$$

This value is compatible with the assumption that the distance control operation does not introduce any significant losses and that atom loss solely occurs due to background gas collisions, see Sec. 2.2.5, during the 2.1 s duration of the distance control operation. This time was counted from the moment of the end of the first exposure till the beginning of the second exposure.

4.6.3 Analysis

Deviation of the final distance from the target distance

Analysis of the data of the distance control experiment shows, that the deviation of the experimentally measured average final distance between the atoms of $d_m = 15.3 \mu\text{m}$ from the target distance $d_t = 15.0 \mu\text{m}$ stems from the drifts of the VDT during the experiment. Although the influence of the global drift of the VDT during the whole experiment was reduced by re-calibrating the position of the VDT after every experimental run (ca. 200 shots, which takes about 15 min.), the drifts during one experimental run resulted in the average shift of the final distance by ca. $0.3 \mu\text{m}$ from the nominal distance. Nevertheless, numerical simulations show, that the corresponding increase of the spread of the final distances in this experiment due to this effect is less than 10 nm rms.

Spread of the final distances

The spread of the final distances of $\delta d_m = 0.78 \mu\text{m}$ mainly arises from the two factors: the precision of the transport of the atoms along the axis of the HDT and the precision of re-insertion of the extracted atom into the HDT.

Precision of the transport. In our previous work [22], it has been shown that the precision of the transport of an atom to a predetermined position along the HDT in our experiment is subject to a statistical error $\delta y_{\text{transp}} = 0.190(\pm 0.025) \mu\text{m}$ rms. Since the experimental sequence used here involves two transports along the HDT, i.e., moving the atom to be extracted to the y -position of the VDT and then placing the remaining atom at the target distance d_T from y_{VDT} , this effect contributes an uncertainty of $\sqrt{2}\delta y_{\text{transp}} = 0.270(\pm 0.035) \mu\text{m}$ to the final distance between two atoms.

Insertion precision. Immediately after the reinserting the extracted atom into the HDT, its measured position has a spread of $\delta y_{\text{insert}} = 0.65(\pm 0.05) \mu\text{m}$ rms, which directly contributes to the spread of measured final distances. This value was extracted from the final positions of the atoms being re-inserted during the same experiment.

The insertion precision itself has contributions from the finite confinement of the extracted atoms in the VDT due to their thermal motion, from the fluctuations and drifts of the VDT and from the precision of the position determination of the atom.

The contribution from the thermal motion of the atoms in the VDT can be estimated using Eq. 4.25 and Eq. 4.29 to $0.47(\pm 0.06) \mu\text{m}$ rms along the y -direction. Long time fluctuations and drifts of the VDT along the y -direction during the whole experiment have been measured to be $0.5(\pm 0.2) \mu\text{m}$ rms, by observing the y -position of atoms trapped in the VDT with the ICCD camera.

The quadratic sum of these two errors together with the precision of the position determination of the atom itself ($0.143(\pm 0.020) \text{ nm}$ rms [22]) yields $\delta y_{\text{insert}}^{\text{th}} = 0.7(\pm 0.2) \mu\text{m}$ rms, which is in a good agreement with the measured $\delta y_{\text{insert}} = 0.65(\pm 0.05) \mu\text{m}$ rms.

Using these values we can estimate the expected spread of the final distances as

$$\Delta d_{\text{th}} = \sqrt{2\delta d_{\text{transp}}^2 + \delta y_{\text{insert}}^2 + w_{\text{p}}^2} = 0.72(\pm 0.05) \mu\text{m rms},$$

where $w_{\text{p}} = 0.130(\pm 0.010)$ is the precision of our distance measurement. This spread is in a good agreement with the measured $\delta d_{\text{m}} = 0.78(\pm 0.05) \mu\text{m rms}$ and $\delta d_{\text{Gauss}} = 0.71(\pm 0.05) \mu\text{m}$ extracted from the fit. This demonstrates the correctness of the assumption that there are no other significant contributions to the spread of the final distances, and, correspondingly, to the precision of the distance control method.

4.6.4 Conclusion

Summarizing, we have demonstrated that the distance between two simultaneously trapped atoms can be actively controlled with a precision of $0.78(\pm 0.05) \mu\text{m rms}$. This precision is of the same order of magnitude as the separation between the adjacent walls of the standing wave dipole trap. The success rate of this process is $98_{-5}^{+2} \%$, provided that the initial separation exceeds $10 \mu\text{m}$.

The precision of the distance control operation on the level of the potential wells of the HDT suggests the possibility of controllably joining of two atoms in a single well of the HDT. Whereas the high efficiency of this operation allows to scale up the number of the atoms to be rearranged, e. g., building an equidistant string of several atoms.

4.7 Building an equidistant string of several atoms

The distance control method, see Sec. 4.6, can be easily extended for string with a larger number of atoms. We have demonstrated this by creating equidistant strings of up to seven neutral atoms.

4.7.1 Experimental realization

Starting with larger strings of $n \geq 3$ atoms in the HDT, a sequential application of the distance control operation allows to rearrange the string. For this purpose exactly n atoms were first loaded into the HDT, see Ch. 3. Then, the positions of all n atoms are determined from the first fluorescence image. After this the rightmost atom is extracted and inserted at the target distance d_{t} to the left of the leftmost atom. The only difference in the spatial manipulation to the distance control experiment is that the manipulation steps c and d in Fig. 4.19 were interchanged. After each distance control operation the order of the atoms within the string undergoes a cyclic permutation. Since for each step the same target distance was used, after $n - 1$ such steps all atoms within the string are equidistantly spaced with respect to each other. The final fluorescence image is recorded in order to check the outcome of the whole manipulation.

We have used the same experimental parameters, i. e., depths of the traps, exposure time and the pixel to micrometer calibration as for the distance control experiment above.

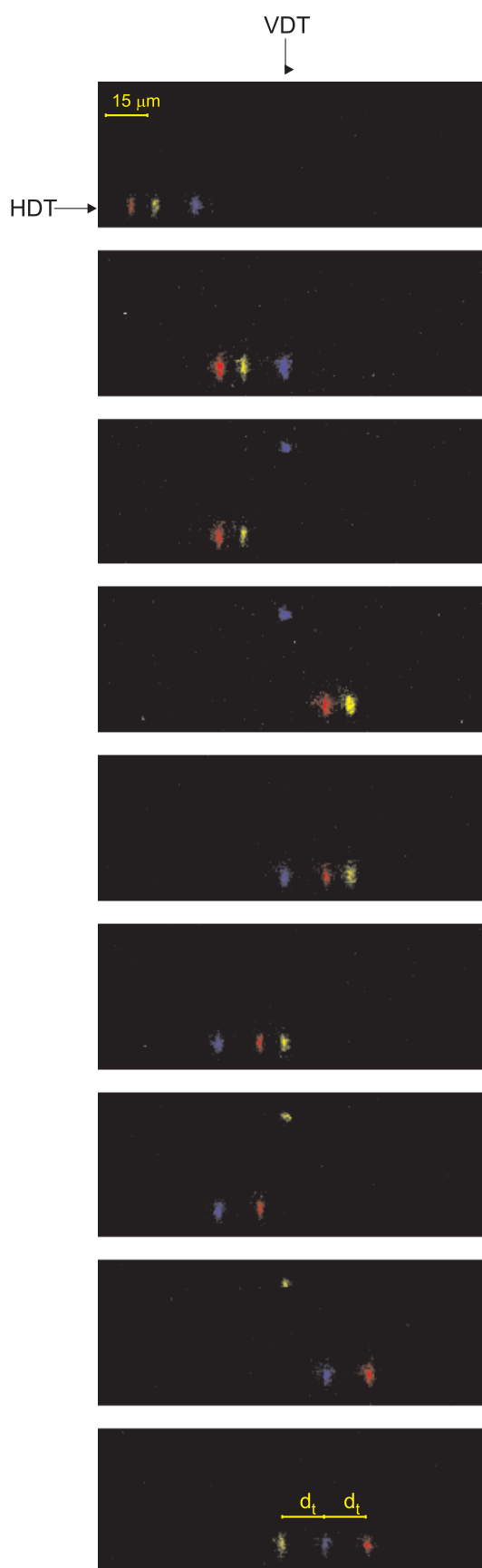


Figure 4.23: Sequence of the ICCD images of the step-by-step rearrangement of a string of three atoms. Two out of three atoms are cyclically rearranged by a sequential application of the distance control operation.

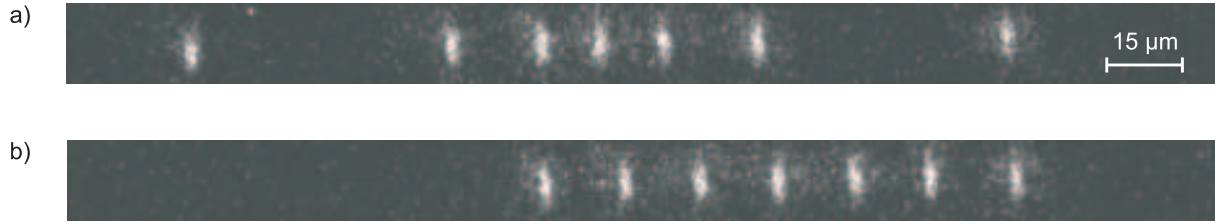


Figure 4.24: Building a regular string of seven neutral atoms. a) Initial string with randomly separated atoms. b) The same string after rearranging six out of the seven atoms with our distance control operation.

The only difference lays in the timing of the sequence. This is based on the fact that the DFD generator can be programmed with only 8 transportation distances, see Sec. 4.1, which is enough for rearrangement of up to 4 atoms. In order to manipulate more than 4 atoms, an additional reprogramming of the DFD should be done after the eighth transport with the HDT. The reprogramming then takes additionally 840 ms.

4.7.2 Experimental results

We have recorded a detailed sequence of ICCD images, illustrating the steps of the rearrangement of a string of *three* atoms, see Fig. 4.23. Here, after each step of the manipulation an ICCD image with 1 s exposure was made. Since the target final separation between the atoms was set to $d_t = 15 \mu\text{m}$, this operation results in the creation of a string of three equidistantly separated atoms.

Figure 4.24 shows ICCD images of a string of *seven* atoms that has successfully been rearranged. After extracting and re-inserting six out of the seven atoms, the initially random separations have clearly been made equidistant with the interatomic spacing of $15 \mu\text{m}$.

4.7.3 Analysis

We now estimate the scalability of our distance control method to even larger strings of atoms, i. e., of how many atoms we can successfully rearrange without losing none of them if the initial separations between the atoms are more than the size of the optical tweezers. For this purpose we use the assumption that the atom losses are caused only by background gas collisions, see Sec. 4.6.2, with the time constant $\tau \approx 60 \text{ s}$ from Sec. 2.2.5. In this case, the probability to have all n atoms successfully rearranged is

$$p(n) = \left(e^{-\frac{T(n)}{\tau}} \right)^n,$$

where $T(n)$ is the manipulation time, i. e., between the end of the first exposure and before the start of the second exposure with the ICCD camera.

According to this equation, the efficiency of the creation of a string with seven atoms is about 50 %. The increase of the number of atoms in the string, but keeping this efficiency at the same level, can be done by reducing the manipulation time. Since, the axial insertion

method requires less atom manipulation steps, this method is thereby intrinsically faster. Using the axial instead of the radial insertion would allow us to manipulate nine atoms. Further improvements of the setup such as usage of shorter cooling in the VDT, movement of the VDT standing wave with AOMs and driving the AOMs with a frequency synthesizer, which can be faster reprogrammed, would increase this number to about 14 atoms for the radial and to about 21 atoms for the axial insertion method.

It should be noted that these results are only rough estimations of the order of magnitude and strongly depend on the quality of the vacuum in our experimental setup.

4.7.4 Conclusion

Summarizing, we can prepare equidistant strings of up to seven atoms in a standing wave dipole trap by rearranging atom-by-atom irregular strings, supplied by loading the trap with an exactly known number of atoms from a magneto-optical trap.

4.8 Joining two atoms in one well of the standing wave

4.8.1 Experimental realization

According to our model of the radial insertion process, see Sec.4.4, it should be compatible with the target distance zero. In this section we experimentally demonstrate that two atoms can be joined in one potential well of the HDT.

Repositioning procedure

For this purpose, exactly two atoms were first loaded into the HDT, see Ch. 3. Then, the distance control operation with the target distance $d_t = 0 \mu\text{m}$ was applied to the atoms, see Sec. 4.6. The difference in the manipulation in comparison to the distance control experiment is that the manipulation steps c and d in Fig. 4.19 were interchanged in order to make this scheme be compatible with the target distance zero. This modification allows us to separate the two atoms in two dipole traps.

Experimental parameters

For this experiment we have used the HDT with the depth of $U_{\text{HDT}}^0 = 1.0 \text{ mK}$ using 1.3 W of the laser power in each arm of the standing wave. The VDT was used with 0.3 W in the incoming beam, which corresponds to the depth of $U_{\text{VDT}}^0 = 1.5 \text{ mK}$. The calibration between the pixels and the micrometers and the timing of the experimental sequence was chosen to be the same as in the distance control experiment.

Although, the experimental problem of joining two atoms in one potential well of the standing wave was experimentally solved using our radial insertion method, see Sec. 4.4, the detection of the success of joining cannot be solved by purely optically methods. The resolution of our imaging system is $\sigma_{\text{total}} = 0.9 \mu\text{m}$, see Sec. 2.2.5, corresponding to 1.7 potential wells. Whereas in this experiment, we have to discriminate the case where the

two atoms have successfully been transferred into the same potential well from the case where the two atoms occupy neighboring potential wells of the standing wave.

4.8.2 Detection scheme

We discriminate these cases by inducing two-atom losses which take place if and only if the two atoms are trapped in the same potential well, see Sec. 3.3.1. This is achieved by illuminating the atoms with the optical molasses for 1 s after merging the traps.

It has been shown that radiative escape is the leading physical mechanism for light induced collisions in a dipole trap illuminated by an optical molasses [58]. For this process, the released kinetic energy causes both atoms to reliably leave the trap. If, on the other hand, the atoms reside in different potential wells, radiative escape is not possible and the atoms remain trapped. Detecting the absence of the pair of atoms after the optical molasses stage therefore confirms the successful joining of the two atoms in one potential well of the HDT.

In order to determine the time scale of this process, and thereby to determine the necessary illumination time we have performed the following experiment: We loaded a variable number of atoms from MOT the into the HDT, illuminated them with the optical molasses, and detected the atomic fluorescence with the APD. The level of this fluorescence signal is a direct measure of the number of trapped atoms, so that the dynamics of the atom losses from the trap is immediately revealed from the time-dependence of their fluorescence. If we have loaded a small number of atoms into the HDT, e.g., on average 3 atoms per shot distributed over on average 25 potential wells, their fluorescence level remained constant, see open circles in Fig. 4.25. For a large number of atoms, e.g., on average 19 atoms per shot distributed over on average 25 potential wells, however, we observed an exponential decay of the average fluorescence level to a steady state value within about 150 ms, see filled circles in Fig. 4.25.

This behavior can be interpreted as follows: for about 3 atoms per 25 potential wells, the probability for having two atoms in one potential well, and thus for inducing cold collisions between them, is negligibly small. In this case, no atom losses are detected when illuminating them with the molasses. For about 19 atoms per 25 potential wells, however, the probability for at least two atoms to occupy a common well is significant. In this case, the optical molasses results in radiative escape of these pairs of atoms. The decay of the level of fluorescence to a steady state value indicates that this loss mechanism effectively removes all pairs within 150 ms. The steady state fluorescence level then corresponds to the atoms which are trapped in individual potential wells of the HDT. The presence of these atoms is shown by releasing all the atoms from the HDT by shortly switching off and on both the trapping laser and the optical molasses. After this, the background fluorescence without atoms is recorded, see Fig. 4.25 between 620 ms and 660 ms. This level is significantly lower than the atomic fluorescence level at the end of the illumination. Indeed, this decay is caused by two-atom losses and not by single-atom losses.

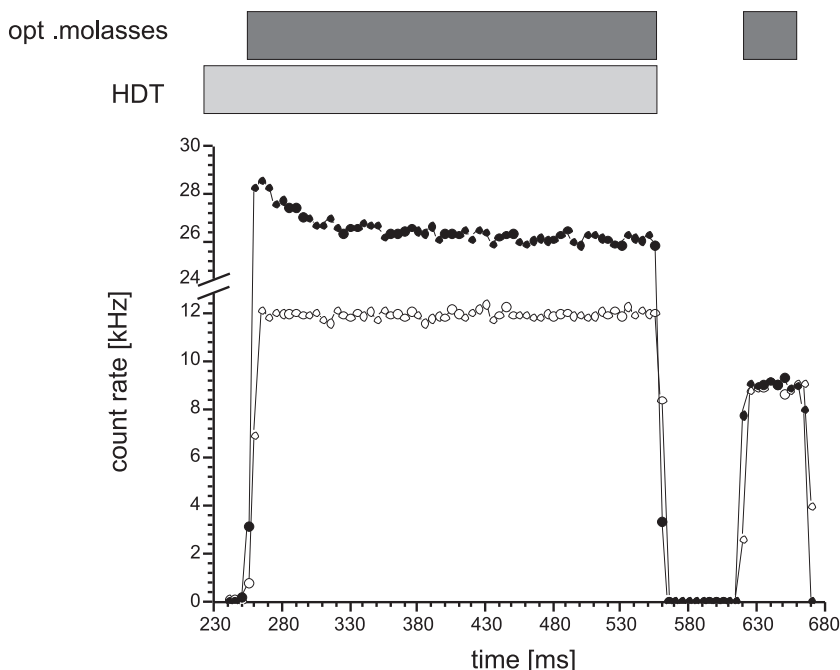


Figure 4.25: Light induced collisions in the HDT. Fluorescence signal of on average 3 atoms (open circles) and on average 19 atoms (full circles) trapped in on average 25 potential wells of the HDT. At $t = 260$ ms the optical molasses illuminating the atoms is switched on. In the 3-atom case, the fluorescence level is constant over the 300 ms illumination time, indicating that no atoms are lost. In the 19-atoms case, however, the fluorescence signal exponentially decays towards a steady state value. This can be attributed to radiative escape collisions causing the loss of pairs of atoms which are trapped in the same potential well. At $t = 560$ ms, the remaining atoms are ejected from the HDT by switching off all lasers in order to measure the background signal due to stray light. Each of the two traces is averaged over 100 shots. Note that the vertical scale is interrupted between 12 and 24 kHz.

4.8.3 Experimental results

In this experiment we have repeated the experimental sequence for on average 25 times. But since we cannot distinguish a two-atom loss due to radiative escape after successfully joining the atoms in one potential well from a two-atom loss due to two uncorrelated one atom losses during the experimental sequence, we have performed in addition to the main experiment two independent cross checks. For this purpose, we have carried out the entire experimental sequence with only one atom: an atom present in the VDT and the HDT is empty, and an atom present in the HDT and the VDT is empty. Every cross check was repeated for about 20 times. The whole sequence, consisting of the main experiment followed by the two cross checks, was repeated altogether seven times.

The corresponding single atom loss probabilities in both cross checks were measured to be $p_V = 6.5^{+2.1}_{-2.4}$ % and $p_H = 0.0^{+3.5}_{-0.0}$ %, respectively. From these measurements, we infer the probability for two *uncorrelated* one atom losses during the experimental sequence to

be

$$p_{\text{uncorr}} = p_V \cdot p_H = 0.0_{-0.0}^{+0.2} \%.$$

At the same time, in the main experiment on joining two atoms in one well, we have measured a total two-atom loss probability of

$$p_{\text{meas}} = 16_{-3}^{+4} \%,$$

significantly higher than what was expected for uncorrelated events. The difference of these two values,

$$p_{\text{corr}} = p_{\text{meas}} - p_{\text{uncorr}} = 16_{-3}^{+4} \%,$$

is the probability for *correlated* two-atom losses. It stems from radiative escape of pairs of atoms proving the successful joining of the two atoms in one potential well, and therefore is our detected success rate in this experiment.

4.8.4 Analysis

The limiting factor for this success rate is the accuracy of the spatial manipulation of the trapped atoms with our dipole traps: we have determined that the position of an atom inserted with the VDT into the HDT fluctuates by $\delta y_{\text{insert}} = 0.82(\pm 0.11) \mu\text{m}$ rms, mainly caused by radial position fluctuations of the VDT. In addition, the accuracy of the transportation of an atom to a predetermined position of the HDT by means of the optical conveyor belt equals $\delta y_{\text{transp}} = 0.190(\pm 0.025) \mu\text{m}$ rms [22]. Assuming that both errors are Gaussian distributed, we can add them quadratically in order to determine the fluctuation of the position of the VDT with respect to the position of the potential well of the atom in the HDT while inserting the other atom with the optical tweezers into the HDT: $\delta y = (2\delta y_{\text{transp}}^2 + \delta y_{\text{insert}}^2)^{1/2} = 0.86(\pm 0.11) \mu\text{m}$. This yields a Gaussian probability distribution with a half-width of δy , giving the probability distribution to join two atoms in one well. Integrating this distribution over the size of one potential well of the HDT, see Fig.4.26, gives the probability p_{theor} to joint two atoms in one potential well of the standing wave of the HDT:

$$p_{\text{theor}} = \frac{p_{2\text{atoms}}}{\sqrt{2\pi} \delta y} \int_{-\frac{\lambda_{\text{HDT}}}{4}}^{\frac{\lambda_{\text{HDT}}}{4}} \exp\left(-\frac{y^2}{2\delta y^2}\right) dy ,$$

where $p_{2\text{atoms}} = (1 - p_V)(1 - p_H) = 94_{-5}^{+6} \%$ is the probability that none of the atoms gets lost during the manipulation. This results in the expected efficiency

$$p_{\text{theor}} = 23 \pm 3 \%$$

of placing two atoms into one well, which agrees reasonably with the experimentally determined success rate of $p_{\text{corr}} = 16_{-3}^{+4} \%$.

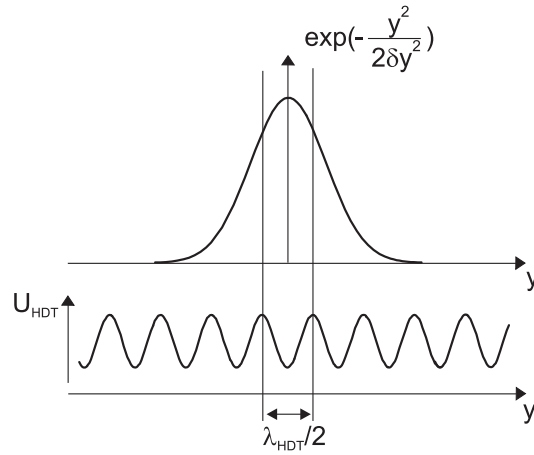


Figure 4.26: Probability distribution to join two atoms in one well. Integration of the distribution over the size of the potential well of the HDT gives the probability p_{theor} to joint two atoms in one potential well of the standing wave of the HDT.

4.8.5 Conclusion

Summarizing, we have joined two atoms in one and the same potential well of a standing wave optical dipole trap. The joining is realized by application of the distance control operation with the target final interatomic distance of zero. The experimental problem to detect the success of the manipulation was solved by inducing cold collisions between the atoms. This was realized by illuminating the atoms with an optical molasses, which leads to a two-atom loss if and only if both atoms reside in the same potential well. Using this detection method, we have experimentally determined a 16_{-3}^{+4} % success rate of the operation.

Chapter 5

Summary

The major achievement of this work is the realization of a technique allowing us to build strings of atoms with any desired interatomic separations and with high precision and efficiency. Initially, the desired number of atoms is prepared in a magneto-optical trap. These atoms are then transferred into a standing wave optical dipole trap. The rearrangement is carried out by extracting atoms out of the initial string in the standing wave dipole trap and by reinserting them back at predetermined positions using a second standing wave dipole trap as optical tweezers. Using this method, the distance between simultaneously trapped atoms can be actively controlled with a precision of $0.78(\pm 0.05) \mu\text{m}$ rms and a success rate of $98_{-5}^{+2} \%$. This precision corresponds to only 3-4 potential wells of the standing wave trap.

Further, this technique allows us to insert two atoms into a single potential well of a standing wave optical dipole trap and to deterministically induce interactions between them leading to light induced collisions. The detected success rate of the insertion of one atom into the potential well occupied by the other atom is $16_{-3}^{+4} \%$, which is limited by the precision of insertion with our optical tweezers.

Furthermore, I have presented models describing the processes of extraction and insertion of an atom with the optical tweezers. They allow to single out the main effects limiting the performance of these operations and to work out the strategies for their further improvements. Finally, I have addressed scalability, i. e., the possibility to apply our method to much larger number of atoms.

Chapter 6

Outlook

Using the technique of manipulating of atoms with optical tweezers presented in this thesis, we are able to control the separations between the atoms stored in the standing wave dipole trap at the level of the potential wells. We can prepare strings with interatomic separations large enough to allow addressing of individual atoms. Moreover, our method of placing an atom with the optical tweezers allows us to insert an atom even into an already occupied micropotential. The result of this work opens a route towards a broad range of further experiments with neutral atoms.

6.1 Quantum information processing

The essential resource for quantum computation is entanglement between qubits. Although bipartite entanglement is theoretically understood and characterized, the characterization and understanding of multi-particle entanglement is a challenging topic of quantum information theory and of great experimental interest [59, 60, 61]. Moreover, arrays of individually addressable entangled qubits (cluster states) form the basis of the one-way quantum computing concept [61]. A string of individually addressable neutral atoms serving as qubits presents a good starting point for the experimental implementation of many particle entangled states. There are several proposals for the realization of multi-particle entanglement in this system. These schemes require the separations between the atoms to be known and controlled. I discuss below two methods for the possible realization of entanglement in our system.

Cold collisions

One of the possibilities to produce entanglement in a string of optically trapped atomic qubits is to use coherent cold collisions [62]. If two atoms are located in the vicinity of each other, such that their respective spin wave functions overlap, they acquire a collisional phase. By properly adjusting the collision time, the states of the atoms can be entangled. One of the promising techniques, which allow us first to bring atoms into the contact and then to spatially separate them is the technique of spin dependent transport of single atoms [63]. It is based on the fact that at a “magic” wavelength of the standing wave

optical dipole trap, the trapping potential for atoms in state $|1\rangle$ is formed only by σ^+ polarization of the dipole trap laser, whereas the atoms in the state $|0\rangle$ are trapped in the σ^- component only. Therefore, atoms in different internal states will be shifted in different directions by shifting the trapping potentials with respect to each other.

We have already demonstrated a preparation of a pair of atoms with a well defined separation. Combination of this system with the technique of spin dependent transport would allow us to prepare an entangled state of two particles. Starting with an equidistant string of up to seven atoms would allow us to prepare a cluster state with individually addressable qubits, which is interesting for the realization of a one-way quantum computer. Spin dependent transport of thousands of atoms in optical lattices has already been realized [15], as well as the creation of a cluster state [16], but at a moment without the possibility to address individual atoms. A new setup, which would allow us to realize spin dependent transport of single atoms, is being built in our group.

Cavity quantum electrodynamics

An alternative possibility to entangle atomic qubits is to use cavity quantum electrodynamics. This can be realized by placing two atoms into a mode of high finesse cavity, which mediates the photon exchange between the atoms. We have recently built and installed into our experimental setup such a high finesse cavity [29]. Since the size of the cavity mode is about $20\ \mu\text{m}$, our strings of atoms with $15\ \mu\text{m}$ separations are thus well suitable for the cavity mediated entanglement of pairs of atoms.

There are several proposals of the realization of the cavity-mediated entanglement. Atoms of a string can be entangled using dissipation-assisted adiabatic passage by transporting them slowly through the cavity mode [64]. In another proposal the qubits are entangled pairwise using a four-photon Raman process [65, 40].

6.2 “Nano-chemistry”

Another interesting application of optically trapped atoms is “nano-chemistry”, where one engineers molecules out of its constituents. We have used our optical tweezers to localize exactly two atoms in one micropotential. These two atoms could then be bound into a stable dimer molecule using photoassociation [11, 12] or Feshbach resonance [13] techniques. Thousands of such chemical reactions carried out in parallel in an optical lattice were already realized experimentally [17, 18, 19, 20, 21]. An alternative to inserting two atoms into one micropotential with the optical tweezers is to use spin dependent transport. The newly built setup will thus allow us to follow this approach as well.

6.3 Quantum simulations

Although the realization of at least part of the above mentioned schemes for the creation of entangled states seems to be feasible already in the near future, there are still several steps more to be done towards the solution of computational problems which are difficult

or not possible with present classical computers [8, 7]. Such calculations require quantum computers with thousands of qubits, which have to be fully controlled. On the other hand, there is another set of problems in theoretical physics, e. g., quantum many-body problems in solid state physics, which are not possible to simulate on a classical computer, because of the presence of too many parameters, but which can be efficiently simulated on a quantum simulator, as it was initially proposed by Feynman [9]. Arrays of optically trapped neutral atoms are good candidates for a quantum simulator. There are already several proposals to perform universal simulation of quantum dynamics using such atomic arrays [10, 66, 67], to simulate ferromagnetism and spin squeezing [68].

Our strings of equidistantly spaced atoms are thus suitable candidates for the physical realization of the above mentioned proposals, which require 1d strings of atoms with the possibility to address each of them.

Appendix A

Design and adjustment of the optical tweezers

During my thesis I developed a lens system of the optical tweezers, the vertical dipole trap (VDT). This system allows us to tightly focus the beam of the VDT, and thereby to reach a small size of the optical tweezers. The small size is necessary for picking up of individual atoms from the HDT (our “object holder”) and for placing back the atoms with high precision at the desired position on the object holder.

A.1 Design goals

In addition to the requirement of the tight focusing of the laser beam of the tweezers, we should be able to integrate the tweezers into the existing experimental setup for trapping single atoms. The summarized requirements for the optical system of the VDT are:

- We want to reach the tightest possible focusing of the beam of the VDT, which is compatible with the geometry of our experimental system, with minimal diffraction effects and spherical aberrations.
- The minimum distance between the last lens (L), which focuses the beam of the VDT on to the MOT, and the glass cell is 160 mm, see Fig. 2.7. This distance is determined by our experimental setup, because the vertical beam of the MOT, which coincides with the axis of the VDT, should not be affected by this lens.
- If possible, usage of catalog lenses to reduce the cost of the system.

A.2 Design of the optical system

We want to have a system with maximum possible lens size, which practically fits to the experimental system. Lenses with 2-inch size fulfill this criterion. A system, with a 2-inch aperture and a focal length of about 160 mm, will then have a numerical aperture on the order of 0.1. At this numerical aperture special attention should be paid to the

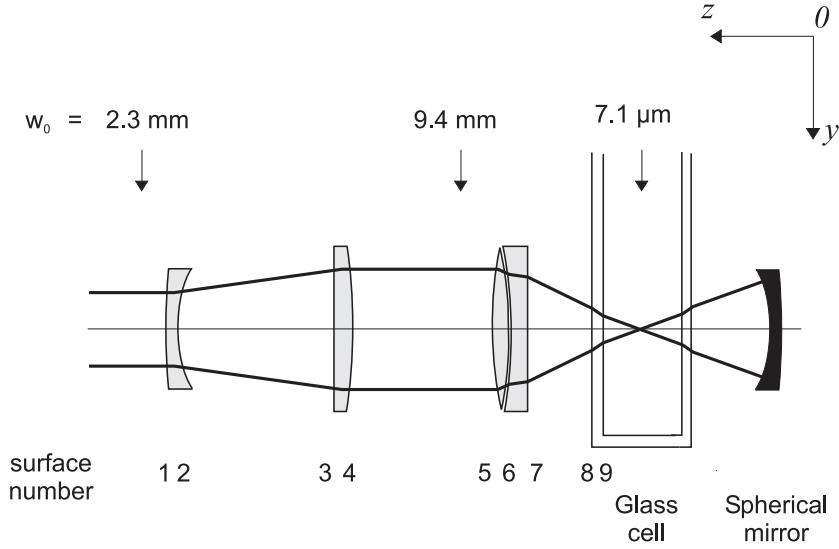


Figure A.1: Layout of the optical system of the VDT. The telescope consists of a meniscus lens (surfaces 1 and 2) and a plan convex lens (surfaces 3 and 4). A laser doublet lens (surfaces 5, 6 and 7) focuses the beam through the wall of the glass cell (surfaces 8 and 9). The two plane mirrors between the surfaces 4 and 5 are not shown, for they do not introduce aberrations. The waist radius in front of the telescope is a measured radius, whereas the other sizes are calculated. The sizes of the beam are exaggerated for presentation purposes.

spherical aberration of the system. Spherical aberrations can be minimized either by using aspheric lenses (which were not used in this system, for they are usually expensive) or by using a multi-lens system with spherical surfaces, where the aberrations of one surface are compensated by the aberrations of the other ones.

In our experimental setup, we have a beam with a waist of $2.25(\pm 0.03)$ mm. This beam has to be first expanded and then focused to the desired waist with the optical system of the VDT. Additionally, because of space limitations due to the existing experimental setup, it is desirable to physically separate the beam-expansion part of the optical system from the final focusing lens. In the simplest possible configuration, one has to use two lenses as a telescope to expand the beam and one lens for the final focusing.

Using this starting information about the desired optical system, I have used the program Oslo LT Edition (Version 6.1 from Lambda Research Corporation, free downloadable from <http://www.lambdares.com>) to design a system with minimal spherical aberrations. The program traces bundle of rays through the lenses and calculates the point spread function at the image plane, including effects of diffraction and aberrations. It computes as well the wave front error, which is a measure of the deviation of the current optical system from an ideal aberration free system. I have minimized this error by trying different combinations of standard catalog lenses.

The result of the optimization is shown in Fig. A.1 and Table A.1. The system consists

Table A.1: Specifications of the lens system.

Surface no.	Radius of curvature [mm]	Distance to next surface [mm]	Material
1	627.40	2.50	BK7
2	24.70	149.96	air
3	∞	7.00	BK7
4	-103.10	200.00	air
5	120.36	9.50	SK11
6	-80.89	4.00	SF5
7	-341.67	152.00	air
8	∞	5.00	silica
9	∞	25.00	vacuum

of three catalog lenses: a meniscus lens (diameter 1-inch, model CMN11405/100 with MgF₂ coating from BFI OPTILAS GmbH), a plan-convex lens (diameter 2-inch, model LPX50B/200 with NIR coating from Lens-Optics GmbH) and a diode laser glass doublet lens (diameter 2-inch, model 06LAI015/077 with NIR coating from MELLES GRIOT).

The simulation shows that the wave front error in the image surface is on the order of $\lambda_{\text{VDT}}/20$. The waist radius of the focused beam is 6.9 μm . The same was simulated using purely Gaussian beam optics, neglecting all aberrations and diffraction effects. This simulation yields a waist radius of $w_0 = 6.7 \mu\text{m}$ with a Rayleigh length of $z_0 = 137 \mu\text{m}$. It is interesting to note, that with the current numerical aperture, the introduction of an additional plane silica window, corresponding to the wall of the glass cell of the vacuum setup, does not introduce significant spherical aberrations but only shifts the position of the waist.

A.3 Adjustment of the optical tweezers

Incoming beam of the VDT

The first step of the installation of the optical system of the VDT consists of the adjustment of the distance between the first two lenses of the optical system comprising a telescope. The collimation of the expanded beam was checked with a shear plate interferometer (model 09 SPM 001 from MELLES GRIOT). In order to reach full flexibility for the alignment of the beam through the final focusing lens, we installed two 45°-mirrors (standard 2-inch mirror with NIR coating from Lens-Optics GmbH) between the telescope and this lens. Since the mirrors are tilted by 45° degree with respect to the beam, they introduce the smallest aperture in the focusing system of $D = a_{\text{M}}/\sqrt{2} = 32.5 \text{ mm}$, where $a_{\text{M}} = 46 \text{ mm}$ is the clear aperture of the mirror. These values will be important for the analysis of the beam clipping in App. C.

In the second step of the installation, we have adjusted the path of the vertical beam of the MOT, in order to combine the beam of the VDT with the MOT beam. For this purpose we have installed a dichroic mirror (2-inch mirror with special coating from Lens-Optics GmbH), which transmits about 96% of the laser light at 852 nm and reflects 99% of the

laser light at 1030 nm, see Fig. 2.7. The changes of the polarization of the MOT beams due to the dichroitic mirror were then compensated by the corresponding polarization optics in the MOT beams.

The third step consists of the axial positioning of the final focusing lens L of the VDT, see Fig. 2.7. The aim of this alignment is to focus the beam of the VDT onto the MOT. As the criterion for the adjustment we have used the fact that the beam of the VDT, if it hits the MOT with a single trapped atom, will cause a light shift of the Cs energy levels proportional to the local intensity of the VDT, which results in a reduction of the fluorescence signal from the MOT. The estimated precision of our alignment along the beam axis was about $100 \mu\text{m}$, which is smaller than the Rayleigh length $z_0 = 137 \mu\text{m}$ of the Gaussian beam of the VDT.

Creation of the standing wave

So far, we have discussed only the transverse geometry of the VDT. The tight axial confinement in the trap is reached by creating a standing wave. The easiest way to minimize the aberrations of the counter propagating beam is to reflect the incoming beam on a spherical mirror (diam. 50 mm with a radius of curvature -250 mm, surface quality $\lambda/10$ and HR coating for 1030-1064 nm from LASER COMPONENTS GmbH). The mirror has to be positioned at the position along the axis of the VDT where the curvature of the mirror matches the curvature of the wave front of the incoming Gaussian beam. As the adjustment criterion we have used the fact that the retro reflected beam should be again collimated after it passes back through the final focusing lens L , see Fig. 2.7. This was checked by placing a beam splitter between the lens and the telescope and observing the reflected beam again with a shear plate interferometer. The final wave front aberration, as measured with the shear plate interferometer, was less than $\lambda_{\text{VDT}}/4$ in the central part of the beam.

A.4 Experimental test of the performance of the VDT

The waist of the resulting dipole trap was expected to be $6.9 \mu\text{m}$. The oscillation frequency measurement of the atoms in the VDT allowed us to measure the waist of the resulting trap, see Sec. 2.2.4. The result shows that the trap profile is elliptic with the widths $10.1 \mu\text{m}$ and $7.2 \mu\text{m}$. The analysis suggests that the observed ellipticity is most probably due to the adjustment procedure of the VDT, see App. C.

Appendix B

Driving electronics of the EOM

The measurement of the oscillation frequency of the atoms in the VDT requires a slow controllable lowering of the depth of the trap on the time scale of few hundred milliseconds, and a fast modulation with the frequencies up to 2 MHz.

We control the power of the laser beam of the trap with the EOM installed between two crosses polarizers. The $\lambda/2$ -voltage of the EOM is 8 kV. This voltage is supplied by a high voltage (HV) amplifier (model HEOPS-10P2-L from hivolt.de GmbH), which amplifies a 0-10 V signal from the analog output of the computer control. Since the bandwidth of the HV-amplifier is limited to 5 kHz, it cannot be directly used for the fast trap modulation but only for changing the voltage offset on the EOM necessary for the tap lowering. In order to have a possibility to slowly lower the depth of the trap and to perform the fast modulation of the EOM, we combine the high voltage from the HV-amplifier and the RF-signal at the necessary frequency from an RF-generator (model SML02 from Rhode & Schwarz), see Fig. B.1. The frequency of the RF-generator is controlled using the digital output of the computer control. The signal from the RF-generator is amplified by a video amplifier (type 250 series video amplifier from LEYSOP Ltd.), which has a bandwidth of DC-5 MHz. The video amplifier produces up to 220 V_{pp} between the inner poles of the outputs 1 and 2.

The corresponding schematic of the EOM control is presented in Fig. B.1. The capacitors C_2 and C_3 decouple the DC high voltage of the HV-amplifier from the video amplifier. R_1 , R_2 and C_1 build a low pass filter to prevent a leakage of the RF-modulation voltage into the HV-amplifier. The EOM is DC-grounded using R_3 .

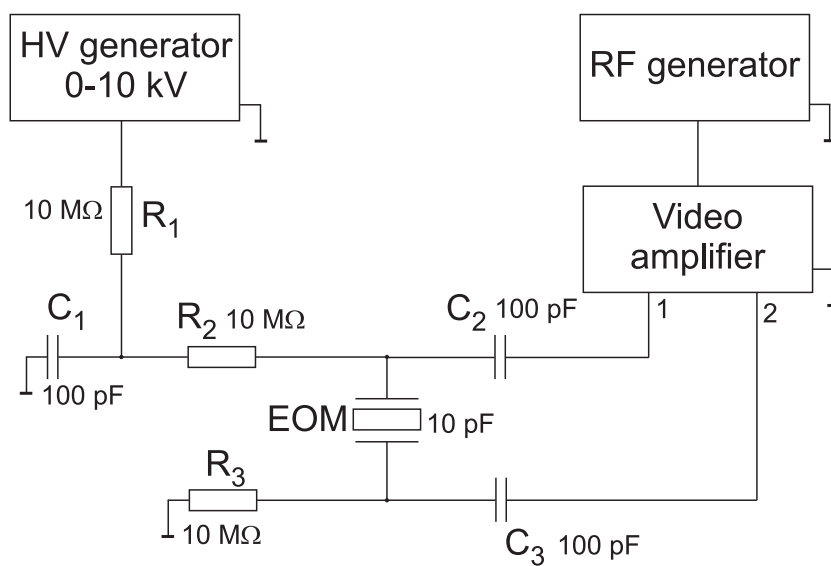


Figure B.1: Driving electronics of the EOM.

Appendix C

Analysis of the ellipticity of the VDT

In the oscillation frequency measurement, see Sec. 2.2.4, we have observed two separate peaks in the spectrum of the radial frequency measurement, see Fig. 2.10b. The presence of two peaks shows that the radial symmetry of the trap is broken and the radial profile of the VDT is elliptic. This profile can be described by two waists $w_{\text{VDT1}} = 10.1(\pm 1.4) \mu\text{m}$ and $w_{\text{VDT2}} = 7.2(\pm 1.2) \mu\text{m}$. In order to interpret this result, to evaluate the quality of the VDT lens system as well as to interpret the result of the measurement of the extraction resolution of the optical tweezers, see Sec. 4.3, we develop a quantitative model.

The cause of the ellipticity can be either the fact that the reflected beam is slightly shifted with respect to the incoming beam of the VDT, or that the laser beam has a small astigmatism, which can as well result in an ellipticity of the radial profile of the VDT at the position of the MOT. The astigmatism could be caused by the beam going at an angle through one of lenses of the optical system of the VDT.

In order to identify a potential reasons of the observed ellipticity, I have numerically modeled two cases: tilted retro-reflecting spherical mirror and tilted last focusing lens L , see Fig. 2.7.

C.1 Tilted retro-reflecting mirror

Here, I assume that the retro-reflecting mirror is slightly tilted. Since the spherical mirror is 25 cm from the MOT, any small tilts of the mirror will result in significant displacements of the reflected beam at the position of the MOT. We limit ourself to the case, where the reflected beam is displaced by not more than the waist of the incoming beam, which correspond to the mirror tilts of less than 0.1 mrad.

The interference pattern created by two counter propagating beams with their waists

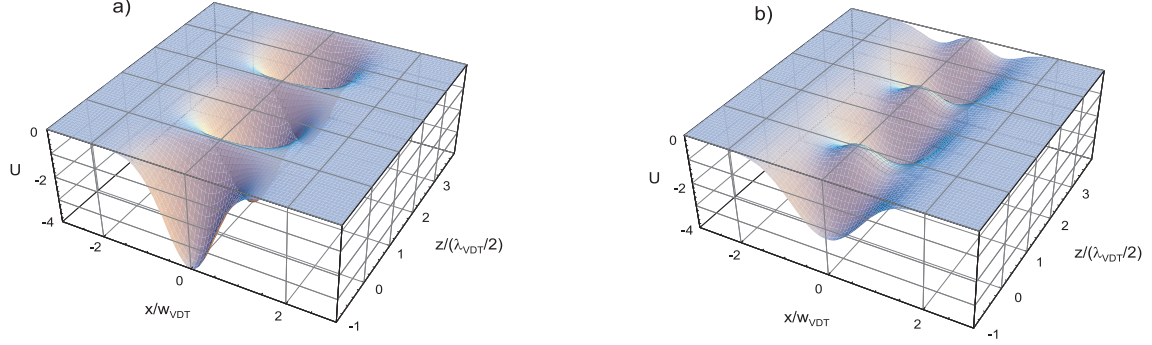


Figure C.1: Trapping potential in the x - z -plane. a) Two beams without any displacement ($d = 0$). b) Two Gaussian laser beams are displaced by one waist of the beam ($d = w_{\text{VDT}}$). The energy scale is in arbitrary units, but the same for a) and b). The scale in the z -direction is stretched by about one order of magnitude for the visualization purposes.

w_{VDT} displaced by d along the x -axis is described by

$$U_{\text{VDT}}^d(x, y, z) = -\frac{1}{4}U_{\text{VDT}}^0 e^{-\frac{2((x-\frac{d}{2})^2+y^2)}{w_{\text{VDT}}^2}} - \frac{1}{4}U_{\text{VDT}}^0 e^{-\frac{2((x+\frac{d}{2})^2+y^2)}{w_{\text{VDT}}^2}} - \frac{1}{2}U_{\text{VDT}}^0 e^{-\frac{2(x^2+y^2)}{w_{\text{VDT}}^2}} e^{-\frac{d^2}{2w_{\text{VDT}}^2}} \cos(2k_{\text{VDT}} \cdot z), \quad (\text{C.1})$$

where the first two terms represent the running wave dipole traps, created by the incoming and the reflected beams individually. The last term represents the interference pattern. The resulting trapping potential is visualized in Fig. C.1 for the case of $d = 0$ and of $d = w_{\text{VDT}}$.

The depth of the trap is decreased by a factor of about two by the displacement, due to the reduction of the contrast, see Fig. C.2. The corresponding axial oscillation frequency is

$$\Omega_{\text{ax}}^d = \Omega_{\text{ax}} e^{-\frac{d^2}{4w_{\text{VDT}}^2}}, \quad (\text{C.2})$$

where

$$\Omega_{\text{ax}} = 2\pi \sqrt{\frac{2U_{\text{VDT}}^0}{m_{\text{Cs}} \lambda_{\text{VDT}}^2}} \quad (\text{C.3})$$

is the axial frequency for $d = 0$.

The radial confining potential along the x -direction for the case with beam displacement is wider than without beam displacement, see the solid and the dashed lines, respectively, in Fig. C.2. The width of the confining radial potential in the y -direction is the same in both cases. Due to this ellipticity of the trap, there are two radial oscillation frequencies

$$\Omega_{\text{rad1}}^d = \Omega_{\text{rad}} e^{-\frac{d^2}{4w_{\text{VDT}}^2}} \sqrt{1 - \frac{d^2}{2w_{\text{VDT}}^2}}, \quad (\text{C.4})$$

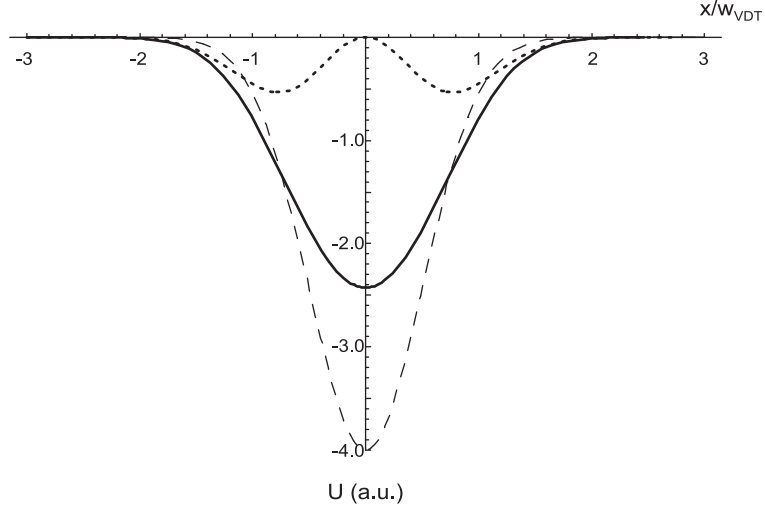


Figure C.2: Radial confining potential. The dashed line presents the profile of the trapping potential without beam displacement at the antinode of the standing wave. The potential has an $1/e^2$ -half width of w_{VDT} and a depth of 4 arbitrary units. With a beam displacement of $d = w_{\text{VDT}}$, the trapping profile at the antinode is shown as the solid line. Its $1/e^2$ -half width is $1.4w_{\text{VDT}}$. The dotted line presents the trapping profile at the position of the antinode of the standing wave.

$$\Omega_{\text{rad}2}^d = \Omega_{\text{rad}} e^{-\frac{d^2}{4w_{\text{VDT}}^2}}, \quad (\text{C.5})$$

where

$$\Omega_{\text{rad}} = \sqrt{\frac{4U_{\text{VDT}}^0}{m_{\text{Cs}}w_{\text{VDT}}^2}} \quad (\text{C.6})$$

is the radial oscillation frequency without displacement.

In order to reach the measured ratio of the two oscillation frequencies of $\Omega_{\text{rad}2}/\Omega_{\text{rad}1} = 1.4$, the displacement of the beams at the position of the MOT should be $d = 7.2 \mu\text{m}$, which is about the size of the MOT itself and is in the range of the experimentally realistic values. For the given beam displacement $d = 7.2 \mu\text{m}$, the depth of the dipole trap will be reduced from the ideal case of perfectly aligned beams of $U_{\text{ideal}}/k_{\text{B}} = 7.5 \text{ mK}$ by a factor of $\exp\left(-\frac{d^2}{2w_{\text{VDT}}^2}\right) \approx 0.6$. Due to the diffraction on the apertures, see Sec. A.3, we expect an additional reduction of the laser intensity maximum in the focus, and thereby of the depth of the trap, by [Siegman]:

$$\eta = \left(1 - \exp\left(-\frac{D^2}{4w^2}\right)\right)^2, \quad (\text{C.7})$$

where D is the diameter of the aperture, and w is the waist radius of the beam before the aperture. For $D = 32.5 \text{ mm}$, see App. A, and $w = 9.2 \text{ mm}$, this equation yields $\eta \approx 0.9$. This gives an expected depth of the dipole trap of $U_{\text{calc}}/k_{\text{B}} = 4.0 \text{ mK}$, which is higher than the value of 2.7 mK obtained from the measured axial oscillation frequency.

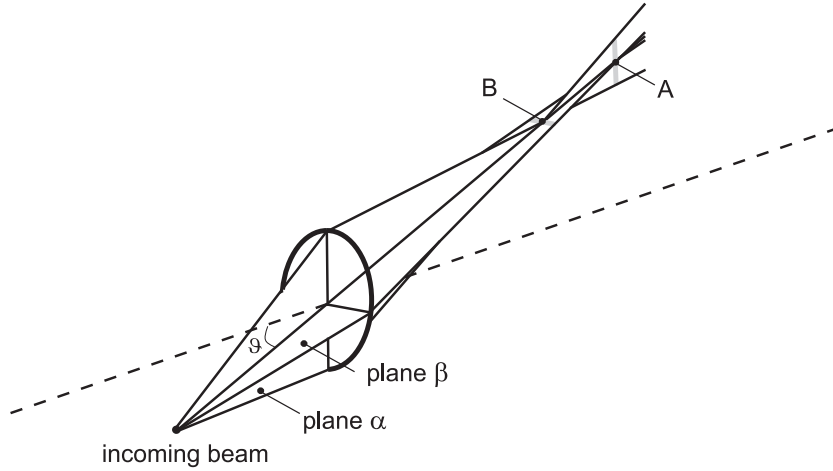


Figure C.3: A lens tilted relative to the incoming beam creates an astigmatic beam. It has two foci at the positions A and B.

C.2 Tilted lens

The second effect, which can explain the ellipticity of the VDT during the oscillation frequency measurement is the presence of an astigmatic aberration. In this case the focused beam has two foci at two different positions along the beam in two perpendicular planes, see Fig. C.3. The beam cross sections in the points A and B are elliptic.

Incoming beam

In this simulation, I assume that the final focusing lens L of the VDT, see Fig. 2.7, is slightly tilted relative to the beam. This tilt results in the astigmatic aberration of the beam, and consequently, in the ellipticity of the radial profile of the trap. The numerical simulation with the Oslo program shows, that a tilt of the lens by $\vartheta = 1.75^\circ$ is enough to explain the measured ellipticity of the trap. This is a realistic tilt, for we had to align the lens to a big beam at a short distance. The program shows the beam will have two foci separated by $190 \mu\text{m}$. At the position A, the beam is focused to the waist of $w_{A\beta} = 7.1 \mu\text{m}$ in the plane β , whereas in the perpendicular plane α , the width of the beam is $w_{A\alpha} = 10.2 \mu\text{m}$. At the position B the width of the beam is $w_{B\beta} = 11.4 \mu\text{m}$ in the plane β and $w_{B\alpha} = 6.8 \mu\text{m}$ in the plane α .

Reflected beam

For the creation of the standing wave the beam is retro reflected from the spherical mirror, see Fig. 2.7. Further, I assume in this simulation that the center of the curvature of the mirror coincides with the focus A, see Fig. C.4.

We first consider the incoming and the reflected beams in the plane β . Since the center of the curvature of the retro reflecting mirror co-insides with the point A, the beam in this plane is retro reflected, see Fig. C.4a. The size of the reflected beam is $w_{B\beta}^{ref} = 11.4 \mu\text{m}$ and

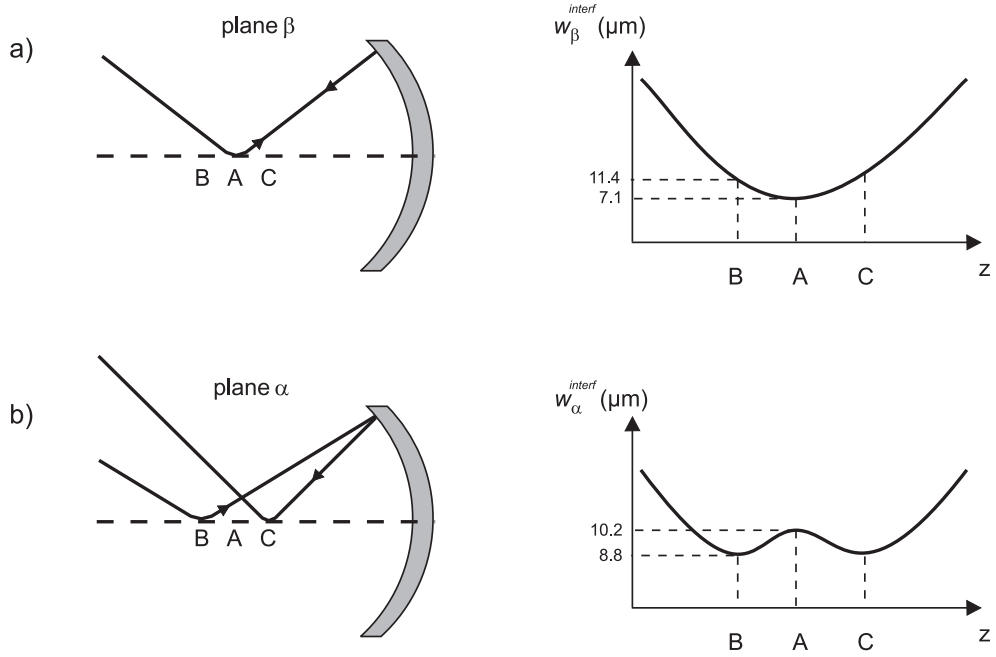


Figure C.4: Incoming and the reflected beams in planes α and β . a) In the plane β , the waists of the incoming and of the reflected beams are at point A, corresponding to the center of curvature of the spherical mirror. b) In the plane α , the waist of the incoming beam is at point B and of the reflected beam is at point C. On the righthand side is the profile along the beam axis z of the beam size of the resulting interference pattern in each case.

$w_{A\beta}^{ref} = 7.1 \mu\text{m}$ in points B and A, respectively. The beam profile of the reflected beam along the beam axis is the same as for the incoming beam. Therefore, the transverse profile of the produced interference pattern can be easily determined. It has a width of $w_{B\beta}^{interf} = 11.4 \mu\text{m}$ at point B and $w_{A\beta}^{interf} = 7.1 \mu\text{m}$ at point A, see Fig. C.4a.

For the plane α , the incoming beam is reflected and refocused at the point C, see Fig. C.4b. The parameters of the reflected beam are calculated from the following considerations: The distance between points A and B is three orders of magnitude smaller than the radius of curvature of the spherical mirror R . Therefore, the distance between A and C approximately equals the distance AB. Moreover, since $AC \ll R$, we can neglect the refocusing to a different waist size by the spherical mirror. Therefore, we approximate the reflected beam by a Gaussian beam with the same waist as the incoming beam, but with a new position at point C. The calculated sizes of the reflected beam at the points A and B are $w_{A\alpha}^{ref} = 10.2 \mu\text{m}$ and $w_{B\alpha}^{ref} = 13.7 \mu\text{m}$, respectively. The incoming beam interferes with the reflected beam, producing a standing wave. The profile of the resulting standing wave dipole trap is calculated in the following way.

Consider interference of two counter propagating Gaussian beams with different widths $w_1(z)$ and $w_2(z)$ at a certain point z along the beam axis, neglecting the curvature of the

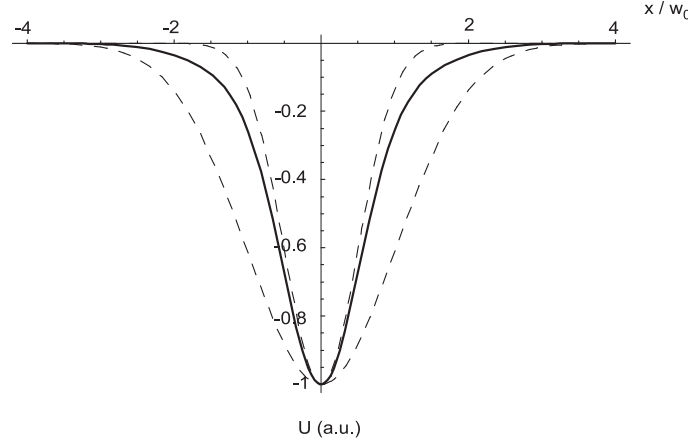


Figure C.5: Transverse shape of the standing wave dipole trap from two different Gaussian beams with the beam sizes w_0 and $2w_0$. The profiles of the individual Gaussian beams are shown as dashed lines. The solid line presents the resulting radial shape with the width of $1.3w_0$.

wave front:

$$U_{\text{VDT}}^x(x, z) = -\frac{1}{4}U_{\text{VDT}}^0 e^{-\frac{2x^2}{w_1^2}} - \frac{1}{4}U_{\text{VDT}}^0 e^{-\frac{2x^2}{w_2^2}} - \frac{1}{2}U_{\text{VDT}}^0 e^{-x^2(\frac{1}{w_1^2} + \frac{1}{w_2^2})} \cos(2k_{\text{VDT}} \cdot z). \quad (\text{C.8})$$

The transverse profile of this potential for the case of w_2 twice as big as w_1 at $z = 0$ at antinode is presented in the Fig. C.5. From the Eq. C.8, one calculates the width of the resulting potential at the point B from the two counter propagating Gaussian beams with widths of $w_{B\alpha} = 6.8 \mu\text{m}$ and $w_{B\alpha}^{\text{ref}} = 13.7 \mu\text{m}$ to be $w_{B\alpha}^{\text{interf}} = 8.8 \mu\text{m}$. For the point A one has $w_{A\alpha}^{\text{interf}} = 10.2 \mu\text{m}$ from the interference of two Gaussian beams with the widths of $w_{A\alpha}^{\text{ref}} = 10.2 \mu\text{m}$ and $w_{A\alpha} = 10.2 \mu\text{m}$. From the analogous considerations one calculates the profile of the standing wave at the point C.

Profile of the standing wave trap

The standing wave at the point A has an elliptic cross section with the beam sizes of 10.2 and 7.1 μm , see Fig. C.4. For the point B the beam widths are 8.8 and 11.4 μm , respectively. This qualitatively shows that even a small tilt of the order of one degree of the final focusing lens results in astigmatic aberrations of the focused beam, and thereby in the elliptic profile of the resulting dipole trap. If we assume that the MOT was at the position A of the trap during the oscillation frequency measurement, the measured oscillation frequencies can be quantitatively explained with this model. The expected trap depth can be estimated as well using this model. The Oslo program simulations show that the astigmatism at the point A contributes a factor of about 0.7 to the reduction of the trap depth relative to the ideal case without aberrations. The diffraction effects contribute a

factor of about 0.9, see above. All together, one expects the drop of the maximal intensity by a factor of about 0.6, relative to the ideal case. This yields the expected depth of the dipole trap at the point A of $0.6 \cdot U_{\text{ideal}}/k_B = 4.5$ mK, which is higher than the measured 2.7 mK, see Sec. 2.2.4.

C.3 Analysis

We have demonstrated that both models are compatible with the results of the oscillation frequency measurement, i. e., observation of the ellipticity of the VDT radial profile. Therefore, it is not possible on the basis of this one experiment to rule out one of these theories.

Nevertheless, the result of the measurement of the size of the optical tweezers, see Sec. 4.3.2, is compatible only with the astigmatic beam assumption. From the fit of the experimental data from this experiment, we have determined that the waist size of the optical tweezers along the HDT axis is $w_{\text{VDT}} = 11.8(\pm 0.2)$ μm . Although the VDT with this radial size can be created by misaligning the beams, the profile of the axial force exerted by the VDT during the extraction of the atoms from the HDT has a Gaussian shape with the width, corresponding to the perfectly adjusted trap. This can be readily see by taking the partial derivative of Eq. C.1 in the z -direction

$$F_z^d = -\frac{\partial}{\partial z} U_{\text{VDT}}^d = U_{\text{VDT}}^0 e^{-\frac{2(x^2+y^2)}{w_{\text{VDT}}^2}} e^{-\frac{d^2}{2w_{\text{VDT}}^2}} \sin(2k_{\text{VDT}}z) k_{\text{VDT}} \quad (\text{C.9})$$

Therefore this assumption does not produce the geometry of the VDT, necessary to explain the results of the extraction experiment. In contrast, if the ellipticity is caused by astigmatic beams, the radial profile of the axial force equals to the profile of the potential, as can be seen by taking the partial derivative of Eq. C.8:

$$F_z^x = -\frac{\partial}{\partial z} U_{\text{VDT}}^x = U_{\text{VDT}}^0 e^{-x^2} e^{\frac{1}{w_1^2} + \frac{1}{w_2^2}} \sin(2k_{\text{VDT}}z) k_{\text{VDT}}. \quad (\text{C.10})$$

Therefore, this configuration produces the necessary geometry compatible with the results of the extraction experiment.

Appendix D

Temperature of an atom from an ICCD image

The radial extent ($\sigma_{\text{HDT}}^v = 3.31(\pm 0.08) \mu\text{m}$) of the fluorescence image of an atom trapped in the HDT micropotential, see Fig. 2.13, is defined by the temperature of the atoms and by the resolution of our imaging system. The width of the point spread function can be estimated from the axial extend of the image ($\sigma_{\text{HDT}}^h = 1.3(\pm 0.1) \mu\text{m}$), see Sec. 2.2.5. Since it is smaller than the radial extend, we can use the image to reveal information about the temperature of the trapped atom. We extract this temperature by modeling the thermal motion of the atom and comparing the prediction of the model with the measured spatial distribution in the ICCD image. One of the methods of a derivation of the final formula was presented in [29]. Here I present an alternative derivation.

Figure 2.13 shows an image of an atom trapped in a micropotential of the HDT and illuminated with three dimensional optical molasses after one second of integration on the ICCD. Since the typical velocity of a laser cooled Cs atom is ≈ 9 cm/s, this time is enough for the atom to cover many possible trajectories in the trap. Therefore, the intensity distribution in the image is proportional to the probability distribution to find an atom in a certain point in space.

In order to calculate the probability distribution, we approximate the potential of the HDT by a harmonic potential with a spring constant κ . The radiation force of the molasses (in the radial direction z) averaged over several scattering cycles and over several wavelengths can be expressed as a friction force with the friction parameter α . Approximating the atom as a point like particle at a temperature T , having a meaning of an average kinetic energy, random fluctuations of the friction force can be characterized by a diffusion constant $D = k_{\text{B}}T/\alpha$. We apply to this system the theory of Brownian motion to calculate the probability distribution [69]. The corresponding Fokker-Planck equation for atomic motion in the HDT illuminated with the optical molasses is [70]

$$\frac{\partial}{\partial t} f = \frac{\kappa}{\alpha} \frac{\partial}{\partial z} (zf) + D \frac{\partial^2}{\partial z^2} f. \quad (\text{D.1})$$

Here, $f(z, z_0, t)$ is the probability density for an atom to be at time t at z for the initial

atom position $z(t=0) = z_0$. The steady state solution of this equation reads

$$f(z, z_0, \infty) = \frac{1}{\sqrt{\pi}} \exp\left(-z^2 \frac{\kappa}{2k_{\text{B}}T}\right), \quad (\text{D.2})$$

which is a simple Gaussian with the $1/\sqrt{e}$ -radius of $\sigma_{\text{FP}} = \sqrt{\frac{k_{\text{B}}T}{\kappa}}$ and does not depend z_0 and D . In the case of the harmonic approximation of the radial potential of our HDT, the spring constant is

$$\kappa = \frac{U_{\text{HDT}}^0}{b^2}, \quad (\text{D.3})$$

where U_{HDT}^0 is the depth of the HDT, and b is the $1/\sqrt{e}$ -radius of the HDT beam. According to this model, the temperature of the atom is

$$T = \frac{\kappa \sigma_{\text{FP}}}{k_{\text{B}}}. \quad (\text{D.4})$$

Assuming that the width of the distribution σ_{FP} is the width of the observed spot, we infer the atomic temperature from an atomic ICCD image:

$$T = \frac{U_{\text{HDT}}^0}{k_{\text{B}}} \left(\frac{a}{b}\right)^2 \quad (\text{D.5})$$

with $a \equiv \sqrt{(\sigma_{\text{HDT}}^v)^2 - (\sigma_{\text{HDT}}^h)^2}$ is the radial width of the fluorescence spot corrected for the width of the point spread function of our imaging system. Note that, in [23] this formula was erroneously given with an extra factor of 2 in the denominator.

List of Figures

2.1	One-dimensional picture of the MOT	4
2.2	Three-dimensional scheme of the MOT	5
2.3	Simplified level scheme of the Cs atom	6
2.4	Experimental setup with the detection optics for the MOT fluorescence	8
2.5	Count rate of the APD detecting the fluorescence from the MOT	9
2.6	Light shifts for a two-level atom	12
2.7	Beams of the HDT, VDT and the vertical beam of the MOT	13
2.8	Block diagram of the laser systems of our dipole traps	15
2.9	Measurement of the lifetime of the atoms in the HDT	16
2.10	Oscillation frequencies of the VDT	19
2.11	Measurement of the lifetime of the atoms in the VDT	20
2.12	Measurement of the lifetime of the atoms in our dipole traps in presence of the optical molasses cooling	22
2.13	CCD image of one atom in the HDT	23
2.14	Images of the same atom trapped in our dipole traps	24
3.1	Histograms of the fluorescence rate in the MOT	28
3.2	Experimental sequences of the preparation efficiency measurement	29
3.3	Efficiency of the preparation of N atoms in the HDT	30
3.4	Schematic presentation of ground state collisions between two atoms	32
3.5	Schematic presentation of light induced collisions between two atoms	33
3.6	Efficiency of the preparation of N atoms in the MOT	34
3.7	Collisional redistribution of atoms	36
3.8	Experimental sequence for measurement of the time scale of the MOT in- duced redistribution process	37
3.9	Simulated preparation efficiency of atoms in the HDT with the absence of the redistribution during the transfer from the MOT	38
3.10	Dependence of the preparation efficiency on the overlap time between the MOT and the HDT	39
3.11	Simulation of the preparation efficiency of the atoms in the MOT	42
3.12	Simulation of the preparation efficiency of the atoms in the HDT	43
3.13	Simulation of the preparation efficiency for $N = 10$ as the function of the overlap time between the MOT and the HDT	44

4.1	Scheme of the experimental setup for atom rearrangement	48
4.2	Histogram of measured distances and its fourier transform	50
4.3	Extraction of an individual atom out of the string	51
4.4	Trapping potentials along the z -axis	52
4.5	Decrease of the effective depth of the potential well	53
4.6	Probability for an atom to remain trapped in the HDT after the extraction	55
4.7	Image analysis for the determination of the width of the tweezers	56
4.8	Comparison of the experimental data and the respective theoretical expectation	58
4.9	Contour plot for $P_{\text{HDT}}(y_{\text{T}}^{\text{min}}, F_{\text{r}}) = 0.99$	61
4.10	Axial insertion	62
4.11	Radial insertion of an atom	63
4.12	Projection of a spatial distribution of a thermal atom onto the HDT	65
4.13	Experimental sequence for the characterization of the insertion precision	66
4.14	Insertion precision with and without cooling	67
4.15	Insertion precision as the function of the depth of the VDT	68
4.16	Insertion of an atom with the VDT into the HDT, which holds another atom	70
4.17	Radial potential of the two traps	71
4.18	Optimal depth of the VDT	72
4.19	Steps of the distance control	74
4.20	Actively controlling the distance between simultaneously trapped atoms	75
4.21	Zoom of the distribution of the final distances	76
4.22	Correlation between the final and the initial distance measurement	78
4.23	Sequence of the ICCD images of the step-by-step rearrangement of a string of three atoms	81
4.24	Building a regular string of seven neutral atoms	82
4.25	Light induced collisions in the HDT	85
4.26	Probability distribution to join two atoms in one well	87
A.1	Layout of the optical system of the VDT	96
B.1	Driving electronics of the EOM	100
C.1	Trapping potential of two displaced Gaussian laser beams	102
C.2	Radial confining potential	103
C.3	Beam through a tilted lens	104
C.4	Incoming and reflected beams in planes α and β	105
C.5	Transverse shape of the standing wave dipole trap from two different Gaussian beams	106

List of Tables

4.1	Width of the tweezers $2y_T^{\min}$ for different parameters	60
A.1	Specifications of the lens system.	97

Bibliography

- [1] M. ANDERSON, J. ENSHER, M. MATTHEWS, C. WIEMAN AND E. CORNEL, *Observation of Bose-Einstein Condensation in a Dilute Atomic Vapor*, Science **269**, 198 (1995)
- [2] C. BRADLEY, C. SACKETT, J. TOLLETT AND R. HULET, *Evidence of Bose-Einstein Condensation in an Atomic Gas with Attractive Interactions*, Phys. Rev. Lett. **75**, 1687 (1995)
- [3] K. DAVIS, M.-O. MEWES, M. ANDREWS, N. VAN DRUTEN, D. DURFEE, D. KURN AND W. KETTERLE, *Bose-Einstein Condensation in a Gas of Sodium Atoms*, Phys. Rev. Lett. **3969**, 1995 (75)
- [4] M. GREINER, O. MANDEL, T. ESSLINGER, T. W. HÄNSCH AND I. BLOCH, *Quantum phase transition from a superfluid to a Mott insulator in a gas of ultracold atoms*, Nature **415**, 39–44 (2002)
- [5] D. FRESE, B. UEBERHOLZ, S. KUHR, W. ALT, D. SCHRADER, V. GOMER AND D. MESCHEDE, *Single Atoms in an Optical Dipole Trap: Towards a Deterministic Source of Cold Atoms*, Phys. Rev. Lett. **85**, 3777 (2000)
- [6] S. KUHR, W. ALT, D. SCHRADER, M. MLLER, V.GOMER, AND D. MESCHEDE, *Deterministic Delivery of a Single Atom*, Science **293**, 278 (2001)
- [7] L. GROVER, *Quantum mechanics helps in searching for a needle in a haystack*, Phys. Rev. Lett. **97**, 325 (1997)
- [8] P. SHOR, *Polynomial-time algorithms for prime factorization and discrete logarithms on a quantum computer*, SIAM J. Comp. **26**, 1484 (1997)
- [9] R. P. FEYNMAN, *Simulating physics with computers*, Int. J. Theor. Phys. **21**, 467 (1982)
- [10] E. JANE, G. VIDAL, W.DÜR, P. ZOLLER AND J. CIRAC, *Simulation of quantum dynamics with quantum optical systems*, Quantum Information and Computation **Vol. 3**, 15–37 (2003)
- [11] D. JAKSCH, V. VENTURI, J. I. CIRAC, C. J. WILLIAMS AND P. ZOLLER, *Creation of a Molecular Condensate by Dynamically Melting a Mott Insulator*, Phys. Rev. Lett. **89**(4), 040402 (Jul 2002)
- [12] K. M. JONES, P. D. L. E. TIESINGA AND P. S. JULIENNE, *Ultracold photoassociation spectroscopy: Long-range molecules and atomic scattering*, Rev. of Modern Phys. **78**, APRIL–JUNE (2006)
- [13] T. KÖHLER AND K. GÓRAL, *Production of cold molecules via magnetically tunable Feshbach resonances*, cond-mat/0601420 (2006)
- [14] F. GERBIER, A. WIDERA, S. FÖLLING, O. MANDEL, T. GERICKE AND I. BLOCH, *Phase coherence of an atomic Mott insulator*, Phys. Rev. Lett. **95**, 050404 (2005)

-
- [15] O. MANDEL, M. GREINER, A. WIDERA, T. ROM, T. W. HÄNSCH AND I. BLOCH, *Coherent transport of neutral atoms in spin-dependent optical lattice potentials*, Phys. Rev. Lett. **91**, 010407 (2003)
- [16] O. MANDEL, M. GREINER, A. WIDERA, T. ROM, T.-W. HANSCH AND I. BLOCH, *Controlled collisions for multi-particle entanglement of optically trapped atoms*, Nature **425**(6961), 937–940 (October 2003)
- [17] T. ROM, T. BEST, O. MANDEL, A. WIDERA, M. GREINER, T. W. HÄNSCH AND I. BLOCH, *State Selective Production of Molecules in Optical Lattices*, Phys. Rev. Lett. **93**, 073002 (2004)
- [18] K. XU, Y. LIU, J. R. ABO-SHAER, T. MUKAIYAMA, J. K. CHIN, D. E. MILLER AND W. KETTERLE, *Sodium Bose-Einstein condensates in an optical lattice*, Phys. Rev. A **72**, 043604 (2005)
- [19] C. RYU, X. DU, E. YESILADA, A. M. DUDAREV, S. WAN, Q. NIU AND D. HEINZEN, *Raman-induced oscillation between an atomic and a molecular quantum gas*, cond-mat/0508201 (2005)
- [20] G. THALHAMMER, K. WINKLER, F. LANG, S. SCHMID, R. GRIMM AND J. H. DENSCHLAG, *Long-Lived Feshbach Molecules in a Three-Dimensional Optical Lattice*, Phys. Rev. Lett. **96**, 050402 (2006)
- [21] T. VOLZ, N. SYASSEN, D. M. BAUER, E. HANSIS, S. DÜRR AND G. REMPE, *A Mott state of molecules*, cond-mat/0605184 (2006)
- [22] I. DOTSSENKO, W. ALT, M. KHUDAVERDYAN, S. KUHR, D. MESCHÉDE, Y. MIROSHNYCHENKO, D. SCHRADER, AND A. RAUSCHENBEUTEL, *Submicrometer Position Control of Single Trapped Neutral Atoms*, Phys. Rev. Lett. **95**, 033002 (2005)
- [23] Y. MIROSHNYCHENKO, D. SCHRADER, S. KUHR, W. ALT, I. DOTSSENKO, M. KHUDAVERDYAN, A. RAUSCHENBEUTEL AND D. MESCHÉDE, *Continued imaging of the transport of a single neutral atom*, Optics Express **11**, 3498–3502 (2003)
- [24] D. SCHRADER, I. DOTSSENKO, M. KHUDAVERDYAN, Y. MIROSHNYCHENKO, A. RAUSCHENBEUTEL AND D. MESCHÉDE, *Neutral atom quantum register*, Phys. Rev. Lett. **93**, 150501 (2004)
- [25] T. W. HÄNSCH AND A. SCHAWLOW, *Cooling of Gases by Laser Radiation*, Opt. Commun. **13**(1), 68 (1975)
- [26] S. CHU, L. HOLLBERG, J. E. BJORKHOLM, A. CABLE AND A. ASHKIN, *Three-dimensional Viscous Confinement and Cooling of Atoms by Resonance Radiation Pressure*, Phys. Rev. Lett. **55**, 48 (1985)
- [27] E. L. RAAB, M. PRENTISS, A. CABLE, S. CHU AND D. E. PRITCHARD, *Trapping of Neutral Sodium Atoms with Radiation Pressure*, Phys. Rev. Lett. **59**, 2631 (1987)
- [28] S. KUHR, *A controlled quantum system of individual neutral atoms*, Ph.D. thesis, Universität Bonn (2003)
- [29] W. ALT, *Optical control of single neutral atoms*, Ph.D. thesis, Universität Bonn (2004)
- [30] W. ALT, *An objective lens for efficient fluorescence detection of single atoms*, Optik **113**, 142 (2002)
- [31] V. S. LETOKHOV, JEPT Lett. **7**, 272 (1968)

- [32] A. ASHKIN, *Trapping of Atoms by Resonance Radiation Pressure*, Phys. Rev. Lett. **40**, 729 (1978)
- [33] J. E. BJORKHOLM, R. FREEMAN, A. ASHKIN AND D. B. PEARSON, *Observation of Focusing of Neutral Atoms by the Dipole Forces of Resonance-Radiation Pressure*, Phys. Rev. Lett. **41**, 1361 (1978)
- [34] S. CHU, J. E. BJORKHOLM, A. ASHKIN AND A. CABLE, *Experimental observation of optically trapped atoms*, Phys. Rev. Lett. **57**, 314 (1986)
- [35] R. GRIMM, M. WEIDEMÜLLER AND Y. B. OVCHINNIKOV, *Optical dipole traps for neutral atoms*, Adv. At. Mol. Opt. Phys. **42**, 95 (2000)
- [36] A. ASHKIN, *Acceleration and Trapping of Particles by Radiation Pressure*, Phys. Rev. Lett. **24**, 156 (1970)
- [37] A. ASHKIN, *Observation of a single-beam gradient force optical trap for dielectric particles*, Opt. Lett. **11**, 288 (1986)
- [38] D. G. GRIER, *A revolution in optical manipulation*, Nature **424**, 810–816 (2003)
- [39] J. DALIBARD AND C. COHEN-TANNOUDJI, *Dressed-atom approach to atomic motion in laser light: the dipole force revisited*, JOSA B **2**, 1707 (1985)
- [40] D. SCHRADER, *A neutral atom quantum register*, Ph.D. thesis, Universität Bonn (2004)
- [41] M. E. GEHM, K. M. OHARA, T. A. SAVARD, AND J. E. THOMAS, *Dynamics of noise-induced heating in atom traps*, Phys. Rev. A **58**, 3914–3921 (1998)
- [42] D. SCHRADER, *Ein Förderband für einzelne Atome*, Diploma thesis, Universität Bonn (2000)
- [43] W. ALT, *Private communication*
- [44] W. WANIAK, *Image restoration by simple adaptive deconvolution*, Astron. Astrophys. Suppl. Ser. **124**, 197–203 (1997)
- [45] G. M. VAN KEMPEN, *Image Restoration in Fluorescence Microscopy*, Ph.D. thesis, Technische Universiteit Delft (1999)
- [46] S. KUHR, *Kalte Stöße mit einzelnen Atomen*, Diploma thesis, Universität Bonn (1999)
- [47] P. S. JULIENNE AND J. VIGUÉ, *Cold collisions of ground- and excited-state alkali-metal atoms*, Phys. Rev. A **44**(7), 4464–4485 (1991)
- [48] N. SCHLOSSER, G. REYMOND AND P. GRANGIER, *Collisional Blockade in Microscopic Optical Dipole Traps*, Phys. Rev. Lett. **89**, 023005 (2002)
- [49] N. SCHLOSSER, G. REYMOND, I. PROTSENKO AND P. GRANGIER, *Sub-poissonian loading of single atoms in a microscopic dipole trap*, Nature **411**, 1024 (2001)
- [50] B. UEBERHOLZ, *Kalte Stöße in einer magnetooptischen Falle mit hohem Magnetfeldgradienten*, Ph.D. thesis, Universität Bonn (2001)
- [51] S. BALI, D. HOFFMANN AND T. WALKER, *Novel Intensity Dependence of Ultracold Collisions Involving Repulsive States*, Europhys. Lett. **27**(4), 273–277 (1994)
- [52] S. DÜRR, M. K. W. AND W. C. E., *Improved loading of an optical dipole trap by suppression of radiative escape*, Phys. Rev. A **63**, 011401(R) (2000)
- [53] V. BAGNATO, D. E. PRITCHARD AND D. KLEPPNER, *Bose-Einstein condensation in an external potential*, Phys. Rev. A **35**, 4354–4358 (1987)

- [54] W. ALT, D. SCHRADER, S. KUHR, M. MLLER, V. GOMER AND D. MESCHEDE, *Single atoms in a standing-wave dipole trap*, Phys. Rev. A **67**, 033403 (2003)
- [55] H. J. LEE, C. S. ADAMS, M. KASEVICH, AND S. CHU, *Raman Cooling of Atoms in an Optical Dipole Trap*, Phys. Rev. Lett. **76**, 2658–2661 (1996)
- [56] H. PERRIN, A. KUHN, I. BOUCHOULE AND C. SALOMON, *Sideband cooling of neutral atoms in a far-detuned optical lattice*, Europhys. Lett. **42**, 395 (1998)
- [57] W. FALK, *Data reduction from experimental histograms*, Nucl. Instrum. and Methods in Phys. Res. **220**, 473 (1984)
- [58] S. J. M. KUPPENS, K. L. CORWIN, K. W. MILLER, T. E. CHUPP AND C. E. WIEMAN, *Loading an optical dipole trap*, Phys. Rev. A **62**, 013406 (2000)
- [59] W. DÜRR, G. VIDAL AND J. I. CIRAC, *Three qubits can be entangled in two inequivalent ways*, Phys. Rev. A **62**, 062314 (2000)
- [60] F. VERSTRAETE, J. DEHAENE, B. D. MOOR AND H. VERSHELDE, *Four qubits can be entangled in nine different ways*, Phys. Rev. A **65**, 052112 (2002)
- [61] H.-J. BRIEGEL AND R. RAUSCHENDORF, *Persistent entanglement in arraya of interacting particles*, Phys, Rev. Lett. **86**, 910 (2001)
- [62] D. JAKSCH, H.-J. BRIEGEL, J. CIRAC, C. GARDINER AND P. ZOLLER, *Entanglement of atoms via cold controlled collisions*, Phys. Rev. Lett. **82**, 1975 (1999)
- [63] G. BRENNEN, C. CAVES, P. JESSEN AND I. DEUTSCH, *Quantum Logic Gates in Optical Lattices*, Phys. Rev. Lett. **82**, 1060 (1999)
- [64] C. MARR, A. BEIGE AND G. REMPE, *Entangled-state preparation via dissipation-assisted adiabatic passages*, Phys. Rev. A **68**, 033817 (2003)
- [65] L. YOU, X. X. YI AND X. H. SU, *Quantum logic between atoms inside a high-Q optical cavity*, Phys. Rev. A **67**, 032308 (2003)
- [66] J. J. GARCÍA-RIPOLL, M. A. MARTIN-DELGADO AND J. I. CIRAC, *Implementation of Spin Hamiltonians in Optical Lattices*, Phys. Rev. Lett. **93**, 250405 (2004)
- [67] B. PAREDES, F. VERSTRAETE AND J. I. CIRAC, *Exploiting Quantum Parallelism to Simulate Quantum Random Many-Body Systems*, Phys. Rev. Lett. **95**, 140501 (2005)
- [68] A. SØRENSEN AND K. MØLMER, *Spin-Spin Interaction and Spin Squeezing in an Optical Lattice*, Phys. Rev. Lett. **83**, 2274–2277 (1999)
- [69] R. K. PATHRIA, *Statistical Mechanics, corrected reprint*, Pergamon, Oxford (1991)
- [70] V. GOMER, B. UEERHOLZ, S. KNAPPE, F. STRAUCH, D. FRESE AND D. MESCHEDE, *Decoding the dynamics of a single trapped atom from photon correlations*, Appl. Phys. B **67**, 689 (1998)

Acknowledgment

First of all I would like to thank professor Meschede for giving me the possibility to work on this fascinating experiment and professor Weitz for taking the role of the co-referee for my thesis.

The whole experimental setup is the result of the work of several generations of Ph.D. students preceding me. I had the wonderful possibility of working together with the "founders" of this experiment, S. Kuhr, D. Schrader and W. Alt, whom I would like to thank for the inspiring atmosphere they created while working on the experiment with me. The Ph.D. students of my generation I. Dotsenko, M. Khudaveryan and S. Reick I would like to thank for the collaborative teamwork in the lab and for supporting unorthodox and unusual ideas about new possible experiments (especially Mika, for not believing that two atoms can be placed in one well). I would like to thank L. Foerster, who was our Diploma student on this experiment during the development and construction of our atoms-sorting machine. He is now a Ph.D. student on the atoms-interferometer experiment, where he has started a new huge single-atom project together with M. Karski, whom I want to acknowledge as well and whom I want to thank for many interesting discussions, especially about the results of our "number-locked loading" experiment.

Next I would like to thank our post-docs A. Rauschenbeutel and W. Alt for the supervision of our work as well as for being open minded towards fruitful discussions on a multitude of topics ranging from our lab-related physics to the deepest secrets of the Deutsche Bahn while having lunch at the Mensa as well as for supporting our unusual ideas and especially for upholding the creative atmosphere in the lab.

Without our electronic workshop the development of our experimental setup would have been much slower. I would like to thank the staff of our electronic workshop for their collaborative and supporting work, for their understanding of our problems and their help to solve them in the most effective way possible (even when we wanted to build a "Doktorhut" controlled by a microprocessor). I want to thank the staff of our precision-mechanics workshop as well for their fast and high quality work. I would like to thank our caretaker Mr. Ernst for solving all kinds of technical problems in the house.

My thanks also refer to the staff of our secretariat and administration, Annelise, Ilona, Fien and Dietmar, for helping me in administrative matters as well as to all other co-workers in the Institute fuer Angewandte Physik who I did not mention personally for keeping a positive working environment in the house.

And, finally, my huge thanks belong to my parents and to my girlfriend Doerthe for supporting my positive spirit during the whole period of the thesis and especially during the end of it.